Structured Light in Complex Channels

Author:
Asher Klug

Supervisor:
Prof. Andrew Forbes

UNIVERSITY OF THE WITWATERSRAND
JOHANNESBURG

A thesis submitted in fulfillment of the requirements
for the degree of Master of Science

in the

Structured Light Laboratory
School of Physics

April 24, 2022

Declaration

I declare that I am the author of this dissertation which is being submitted for the Degree of Master of Science at the University of the Witwatersrand, Johannesburg. It has not been submitted before for any degree or examination at any other University.

I also declare that this is my own original work, except where due reference is made for work forming part of jointly-authored publications. My contribution and those of the other authors to this work have been explicitly indicated below.

Signed: Asher Klug

Date: April 24, 2022

Abstract

The renewed interest in studying the relationship between the atmosphere and structured light can be, in part, attributed to the promise of free space optical (FSO) communication networks. These channels have been suggested as a mechanism for bringing high speed internet connections to difficult-to-reach areas, overcoming the cost and hassle of traditional fibre optic connections. However, propagating structured light fields through complex media like the Earth's atmosphere introduces a new suite of problems. Understanding the interaction between optical fields and a turbulent atmosphere has therefore become a highly topical research field, and forms the focus of this dissertation.

A cursory introduction to structured light is presented in Chapter 1. The different families of beams studied in this dissertation are obtained from the Helmholtz equation and we describe the propagation of these beams using scalar diffraction theory. Next, the angular spectrum method of propagation is presented as it is used for numerical simulations throughout this dissertation. Finally, we explain how structured light fields can carry orbital angular momentum (OAM). This property of light is studied extensively in Chapter 4.

Chapter 2 discusses the experimental techniques and equipment used to shape light, simulate turbulence and take measurements. We illustrate how light is controlled in the laboratory through the implementation of holograms displayed on liquid crystal spatial light modulators and digital micromirror devices and provide the procedure for generating these holograms. We then show how carefully chosen holograms are used to evaluate an inner product of two optical states to obtain a modal decomposition of a desired field.

Chapter 3 explains characteristics and statistics of atmospheric turbulence. Using these statistics and physical insight, we introduce the thin phase screen approximation to modelling weak turbulence and discuss the different methods used to generate these screens. We then extend this model to strong turbulence using the split-step method and the chapter concludes by discussing how the strength of these phase screens is calibrated in a laboratory setting.

Chapters 4 and 5 present novel research. The atmosphere is famous for causing distortions in the OAM spectrum of structured light beams. Chapter 4 recasts this effect as a transfer of OAM between the beam and the atmosphere by viewing the atmosphere as a store of OAM. Such a perspective allows us to resolve the debate on the effects of turbulence on structured light. We show that the spread in OAM of structured light beams caused by turbulent effects is symmetric about and independent of the beam's initial OAM. Further, the spectrum finds a maximum value at the initial OAM. We show that the beam's size determines a field's behaviour in turbulence and not its OAM by considering Laguerre-Gaussian and perfect vortex modes.

Chapter 5 writes the turbulent channel as a linear operator and finds its corresponding eigenvectors, termed ‘eigenmodes’. These beams are invariant as they propagate through a turbulence atmosphere. The chapter explains important numerical details such as sampling constraints and we verify the robustness of the eigenmodes experimentally. When considering many realisations of turbulence, we show that it is better to use the ‘usual’ vacuum modes in communication studies as turbulence has a zero average effect on structured light fields.

To my loving parents, Barbara and Eric, and wife, Ariella

Acknowledgements

I want to thank my supervisor, Prof. Andrew Forbes, for the invaluable experience he has granted me over the course of this project. I am grateful for all the discussions we have had and the tips (both small and large) on how to perform excellent scientific research. I am also deeply grateful for the bursary provided by Prof. Forbes and the constant attention and care, both for this dissertation and my career.

Thank you to my parents for their love, advice, wisdom and for the wonderful opportunity to study what I enjoy. To my sisters, thank you for your constant encouragement and loving support.

I want to acknowledge my wife who has heard about this dissertation more than anyone else. Thank you for understanding the long hours and for always being a supportive, warm presence, especially during those weeks when ‘nothing seems to be working’.

Lastly, I am grateful to the Almighty, the source of all our knowledge and accomplishments, for the kindness He has always shown me.

Contents

List of Figures

List of Tables

List of Publications

Journal articles

• **Klug, A.**, Nape, I., and Forbes, A., 2021. "The orbital angular momentum of a turbulent atmosphere and its impact on propagating structured light fields", *New Journal of Physics*, **23**(9), p093012.

A.K. was the primary author, developed the theory, built the experiment, performed the measurements and wrote the manuscript.

• Nape, I., Singh, K., **Klug, A.**, Buono, W., Rosales-Guzmán, C., Franke-Arnold, S., Dudley, A. and Forbes, A., 2021. "Revealing the invariance of vectorial structured light in perturbing media." *Nature Photonics*, (**accepted**).

A.K. designed an experiment and performed the measurements for the basis-dependent turbulence data and contributed to the manuscript.

• **Klug, A.**, Forbes, A., 2021. "Eigenmodes of a turbulent atmosphere". (**Manuscript in preparation**.)

A.K. was the primary author, developed the theory, built the experiment, performed the measurements and wrote the manuscript.

• Bachmann, D., **Klug, A.**, Forbes, A., 2021. "The effects of strong Kolmogorov turbulence on Laguerre-Gaussian beams." (**Manuscript in preparation**.)

A.K. built the experiment, performed the measurements and contributed to the manuscript.

Conference proceedings

Klug, A., Pinnell, J., and Forbes, A., "Spatial filtering of Structured Light," in Education and Training in Optics & Photonics Conference 2021, A. Danner, A. Poulin-Girard, and N. Wong, eds., OSA Technical Digest (Optical Society of America, 2021), paper Th3A.3.

List of Symbols

- $\mathbf{R} = (x, y, z),\ (R, \phi, \theta)$ – three dimensional spatial coordinate
- $\mathbf{r} = (x, y),\ (r, \phi)$ – two dimensional transverse spatial coordinate
- $\boldsymbol{\rho} = (\rho, \phi)$ – unit transverse spatial coordinate
- $\mathbf{k} = (k_x, k_y, k_z),\ (k, \varphi, \vartheta)$ – three dimensional angular frequency coordinate
- $\boldsymbol{\nu} = (\nu_x, \nu_y),\ (\nu, \varphi)$ – two dimensional angular frequency coordinate
- ∇^2 – three dimensional Laplacian
- $\nabla_t^2 = \partial_x^2 + \partial_y^2$ – tranverse Laplacian
- λ – wavelength
- ω – temporal angular frequency
- $k = 2\pi/\lambda$ – wavenumber
- $\mathcal{D}$ – structure function
- Φ – power spectral density
- $\mathcal{P}$ – one dimensional power spectral density
- B – covariance function
- n – refractive index
- δn – fluctuation in refractive index
- C_A^2 – structure constant of A
- r_0 – Fried parameter
- σ_R^2 – Rytov variance
- $D = 2\mathcal{R}$ – aperture diameter
- P – radius of curvature
- z_R – Rayleigh length

Introduction

Space division multiplexing (SDM) and its subsidiary mode division multiplexing (MDM) are mooted as solutions to the impending data crunch, and seek to exploit the spatial degrees of freedom of light for additional information capacity.[1–4] This includes using light's spatial modes, tailored in amplitude, phase and polarisation for what is now commonly referred to as structured light.[5] One popular example is light tailored to have an azimuthally varying phase of the form $\exp(i\ell\phi)$ with integer topological charge (TC) ℓ for $\ell\hbar$ of orbital angular momentum (OAM) per photon.[6–8] This property of light and its interaction with a turbulent atmosphere is studied extensively in this dissertation. Although it is understood that other orthogonal mode sets are equally valid, including using the full radial and azimuthal indices of the Laguerre-Gaussian (LG) modes[9–11] as well as Bessel,[12–21] Hermite-Gaussian[22–24] and vectorial modes,[25–28] OAM has become the mode of choice in the majority of communication studies.[29,30] These OAM modes (theoretically) provide an unlimited alphabet which can be used to transmit information to a receiver situated many kilometers away.

Unfortunately, structured light becomes distorted in the presence of atmospheric turbulence in free-space atmospheric links.[31–34] The orthogonality of the modes is impaired which leads to the deleterious effects of decay in entanglement in quantum states,[35–42] and modal crosstalk for classical communication channels.[43–50] For this reason, a crucial step towards deploying free space classical[51,52] and quantum communication channels[53] is the exact characterisation of the turbulence induced perturbations on structured light.

However, characterising this interaction has produced conflicting claims as to the role that a beam's OAM plays in determining its behaviour in turbulence. In attempting to investigate the degradation of OAM modes in turbulence, Paterson[35] famously derived a theoretical expression for the likelihood of scattering between OAM states, showing that the probabilities were independent of the initial OAM that a beam carried. This analysis assumed that the amplitude profile was independent of the topological charge. Further theoretical investigations[54] using optical vortex beams supported these findings with sufficient numerical and experimental confirmation.[55,56] In contrast, numerical studies of entangled OAM states in turbulence found that higher order single photon LG states were less robust than lower order ones.[57] These results seemed to indicate that a beam's behaviour is strongly governed by its OAM. Other studies have shown that there is also a basis dependence: for example, different results are obtained when using vortex Gaussian beams in comparison to LG, optical vortex[58,59] and Ince-Gaussian beams.[33] Indeed, while these advancements have elucidated the detrimental effects of turbulence on OAM-carrying light fields, the nuances involved in the modal dependence argument are not settled since there is disagreement with early findings. The uncertainty can in part be attributed to the fact that the focus is on the beam itself, and thus its construction plays a large role in the outcome.

Being able to eliminate or at least mitigate the effects of turbulence is highly desirable in any free space channel. Several methods have been investigated. The polarization structure of vector modes could provide a robust degree of freedom for optically encoding information.[46,60] These states of light differ from scalar beams in that their polarization is spatially dependent and is thus inhomogeneous across the transverse plane.[5] In the world of scalar beams, some mode sets are more robust than others: HG beams could prove to be more resilient than LG beams due to the Cartesian symmetry of their phase profiles.[61]

Modal diversity has been proposed as an effective error-reduction scheme in communication channels.[62] There is, however, a reduction in the multiplexing gain.[63] Adaptive optics for pre- and post-correction,[64–66] iterative routines[67] and deep learning models[68] have also found success in removing these unwanted distortions that arise from atmospheric turbulence.

Here, we present a comprehensive treatment of the interaction between turbulence and optical fields. This is achieved by reviewing concepts in structured light, presenting a detailed discussion on the Earth's atmosphere and techniques to model turbulent effects, providing novel results on the effects of OAM on a beam's behaviour in turbulence and obtaining sets of modes which are invariant under the action of turbulence, without the need for adaptive optics or machine learning routines.

Chapter 1

Structured light

In this chapter we provide the theoretical tools needed to understand orbital angular momentum and the propagation of optical fields through space. We start from Maxwell's equations which govern the spatial evolution of electromagnetic waves in any medium. We show how to solve the inhomogeneous form of the Helmholtz equation which is used extensively in Chapter 5. The derivation of the Laguerre-Gaussian family of beams is then presented along with perfect vortex beams since these mode sets are beams studied in this dissertation. The principles of scalar diffraction theory are explained by introducing the Huygens-Fresnel diffraction integral which plays a central role in Chapter 5, and the angular spectrum method of propagation, which was used for numerical simulations. We conclude by showing how coherent fields can carry orbital angular momentum. This property of light is studied extensively in Chapter 4.

1.1 Paraxial Helmholtz equation

Maxwell's equations completely describe the behaviour of the electromagnetic field, whose electric and magnetic components are, respectively, denoted as **E** and **B**. These equations (not only) permit solutions for **E** and **B** which correspond (physically) to travelling waves. We will present an abridged discussion on obtaining these solutions since the procedure is well-known.[69]

In the absence of any charges and currents, Maxwell's equations are given by

$$\epsilon\nabla\cdot\mathbf{E}=0, \tag{1.1}$$

$$\nabla\cdot\mathbf{B}=0, \tag{1.2}$$

$$\nabla\times\mathbf{E}=-\frac{\partial}{\partial t}\mathbf{B}, \tag{1.3}$$

$$\nabla\times\mathbf{B}=\epsilon\mu_0\frac{\partial}{\partial t}\mathbf{E}, \tag{1.4}$$

where ϵ and μ_0 are the dielectric permittivity and magnetic permeability of the medium, respectively.[69] This derivation assumes that the medium has the same magnetic permeability as the vacuum. To eliminate **B** in Eq. 1.3, we apply the curl operator ($\nabla\times$) to both sides of Eq. 1.3 and use Eq. 1.4 to obtain

$$\nabla\times\nabla\times\mathbf{E}=-\epsilon\mu_0\frac{\partial^2}{\partial t^2}\mathbf{E}. \tag{1.5}$$

The vector identity $\nabla \times \nabla \times \mathbf{A} = \nabla(\nabla \cdot \mathbf{A}) - \nabla^2 \mathbf{A}$ for a vector $\mathbf{A}$ simplifies Eq. 1.5 to

$$\nabla(\nabla \cdot \mathbf{E}) - \nabla^2 \mathbf{E} = -\epsilon \mu_0 \frac{\partial^2}{\partial t^2} \mathbf{E}. \tag{1.6}$$

In the absence of any sources, $\nabla \cdot \mathbf{E} = 0$ (see Eq. 1.1) and so

$$\nabla^2 \mathbf{E} = \frac{n^2}{c^2} \frac{\partial^2}{\partial t^2} \mathbf{E}, \tag{1.7}$$

where $n = \sqrt{\epsilon/\epsilon_0}$ is the refractive index of the medium and ϵ_0 the permittivity of the vacuum. The quantity $c = 1/\sqrt{\epsilon_0 \mu_0}$ is the speed of light in a vacuum.[69] A similar derivation can be performed for the magnetic field $\mathbf{B}$. Eq. 1.7 presents a scalar wave equation for each spatial component of $\mathbf{E}$, thus yielding three equations which must be solved to describe the travelling wave $\mathbf{E}$. We will solve Eq. 1.7 for a single scalar component. We assume that the (scalar) waves can be written as the product $\mathrm{U}(\mathbf{R}) \exp(-i\omega t)$, where ω is the angular frequency of the wave and $\mathrm{U}(\mathbf{R})$ describes its spatially dependent behaviour with $\mathbf{R} = (x, y, z)$. Using this ansatz and the method of separation of variables, we can isolate the temporal and spatial components of Maxwell's equations to obtain the Helmholtz equation

$$\left(\nabla^2 + k^2 n^2\right) \mathrm{U}(\mathbf{R}) = 0, \tag{1.8}$$

where $k = 2\pi/\lambda$ is the wavenumber for wavelength λ and n is the refractive index of the medium. For simplicity, consider the case $n = 1$. A plane wave $\mathrm{U}(\mathbf{R}) = \mathcal{A} \exp(i\mathbf{k} \cdot \mathbf{R})$ is a trivial solution to Eq. 1.8 for a constant $\mathcal{A}$ and $\mathbf{k} = (k_x, k_y, k_z)$, obtained by performing a separation of variables in Cartesian coordinates. A more interesting solution is the spherical wave

$$\mathrm{U}(\mathbf{R}) = \mathcal{A} \frac{\exp(ikR)}{4\pi R}, \tag{1.9}$$

whose wavefronts (surfaces of constant phase) form concentric spheres, centered at $\mathbf{R} = \mathbf{0}$, and $R = \|\mathbf{R}\|$. We note that

$$\lim_{R \to 0} \frac{\exp(ikR)}{4\pi R} = \delta^{(3)}(R) = \delta(x)\delta(y)\delta(z), \tag{1.10}$$

which corresponds to a point source located at $R = 0$. That is, a spherical wave corresponds to solving the Helmholtz equation for a point source and is thus the Green's function for Eq. 1.8. This is used to solve Eq. 1.8 with a driving term $\mathcal{Q}$

$$\left(\nabla^2 + k^2 n^2\right) \mathrm{U}(\mathbf{R}) = \mathcal{Q}(\mathbf{R}) \tag{1.11}$$

where

$$\mathrm{U}(\mathbf{R}) = \int \mathrm{d}^3 \mathbf{R}' \, \frac{\exp(ik\|\mathbf{R}' - \mathbf{R}\|)}{4\pi\|\mathbf{R}' - \mathbf{R}\|} \mathcal{Q}(\mathbf{R}'). \tag{1.12}$$

Plane waves, however, do not represent physical solutions since they have infinite energy. Physically realisable solutions are obtained if we assume that the waves are propagating in the z-direction and that their transverse (x-y plane) spatial extent is much smaller than the propagation distance. This assumption is called the paraxial approximation and results in the paraxial Helmholtz equation

$$\left(\nabla_t^2 + 2ik\partial_z\right) \mathrm{V}(\mathbf{R}) = 0 \tag{1.13}$$

for a vacuum refractive index of $n = 1$ and $\mathrm{V}(\mathbf{R}) = \mathrm{U}(\mathbf{R}) \exp(-ikz)$. The operator $\nabla_t^2 = \partial_x^2 + \partial_y^2$ is the transverse Laplacian. Solving this paraxial equation with the ansatz of a Gaussian envelope returns the famous Gaussian beam, with functional form[70]

$$\mathrm{V}(\mathbf{R}) = \mathcal{A}\frac{w_0}{w(z)} \exp\left(-\frac{r^2}{w^2(z)}\right) \exp\left(\frac{-ikr^2}{2P(z)} + i\psi(z)\right). \tag{1.14}$$

The Gaussian beam is an important physical solution to the paraxial wave equation and $\mathbf{R} = (\mathbf{r}, z)$. The parameter $w(z) = w_0\sqrt{1 + (z/z_R)^2}$ defines the beam's width with $w(0) = w_0$, known as the beam's waist radius. $z_R = \pi w_0^2/\lambda$ is the beam's Rayleigh range and is the distance over which the beam's area doubles. $P(z) = z\left(1 + (z_R/z)^2\right)$ is the radius of curvature of the wavefront and $\psi(z) = \arctan(z/z_R)$ is the Gouy phase.

1.1.1 Laguerre-Gaussian modes

Solving Eq. 1.13 directly using the method of separation of variables introduces inherent symmetry into the solutions. In a cylindrical coordinate system ($\mathbf{R} = (r, \phi, z)$) we suppose that $\mathrm{V}(\mathbf{R})$ can be written as the product $\mathrm{X}(r, z)\Psi(\phi)$. Such solutions have the functional form[70]

$$\begin{aligned} \mathrm{LG}_p^\ell(r,\phi,z) = C_p^\ell \frac{w_0}{w(z)} \left(\frac{\sqrt{2}r}{w(z)}\right)^{|\ell|} L_p^{|\ell|}\left(\frac{2r^2}{w^2(z)}\right) \exp\left(-\frac{r^2}{w^2(z)}\right) \times \\ \times \exp\left(i\ell\phi\right) \exp\left(\frac{-ikr^2}{2P(z)} + iN\psi(z)\right), \end{aligned} \tag{1.15}$$

and are known as the Laguerre-Gaussian modes. $L_p^{|\ell|}(\cdot)$ is the associated Laguerre polynomial (hence the name of the modes), $N^2 = 1 + 2p + |\ell|$ is the mode number and C_p^ℓ is a normalisation constant. Eq 1.15 reduces to Eq. 1.14 for $p = \ell = 0$. The second moment radius, defined as

$$\overline{r^2} = \sqrt{2\frac{\int \mathrm{d}^2\mathbf{r}\ r^2\,\mathrm{LG}_p^\ell(r,\phi,z=0)}{\int \mathrm{d}^2\mathbf{r}\ \mathrm{LG}_p^\ell(r,\phi,z=0)}} = w_0\sqrt{1 + 2p + |\ell|}, \tag{1.16}$$

grows with mode number and so higher order modes are also larger. These modes form a complete and orthonormal set with

$$\langle p', \ell' | p, \ell \rangle = \int \mathrm{d}^2\mathbf{r}\ \left(\mathrm{LG}_{p'}^{\ell'}(\mathbf{r}, z)\right)^* \mathrm{LG}_p^\ell(\mathbf{r}, z) = \delta_{p',p}\delta_{\ell',\ell}. \tag{1.17}$$

Intensity and phase (as insets) plots for LG beams are shown in Fig. 1.1 for $p \in [0, 2]$ and $\ell \in [0, 3]$. The fundamental Gaussian mode is shown in the top left corner.

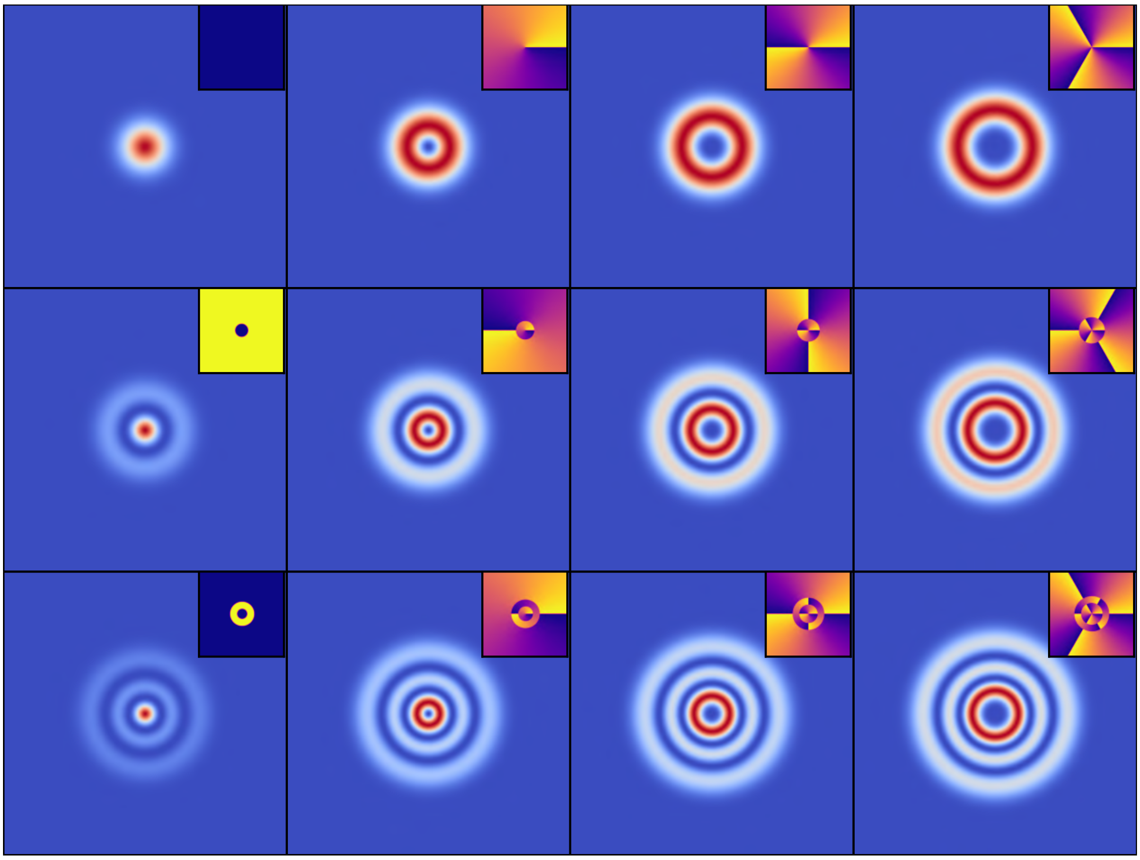

Figure 1.1: Laguerre-Gaussian intensity plots with the phase displayed as an inset for $p \in [0, 2]$, $\ell \in [0, 3]$ and $z = 0$. The fundamental Gaussian mode occupies the top left corner with the p index incrementing downwards and the ℓ index to the right.

1.1.2 Perfect vortex modes

The 'perfect vortex' (PV) modes form another family of beams which are used in this dissertation. These modes have intensity patterns which resemble rings and have the following functional form in the waist plane:[71]

$$\mathrm{PV}_\ell^{\mathrm{ideal}}(r, \phi) = \delta(r - r_v)\exp\left(i\ell\phi\right), \tag{1.18}$$

where r_v is the radial position of the ring. It is physically impossible to realise such a mode since the delta-function demands an infinitely thin ring. However, nature is very forgiving and one can approximate these pure vortex modes with[71]

$$\mathrm{PV}_\ell(r, \phi) = \exp\left(-\frac{(r - r_v)^2}{w_0^2}\right)\exp\left(i\ell\phi\right), \tag{1.19}$$

provided that the beam waist w_0 is much smaller than the radius r_v. Unlike the LG modes, these modes do not retain their shape as they propagate. In fact, their far field patterns approximate the Bessel-Gaussian mode family in the near field, which have the functional form[72]

$$\mathrm{BG}_{kr}^{\ell}(r, \phi, 0) = J_\ell(k_r r)\exp\left(-\frac{r^2}{w_0^2}\right)\exp\left(i\ell\phi\right), \tag{1.20}$$

where $J_\ell(\cdot)$ is the ℓth order Bessel function of the first kind and k_r is the radial wavevector such that $k^2 = k_r^2 + k_z^2$. Bessel-Gaussian beams are shown in Fig. 1.2 for $\ell = 5$ at three different planes: at $z = 0$, $z = 2.5$ m and $z \to \infty$ (far field). The upper and lower rows correspond to $k_r = 5 \times 10^3\ \mathrm{m}^{-1}$ and $k_r = 10^4\ \mathrm{m}^{-1}$, respectively. The far field intensity pattern is a thin ring whose radius is controlled by k_r. These rings are the perfect vortex beams presented in Eq. 1.19.

This perfect vortex – Bessel-Gaussian duality is shown in Fig. 1.3 for azimuthal indices $\ell = 0, 5, 15$ at three planes: the waist plane $z = 0$, $z = 5z_R$ and $z \to \infty$. The distance z_R is the Rayleigh length for a Gaussian beam with the same waist parameter w_0. We see that after propagating to the far field, the intensity pattern resembles a Bessel-Gaussian beam. The perfect vortex beams were generated according to Eq. 1.19 with $r_v \approx 16w_0$. We also note that the near field intensity pattern is independent of the initial charge ℓ.

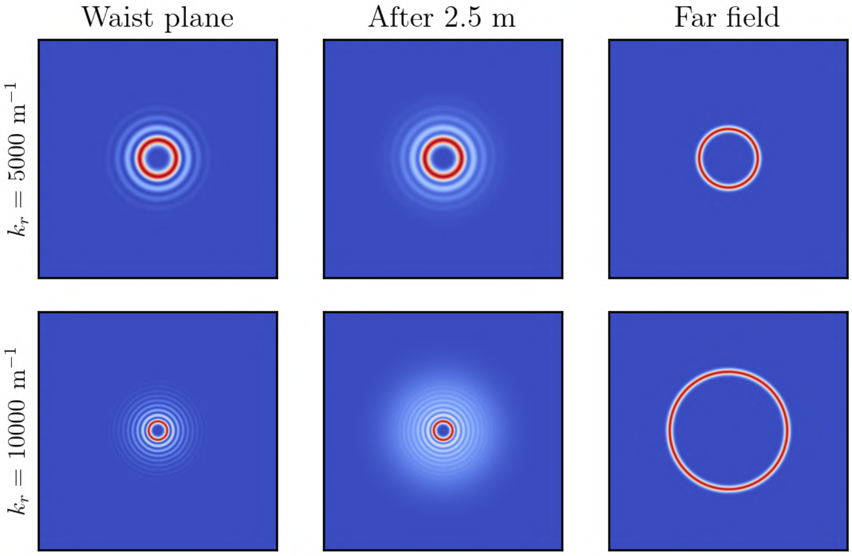

Figure 1.2: Bessel-Gaussian beams with $k_r = 5 \times 10^3\ \mathrm{m}^{-1}$ and $k_r = 10^4\ \mathrm{m}^{-1}$ are shown: at the waist plane ($z = 0$), after propagating for 2.5 metres and in the far field. The far field pattern is a ring whose radius is controlled by k_r.

1.2 Huygens-Fresnel diffraction

Eq. 1.8 describes the spatial evolution of a wave in the form of a differential equation. Solving Eq. 1.8 results in an integral equation which determines the propagation of an optical field and forms the topic of this subsection. The field at a plane z, given that it was described by $\mathrm{V}(\mathbf{r}', z')$ at the z' plane is

$$\mathrm{V}(\mathbf{R}) = \frac{1}{i\lambda} \int \mathrm{d}^2\mathbf{r}'\ \mathrm{V}(\mathbf{R}') \frac{\exp\left(ik\|\mathbf{R} - \mathbf{R}'\|\right)}{\|\mathbf{R} - \mathbf{R}'\|} \cos\left(\varrho\right), \tag{1.21}$$

where $\cos(\varrho) = z / \|\mathbf{R} - \mathbf{R}'\|$ is cosine of the angle between the vector connecting the points $\mathbf{R}$ and $\mathbf{R}'$ and the z axis. Eq. 1.21 is known as the Huygens-Fresnel integral.[73] We now make a series of approximations to make Eq. 1.21 easier to

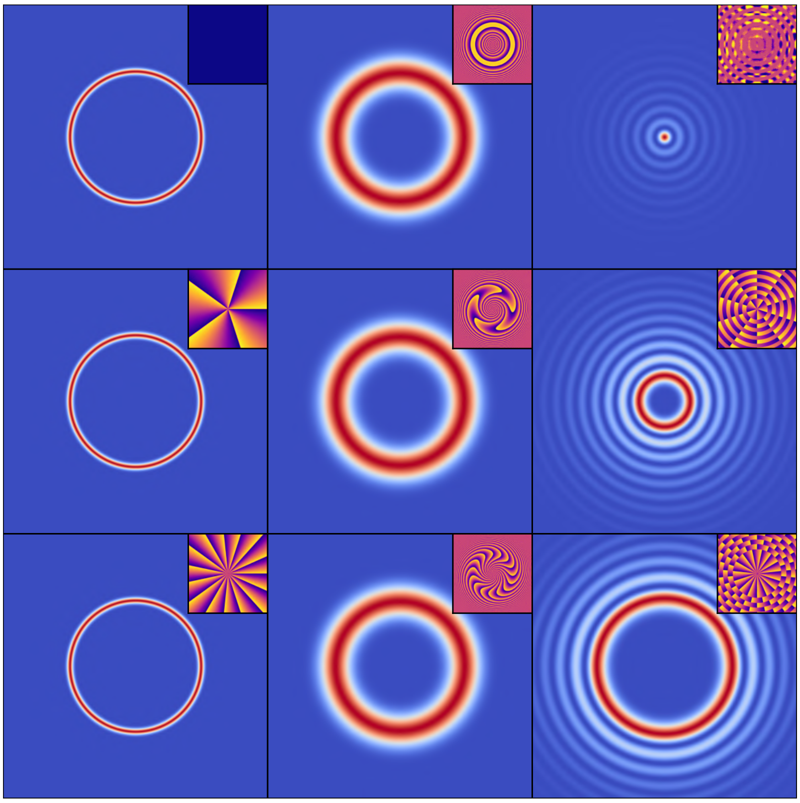

Figure 1.3: Intensity patterns of perfect vortex modes are shown for (from top to bottom) $\ell = 0, 5, 15$ and (from left to right) at $z = 0$, $z = 5z_R$ and $z \to \infty$. Insets show the phase of the beam. Here, z_R is the Rayleigh length of a Gaussian beam with the same waist parameter w_0. The far field is a Bessel-Gaussian beam. In this case, $r_v \approx 16w_0$.

solve. First we set the initial plane to be at $z' = 0$. In the paraxial limit, $z \approx \|\mathbf{R} - \mathbf{R}'\|$ ($\cos(\varrho) \approx 1$) and

$$\mathrm{V}(\mathbf{R}) = \frac{1}{i\lambda z} \int \mathrm{d}^2\mathbf{r}' \;\; \mathrm{V}(\mathbf{R}') \exp\left(ik\|\mathbf{R} - \mathbf{R}'\|\right). \tag{1.22}$$

We cannot approximate $z \approx \|\mathbf{R} - \mathbf{R}'\|$ in the phase factor in Eq. 1.22 since k is very large for optical fields. However, we employ the Fresnel approximation

$$\|\mathbf{R} - \mathbf{R}'\| = \sqrt{\|\mathbf{r} - \mathbf{r}'\|^2 + z^2} \approx z + \frac{\|\mathbf{r} - \mathbf{r}'\|^2}{2z}, \tag{1.23}$$

which treats the curvature in the wavefronts as parabolic rather than spherical. Thus

$$\mathrm{V}(\mathbf{R}) = \frac{\exp(ikz)}{i\lambda z} \int \mathrm{d}^2\mathbf{r}' \;\; \mathrm{V}(\mathbf{R}') \exp\left(\frac{ik\|\mathbf{r} - \mathbf{r}'\|^2}{2z}\right). \tag{1.24}$$

In the limit that $\mathbf{r}' \ll z$ (i.e. the field has propagated a comparatively "large" distance), we can neglect the term $\|\mathbf{r}'\|^2$ in $\|\mathbf{r} - \mathbf{r}'\|^2 = \|\mathbf{r}'\|^2 + \|\mathbf{r}\|^2 - 2\mathbf{r} \cdot \mathbf{r}'$ (dubbed the "Fraunhofer approximation") to obtain the far field expression

$$\mathrm{V}(\mathbf{R}) = \frac{\exp(ikz)}{i\lambda z} \exp\left(\frac{ikr^2}{2z}\right) \int \mathrm{d}^2\mathbf{r}' \;\; \mathrm{V}(\mathbf{R}') \exp\left(\frac{-ik\mathbf{r} \cdot \mathbf{r}'}{z}\right). \tag{1.25}$$

Eq. 1.25 can be rewritten as the Fourier transform equation

$$\mathrm{V}(\mathbf{R}) = \frac{\exp\left(ikz\right)}{i\lambda z} \exp\left(\frac{ikr^2}{2z}\right) \mathcal{F}\left\{\mathrm{V}(\mathbf{R}')\right\}, \tag{1.26}$$

where the spatial frequency coordinate $\boldsymbol{\nu}$ is related to the actual spatial coordinates according to

$$\boldsymbol{\nu} = \frac{k\mathbf{r}}{z}. \tag{1.27}$$

That is, the far field is equivalent to the Fourier transform of the initial (near) field, ignoring phase factors.

1.3 Angular spectrum method of propagation

The propagation of a plane wave

$$|\boldsymbol{\nu}\rangle = \frac{1}{2\pi} \exp\left(i\boldsymbol{\nu}\cdot\mathbf{r}\right) \tag{1.28}$$

along the z direction does not require solving the Huygen's-Fresnel integral (Eq. 1.24). Consider a plane wave $\mathrm{U}(\mathbf{r},0) = \exp\left(ik_x x + ik_y y\right)/2\pi$ at $z = 0$. The same wave a distance z later is just

$$\mathrm{U}(\mathbf{r},z) = \mathrm{U}(\mathbf{r},0)\exp(ik_z z), \tag{1.29}$$

where the propagation is accomplished by multiplying the initial field by the phase factor $\exp(ik_z z)$ and $k_z = \sqrt{k^2 - k_x^2 - k_y^2}$.

Waves with different $\boldsymbol{\nu}$ vectors are Dirac-delta orthogonal as

$$\langle\boldsymbol{\nu}'|\boldsymbol{\nu}\rangle = \frac{1}{(2\pi)^2}\int \mathrm{d}^2\boldsymbol{\nu}'\ \exp\left(-i\boldsymbol{\nu}'\cdot\mathbf{r}\right)\exp(i\boldsymbol{\nu}\cdot\mathbf{r}) = \delta^{(2)}(\boldsymbol{\nu}'-\boldsymbol{\nu}), \tag{1.30}$$

and can be used to perform a modal decomposition of a given function V in the transverse plane. However, unlike discrete sets of basis functions, the plane waves are described by a continuous parameter $\boldsymbol{\nu}$ and are not labelled discretely. As such, V is written in terms of an integral

$$\mathrm{V}(\mathbf{r},z) = \frac{1}{2\pi}\int \mathrm{d}^2\boldsymbol{\nu}\ \mathcal{V}(\boldsymbol{\nu},z)\exp(i\boldsymbol{\nu}\cdot\mathbf{r}) \tag{1.31}$$

rather than a discrete sum. The function $\mathcal{V}$ is retrieved according to

$$\mathcal{V}(\boldsymbol{\nu},z) = \frac{1}{2\pi}\int \mathrm{d}^2\mathbf{r}\ \mathrm{V}(\mathbf{r},z)\exp(-i\boldsymbol{\nu}\cdot\mathbf{r}). \tag{1.32}$$

These integrals are, of course, the Fourier transform operators. Performing the Fourier transform on a field V is equivalent to finding its expansion in the plane wave basis. $\mathcal{V}$ is referred to as the angular spectrum of V as $\boldsymbol{\nu}$ is a spatial angular frequency coordinate. We use this to propagate V a distance z. First, Fourier transform V to obtain its angular (plane wave) spectrum $\mathcal{V}$. Multiplying $\mathcal{V}$ by $\exp(ik_z z)$ will propagate the plane waves, after which we apply the inverse

Fourier transform to return to the spatial domain. This is procedure is captured in the equation

$$\mathrm{V}(\mathbf{r},z) = \mathcal{F}^{-1}\left\{\mathcal{F}\left\{\mathrm{V}(\mathbf{r},0)\right\}\exp(ik_z z)\right\}. \tag{1.33}$$

This algorithm is computationally easier to implement than solving the Huygens-Fresnel integral and therefore used for numeric simulations.

1.4 Orbital angular momentum

An electromagnetic field carries a linear momentum density **L** and linear momentum **P**

$$\mathbf{L} = \epsilon_0\,\mathbf{E}\times\mathbf{B}, \quad \mathbf{P} = \int \mathrm{d}^3\mathbf{R}\ \mathbf{L}, \tag{1.34}$$

and an angular momentum density **M** and angular momentum **J**

$$\mathbf{M} = \epsilon_0\,\mathbf{R}\times(\mathbf{E}\times\mathbf{B}), \quad \mathbf{J} = \int \mathrm{d}^3\mathbf{R}\ \mathbf{M}. \tag{1.35}$$

In a seminal paper,[6] Allen et al. showed that an azimuthal phase factor $\exp(i\ell\phi)$ (like that in Eq. 1.15) corresponds to a beam carrying $\ell\hbar$ of orbital angular momentum (OAM) per photon. The ensuing discussion follows their paper closely.

Spin angular momentum is associated with the state of polarisation of an electromagnetic field. Beth[74] measured the spin angular momentum of light by observing the torque exerted on birefringent plates by circularly polarised light. It was found that the ratio of the angular to linear momenta was $\lambda/2\pi$, and that each photon carried $\hbar$ of angular momentum. Consider a field whose complex amplitude is described by $\mathrm{V}(\mathbf{R})\exp(ikz)$. In the Lorenz gauge, this field has a vector potential

$$\mathbf{A} = \hat{x}\,\mathrm{V}(\mathbf{R})\exp(ikz), \tag{1.36}$$

where $\hat{x}$ is the unit vector in the x-direction. The electric **E** and magnetic **B** fields are related according to the equations

$$\mathbf{B} = \nabla\times\mathbf{A}, \tag{1.37}$$

$$\mathbf{E} = \frac{ic^2}{\omega}\nabla\times\mathbf{B}. \tag{1.38}$$

The time-averaged, real-valued linear momentum density is

$$\mathbf{L} = \frac{\epsilon_0}{2}\left(\mathbf{E}^*\times\mathbf{B} + \mathbf{E}\times\mathbf{B}^*\right). \tag{1.39}$$

In this gauge **L** is then given by

$$\frac{i\omega\epsilon_0}{2}\left(\mathrm{V}\nabla\mathrm{V}^* - \mathrm{V}^*\nabla\mathrm{V}\right) + \omega\epsilon_0 k|\mathrm{V}|^2\hat{z} \tag{1.40}$$

for a field V that satisfies the paraxial approximation. We will consider the case $\mathrm{V}(\mathbf{R}) = \mathrm{LG}_0^\ell(\mathbf{R})$ which has a "donut" intensity profile (see the first row in Fig. 1.1) and complex field amplitude

$$\mathrm{V}(\mathbf{r},z) = C_0^\ell\frac{w_0}{w(z)}\left(\frac{\sqrt{2}r}{w(z)}\right)^{|\ell|}\exp\left(-\frac{r^2}{w^2(z)}\right)\exp\left(i\ell\phi - \frac{ikr^2}{2P(z)} + iN\psi(z)\right). \tag{1.41}$$

Substituting Eq. 1.41 into Eq. 1.40 gives (per unit power)

$$\mathbf{L} = \frac{|\mathrm{V}|^2}{c}\left(\frac{rz}{z^2+z_R^2}\hat{r} + \frac{\ell}{kr}\hat{\phi} + \hat{z}\right), \tag{1.42}$$

and an angular momentum density per unit power

$$\mathbf{M} = |\mathrm{V}|^2\left(-\frac{\ell z}{\omega r}\hat{r} + \frac{r}{c}\left[\frac{z^2}{z^2+z_R^2} - 1\right]\hat{\phi} + \frac{\ell}{\omega}\hat{z}\right). \tag{1.43}$$

Finding the total angular momentum requires integrating Eq. 1.43 over all space. Performing the integration leaves only the z term due to the symmetry of the radial and azimuthal components. Comparing the linear and angular momentum densities in the z direction gives

$$\frac{M_z}{L_z} = \ell\frac{c}{\omega} = \frac{\ell}{k} = \frac{\ell\lambda}{2\pi}. \tag{1.44}$$

Unlike spin angular momentum, orbital angular momentum is instead related to the helicity of the wavefront and ℓ is referred to as the topological charge. As the beam advances one wavelength its phase undergoes ℓ rotations. The null intensity at the centre of the beam (see Fig. 1.1) is characteristic of light carrying OAM. We see that a larger topological charge corresponds to a greater optical vortex (region of no intensity) as the phase is spiraling 'quicker' and is undefined at the centre.

Chapter 2

Experimental methods

The effects and characteristics of turbulence were experimentally verified in a laboratory setting during the course of this dissertation. Liquid crystal spatial light modulators and digital micromirror devices were used to both simulate turbulence and perform the necessary measurements. These devices are used to display greyscale images, termed "holograms", which implement the desired modulation of a laser beam. Here, we outline the operation of these devices, their calibration procedures and how their respective holograms are generated to achieve arbitrary modulations. Many of the measurements taken for this dissertation took the form of expanding a given field into an orthogonal basis. This procedure is known as a modal decomposition. We show how this decomposition can be implemented optically using a correctly chosen hologram, lens and camera.

2.1 Spatial light modulators

2.1.1 Principles of operation

The dynamic phase of an electromagnetic field advances according to the elementary relationship

$$\mathrm{d}\phi = \frac{2\pi}{\lambda} n(z)\,\mathrm{d}z \tag{2.1}$$

for some refractive index n. There are thus two ways to directly modulate the phase: either change the refractive index n while keeping the propagation distance $\mathrm{d}z$ fixed, or keep n fixed and vary $\mathrm{d}z$. Spatial light modulators are a tool which allow us to precisely control n to modulate a field's phase to produce some desired effect.

In this research, liquid crystal on silicon displays were used to tailor light using the principle of birefringence. The refractive index inside birefringent materials changes depending on the polarisation and the direction of propagation of the light passing through it. Two axes are present inside birefringent materials – the so-called 'ordinary' (with refractive index n_0) and 'extraordinary' (with refractive index n_e) axes. The birefringence is quantified by the difference

$$\Delta n \equiv n_e - n_0. \tag{2.2}$$

These liquid crystal displays contain many (hundreds of thousands) birefringent crystals whose orientations can be independently controlled by changing the voltages supplied to the electrodes on which the crystals sit. The applied voltage results in rotating a crystal through an angle θ which in turn affects the refractive index of the extraordinary axis according to[72]

$$\frac{1}{n_e^2(\theta)} = \left(\frac{\cos\theta}{n_e(\theta=0)}\right)^2 + \left(\frac{\sin\theta}{n_0}\right)^2. \tag{2.3}$$

By varying the voltages, the phase of a field can be modulated according to Eq. 2.1 with $n = \Delta n = n_e(\theta) - n_0$. These voltages are controlled by digital holograms which are greyscale images whose pixel values are related to some applied voltage, which is in turn realised as a rotation of the liquid crystals.

2.1.2 Calibration

The voltages of the SLM must be calibrated so that the desired phase change is indeed implemented. Each pixel value in the greyscale holograms can range between 0 and 1 with 256 possible linear increments in-between. A value of 0 corresponds to a greyscale colour of black and a phase modulation of 0, whereas a value of 1 corresponds to 'white' and a phase modulation of 2π. Calibrating the SLM involves finding the correct mapping between the voltages and these pixel values.

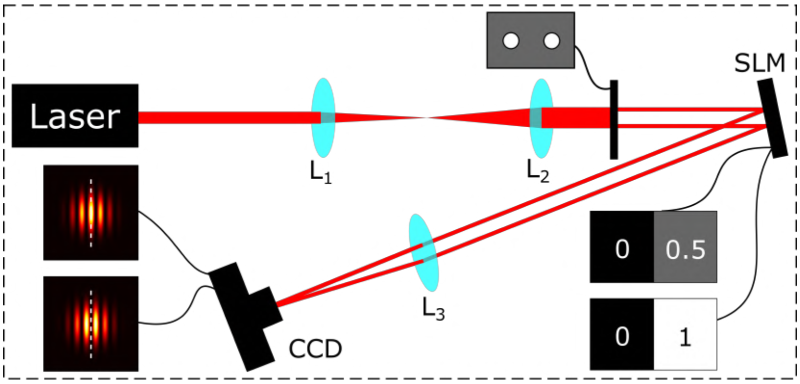

Figure 2.1: A Gaussian beam is expanded and collimated by lenses L$_1$ and L$_2$ onto a double pinhole to produce two circular beams. These beams are then incident on an SLM on which greyscale holograms are displayed, corresponding to a 0, π or 2π phase shift between the two beams. Lens L$_3$ focuses the two beams such that they interfere in the Fourier plane, producing intensity fringes. These fringes are recorded by a CCD.

The calibration procedure is captured in Fig. 2.1. A Gaussian beam is expanded and collimated by lenses L$_1$ and L$_2$ onto the SLM display. A double pinhole aperture then "cuts" out two circles of light which land on separate halves of the screen. A lens L$_3$ focuses these two circles onto the same point in the Fourier plane where they interfere and produces intensity fringes due to the difference in path length they have travelled. These fringes are then recorded on a charge-coupled device (CCD). First, a "black" (all pixel values are 0) hologram is displayed on each half of the SLM screen. Changing the hologram on one half of the screen to “white” (all pixel values are 1) should result in no discernable change in the intensity fringes if the device is calibrated correctly. Further, displaying a “grey” hologram (pixel values are equal to 0.5) should shift the fringes according to a π phase shift. The potentiometer (voltage) values are adjusted until this behaviour is achieved. The voltages are mapped to pixel values through “gamma”-files which are provided by the manufacturer.

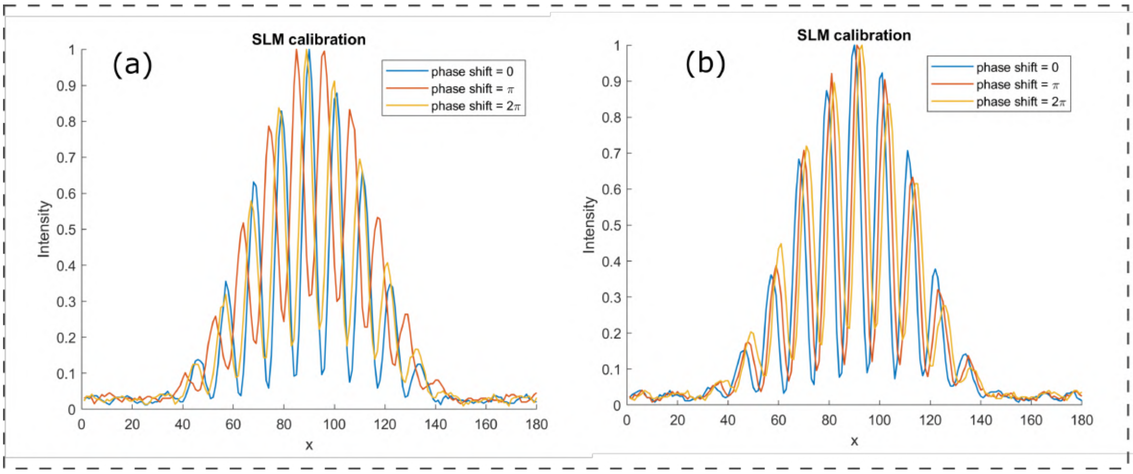

Figure 2.2: Intensity cross-sections for interference fringes during the calibration procedure. (a) corresponds to a correctly calibrated SLM, whereas (b) illustrates an incorrect phase modulation for the encoded π and 2π phase shifts.

Fig. 2.2 shows cross-sections laterally through the intensity fringes obtained during a calibration procedure. Both Fig. 2.2(a) and Fig. 2.2(b) show lines for phase modulations of 0, π and 2π. However, Fig. 2.2(a) corresponds to the correct voltages and one can see that the 0 and 2π lines are superimposed, whereas the π line is out of phase. Fig. 2.2(b) shows the effects of the incorrect voltages. There is little variation between the different encoded phase shifts.

There is another, sometimes easier, method that can be used to calibrate an SLM. This method uses the very high efficiency of a blazed grating

$$g_{\text{blazed}}(x, y) = 2\pi\left(G_x x + G_y y\right) \mod 2\pi \tag{2.4}$$

with respect to the first diffraction order. Specifically, a pure vortex beam $\exp(i\ell\phi)$ is created on the SLM with a blazed grating and the far field intensity pattern is observed on a CCD such that both the zero and first diffraction orders can be seen simultaneously. The potentiometer values are then adjusted such that most of the light is directed into the first order vortex mode. The next section will discuss how these modes are created on an SLM.

2.1.3 Hologram generation

SLMs can only modulate the phase of a given field and so the transmission function for the SLM is

$$t = \exp\left(i\mathrm{H}\right), \tag{2.5}$$

where H is the hologram. For certain simple cases, one can work out the required hologram quite easily. Say that a field V is incident on the SLM and we require the field to be described by

$$\mathrm{V}\exp(i\ell\phi) \tag{2.6}$$

after modulation. The required hologram would be $\mathrm{H} = \ell\phi \mod 2\pi$. The SLM is not completely efficient and so there is always some light which is left unmodulated. We must separate out our modulated field from this unmodulated component, otherwise the field after the SLM would be the superposition

$$\mathrm{V}\exp(i\ell\phi) + \text{ unmodulated light.} \tag{2.7}$$

To mitigate this, a diffraction grating

$$g(x,y) = 2\pi\left(G_x x + G_y y\right) \tag{2.8}$$

with grating frequencies G_x and G_y must be added to the hologram in order to separate the modulated light from the original axis. Thus the actual hologram would be

$$\mathrm{H} = \ell\phi + 2\pi\left(G_x x + G_y y\right) \mod 2\pi. \tag{2.9}$$

However, a different encoding scheme is required to achieve amplitude modulation as well. In this dissertation, the Arrizón type 3 encoding scheme was used for all beam shaping. The discussion below summarises the results presented in Ref.[75] The desired field is $\mathrm{V} = A(x,y)\exp(i\Psi(x,y))$ where A is the amplitude and Ψ the phase. We are looking for a hologram H such that $t(A,\Psi) = \exp(i\mathrm{H}(A,\Psi)) = A(x,y)\exp(i\Psi(x,y))$. A useful "trick" is to represent the transmission function t in a Fourier expansion

$$t(A,\Psi) = \sum_n t_n(A)\exp(in\Psi), \tag{2.10}$$

with

$$t_n(A) = \frac{1}{2\pi}\int_{-\pi}^{\pi} \mathrm{d}\Psi\ \exp\left(i\mathrm{H}\left[A,\Psi\right]\right)\exp(-in\Psi). \tag{2.11}$$

Requiring the modulated field be found in the first order sets $n = 1$ and

$$t_n(A) = \mathcal{C}A \tag{2.12}$$

for a positive constant $\mathcal{C}$. Expanding the integrand in Eq. 2.11 gives

$$t_n(A) = \frac{1}{2\pi}\int \mathrm{d}\Psi\ \cos\left(\mathrm{H}\left[A,\Psi\right] - n\Psi\right) + \frac{i}{2\pi}\int \mathrm{d}\Psi\ \sin\left(\mathrm{H}\left[A,\Psi\right] - n\Psi\right). \tag{2.13}$$

Since Eq. 2.12 only has real values, we see that

$$\mathcal{C}A = \frac{1}{2\pi}\int \mathrm{d}\Psi\ \cos\left(\mathrm{H}\left[A,\Psi\right] - \Psi\right), \tag{2.14}$$

$$0 = \frac{1}{i2\pi}\int \mathrm{d}\Psi\ \sin\left(\mathrm{H}\left[A,\Psi\right] - \Psi\right). \tag{2.15}$$

Arrizón proposed that we look for a solution of the form

$$\mathrm{H}(A,\Psi) = f(A)\sin(\Psi). \tag{2.16}$$

This ansatz has the Fourier expansion

$$\exp\left(if(A)\sin(\Psi)\right) = \sum_{m} J_m(f(A))\exp(im\Psi), \tag{2.17}$$

where $J_m(\cdot)$ is the mth Bessel function of the first kind. Such an expansion is known as Jacobi–Anger identity.[76] Again, requiring the modulated field to appear in the first order sets $m = 1$ and $t_1(A) = \mathcal{C}A = J_1(f(A))$. This means that $f(A) = J_1^{-1}(\mathcal{C}A)$. If the amplitude A of the field is normalised such that $A \in [0, 1]$ then we can set $\mathcal{C} = 1$. Thus, the required hologram is given by

$$t(A, \Psi) = \exp\left[if(A)\sin\left(\tilde{\Psi}\right)\right], \tag{2.18}$$

$$f(A) = J_1^{-1}(A), \tag{2.19}$$

$$\tilde{\Psi} = \Psi + 2\pi\left(G_x x + G_y y\right) \mod 2\pi. \tag{2.20}$$

Fig. 2.3 shows an exemplar case of using this encoding technique to generate greyscale holograms. Top row: the left panel shows the intensity pattern for a Laguerre-Gaussian beam with a radial index of 1 and azimuthal index of 2. The middle panel shows a hologram generated with no phase grating whereas a grating is present in the hologram on the far right. The characteristic "fork" dislocation of OAM beams can be seen in this hologram. Bottom row: equivalent figures are presented for a superposition of LG beams with $p = 3$ and $|\ell| = 5$.

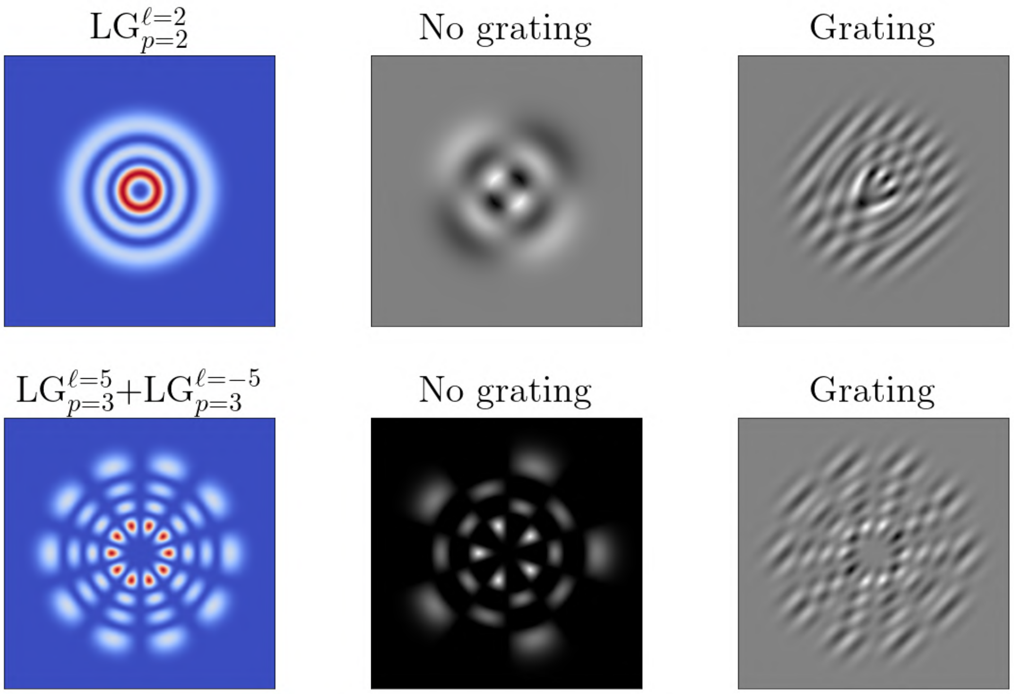

Figure 2.3: Holograms generated using the above encording technique for an LG mode with $p = 1$ and $\ell = 2$ (top row) and a superposition of modes with $p = 3$ and $\ell = \pm 5$ (bottom row). The mode's intensity pattern is shown in the leftmost panel. Holograms are shown without (middle) and with (right) phase gratings.

2.2 Digital micromirror devices

2.2.1 Principles of operation

The other device used in this thesis to modulate laser beams was a digital micromirror device (DMD). These devices consist of an array of thousands of mirrors which can turn in two different directions, allowing amplitude-only control of light. DMDs are used in digital projectors and can be adapted for structured light purposes.

DMD mirrors have access to three different positions. When the DMD is not connected to a power source, the mirrors are said to be in the 'parked' position and are flat. When powered on, the mirrors are either in the 'off' (angled $\alpha/2$ to the right from the screen's perspective) or 'on' (angled $\alpha/2$ to the left) states. Thus, an angle of α exists between the two states.

There are many diffraction orders produced by the DMD screen due to the pixelated nature of the screen. There will be one order much brighter than the others, known as the zeroth order. This order will be used to align the DMD in the following procedure. All mirrors are initially put into the off-state by displaying a hologram where all pixel values are set to 0. The DMD is then physically rotated in its mount so that the zero diffraction order is co-linear with the initial beam. This means that the mirrors are perpendicular to the incident light. After this coarse alignment one displays a hologram on the DMD to generate an LG mode with $\ell = 1$ and $p = 0$ and the required grating. This results in the LG mode appearing in the first diffraction order of the zeroth diffraction order. One should note that there are two different diffraction processes occurring: one is due to the pixelated screen of the DMD and the other from the hologram itself. The fine alignment controls of the amount are then adjusted so that the modulated first order (in which our desired beam appears) is correctly aligned with the experimental set-up.

DMDs are quite inefficient. They achieve a maximum efficiency of 62% before the application of a hologram. Once a hologram with a diffraction grating is displayed this efficiency drops to 6.2%. This efficiency can drop even further when other functions are included in the hologram which decrease the number of mirrors in the on-state.[77]

2.2.2 Hologram generation

The hologram generation procedure presented for liquid crystal SLMs can not apply to the amplitude only DMDs. For this reason, a different encoding scheme is required. The following discussion follows Ref.[78] closely. The transmission function for the DMD screen is mathematically represented (in one dimension) as

$$t(x) = \sum_n \operatorname{rect}\left(\frac{x-(n+p)x_0}{wx_0}\right), \tag{2.21}$$

where $\operatorname{rect}(\cdot)$ is the rectangle function

$$\operatorname{rect}(x) = \begin{cases} 1, & \text{for } |x| \le \frac{1}{2}, \\ 0, & \text{otherwise.} \end{cases} \tag{2.22}$$

The parameters p, w and x_0 set the position, width and period of the rectangles (mirrors), respectively. The rectangle function takes the argument x/w_x for $n = p = 0$ which shows that w controls the width of the rectangle.

In a similar step to the SLM hologram derivation, we expand this periodic transmission function in a Fourier sum

$$t(x) = \sum_n t_n \exp\left(i2n\pi \frac{x}{x_0}\right), \tag{2.23}$$

where the expansion coefficients t_n are given by

$$t_n(p, w) = \int \mathrm{d}x \ \operatorname{rect}\left(\frac{x - px_0}{wx_0}\right) \exp\left(-i2\pi \frac{x}{x_0}\right). \tag{2.24}$$

The integration bounds are determined by finding the $n = 0$ rectangle extent. This rectangle is 0 at $x_- = px_0 - wx_0/2$ and at $x_+ = px_0 + wx_0/2$ so

$$t_n(p, w) = \int_{x_-}^{x_+} \mathrm{d}x \ \exp\left(-i2\pi n \frac{x}{x_0}\right) = \frac{\exp(i2\pi np)\sin(\pi nw)}{\pi n}. \tag{2.25}$$

Selecting the first diffraction order ($n = 1$) to form the desired field $\mathrm{V} = A\exp(i\Psi)$ sets

$$t_1(p, w) = \frac{\sin(\pi w)}{\pi} \exp(i2\pi p) = A\exp(i\Psi), \tag{2.26}$$

for $A \in [0, 1]$. Equating amplitude and phase terms yields the following expressions:

$$w = \frac{1}{\pi} \arcsin(A), \tag{2.27}$$

$$p = \frac{1}{2\pi}\Psi. \tag{2.28}$$

Substituting these expressions into Eq. 2.21 will produce the required hologram. If we extend the analysis to the y direction as well, we arrive at the expression for a hologram

$$t(x, y) = \frac{1}{2} + \frac{1}{2}\operatorname{sign}\left(\cos\left[2\pi p(x, y) + 2\pi g(x, y)\right] - \cos\left[\pi w(x, y)\right]\right), \tag{2.29}$$

where $\operatorname{sign}(\cdot)$ is the sign (signum) function and $g(x, y)$ is a diffraction grating.

To see that this equation indeed produces the correct hologram, we note that binary holograms are equivalent to interferograms between the desired field V and a plane wave $\exp(-i2\pi x/x_0)$ in the one dimensional case.[79] The interference between the two fields produces the intensity pattern

$$\left| A\exp(i\Psi) + \exp\left(-i2\pi\frac{x}{x_0}\right)\right|^2 = 1 + |A|^2 + 2A\cos\left(\Psi + 2\pi\frac{x}{x_0}\right), \tag{2.30}$$

where the final term is responsible for the characteristic fringe pattern seen in interferograms. We cannot turn the above expression into a binary hologram using the signum function as Eq. 2.30 is always positive. However, the peaks of the fringes occur when

$$\cos\left(\Psi + 2\pi\frac{x}{x_0}\right) = 1 \implies \Psi + 2\pi\frac{x}{x_0} = 2\pi \times \text{ integer.} \tag{2.31}$$

These peaks will correspond to mirrors in the 'on' state. We must pick an applicable bias function $b(x) = \cos(\pi w(x))$ to modulate the difference

$$\cos\left(\Psi + 2\pi\frac{x}{x_0}\right) - b(x), \tag{2.32}$$

so that amplitude information can also be included in the hologram, as Eq. 2.31 depends only on the phase and grating. Looking at the Fourier expansion in Eq. 2.23, we picked the $n = 1$ term so we set $w(x) = \arcsin(A(x))/\pi$. This will correctly include the desired amplitude information of the mode $A\exp(i\Psi)$.

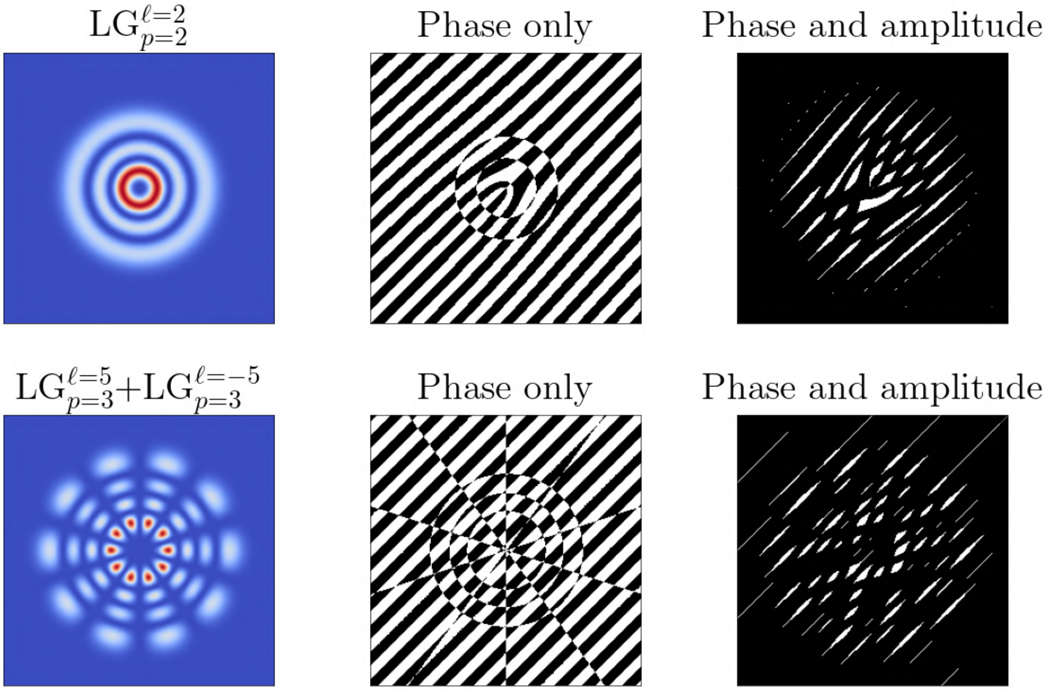

Figure 2.4: Binary holograms for LG modes (see left column) are generated according to Eq. 2.29. The right and middle panels are holograms with and without amplitude information, respectively.

Fig. 2.4 shows binary holograms for a DMD for the same LG modes in Fig. 2.3. The amplitude term $\cos(\pi w(x, y))$ in Eq. 2.29 is neglected in the "phase only" hologram displayed in the middle of Fig. 2.4, and is included in the right column.

2.3 Optically performing the overlap integral

The final experimental topic discussed in this chapter is the procedure of modal decomposition, which hinges on the evaluation of an overlap integral or inner product. Given a complete, orthonormal set of basis functions $\{\Phi_j\}$ with an inner product defined by

$$\langle \Phi_i | \Phi_j \rangle = \int \mathrm{d}^2\mathbf{r}\ \Phi_i^*(\mathbf{r})\Phi_j(\mathbf{r}) = \delta_{ij}, \quad \mathbf{r} = (x, y), \tag{2.33}$$

we can describe an arbitrary function $f(\mathbf{x})$ as the linear superposition

$$f(\mathbf{r}) = \sum_j c_j \Phi_j(\mathbf{r}), \tag{2.34}$$

provided f is sufficiently well-behaved. The expansion coefficients are determined by

$$c_j = \langle \Phi_j | f \rangle . \tag{2.35}$$

We note that the inner product in Eq. 2.33 is proportional to evaluating the Fourier transform of the product $\Phi_j^* f$ at the frequency $\boldsymbol{\nu} = \mathbf{0}$, or mathematically

$$|c_j|^2 = |\langle \Phi_j | f \rangle|^2 \propto \left| \mathcal{F}\left\{\Phi_j^* f\right\}\Big|_{\boldsymbol{\nu}=\mathbf{0}} \right|^2. \tag{2.36}$$

We can therefore extract the norm of the coefficients by measuring the on-axis ($\boldsymbol{\nu} = \mathbf{0}$) intensity of the far field of the product $\Phi_j^* f$ (recall that $\boldsymbol{\nu} = k\mathbf{r}/z$). However, this was only true in the far field, and the quadratic phase term $\exp\big(ik(r')^2/2z\big)$ is still present in Eq. 1.24 where $\mathbf{r}'$ is the transverse coordinate in the near (initial) field. This factor can be removed without needing to propagate a distance $z \gg \|\mathbf{r}'\|$ by introducing a lens. The physical effect of a lens can be expressed as a phase-only transmission function

$$t_{\text{lens}}(\mathbf{r}) = \exp\left(-\frac{ikr^2}{2f}\right), \tag{2.37}$$

for a lens of focal length f.[73] Consider a field $\mathrm{V}(\mathbf{r}_0, z = 0)$ at the plane $z = 0$, placed a distance f behind a lens with spatial coordinates $\mathbf{r}_f$. The field at the plane $z = f$ is equal to the convolution (see Eq. 1.24)

$$\mathrm{V}(\mathbf{r}_0, 0) \circledast h(\mathbf{r_f}, f) = \int \mathrm{d}^2\mathbf{r}_0\ \mathrm{V}(\mathbf{r}_0, 0) h(\mathbf{r_f} - \mathbf{r}_0, f) \tag{2.38}$$

for the impulse response of free space

$$h(\mathbf{r}, z) = \frac{\exp(ikz)\exp\left(ikr^2/2z\right)}{i\lambda z}. \tag{2.39}$$

After passing through the lens at $z = f$, the field is the product of Eq. 2.38 and Eq. 2.37, which removes a quadratic phase factor, equivalent to the application of the Frauenhofer approximation. Propagating a further focal length to the plane $z = 2f$ gives us

$$\frac{\exp(ikf)\exp\left(ikr_{2f}^2/2f\right)}{i\lambda f} \mathcal{F}\left\{\mathrm{V}(\mathbf{r}_0, 0) \circledast h(\mathbf{r_f}, f)\right\} \tag{2.40}$$

where we used Eq. 1.26. This reduces to the product

$$\frac{\exp(ikf)\exp\left(ikr_{2f}^2/2f\right)}{i\lambda f}\mathcal{F}\left\{\mathrm{V}(\mathbf{r}_0,0)\right\}\mathcal{F}\left\{h(\mathbf{r_f},f)\right\} \tag{2.41}$$

using the convolution property of the Fourier transforms. Finally, evaluating the Fourier transform of the impulse response removes the quadratic factors and leaves

$$\frac{\exp(ik2f)}{i\lambda f}\mathcal{F}\left\{\mathrm{V}(\mathbf{r}_0,0)\right\}. \tag{2.42}$$

The Fourier transform of the field V appears one focal length after the lens, provided that V is located one focal length behind it. We use this technique to obtain the expansion coefficients $|c_j|^2$ by measuring the on-axis intensity (proportional to the square of the field) of the product $\Phi_j^*\mathrm{V}$ after it has passed through a lens.

We extract the phase of the (generally) complex coefficients by measuring certain superpositions according to the following procedure.[80] Pick a reference mode Φ_0 where we set $c_0 = |c_0|$. Suppose we would like to measure the phase of the expansion coefficient $c_j = |c_j|\exp(i\theta)$. Two measurements (in addition to measuring $|c_j|^2$ according to the above method) are required. These are

$$I_{\cos} = |\left\langle \Phi_0 + \Phi_j \middle| V \right\rangle|^2 = |c_0|^2 + |c_j|^2 + 2|c_0||c_j|\cos(\theta) \tag{2.43}$$

and

$$I_{\sin} = |\left\langle \Phi_0 + i\Phi_j \middle| V \right\rangle|^2 = |c_0|^2 + |c_j|^2 + 2|c_0||c_j|\sin(\theta). \tag{2.44}$$

These additional two measurements permit the calculation of θ from

$$\theta = \arctan\left(\frac{I_{\sin} - |c_j|^2 - |c_0|^2}{I_{\cos} - |c_j|^2 - |c_0|^2}\right). \tag{2.45}$$

Fig. 2.5 illustrates the experimental procedure for performing a modal decomposition. A field U passes through an SLM (or DMD, see Chapter 2), on which a hologram of the basis state Φ_j^* is displayed. Immediately after the SLM the field is the product $\Phi_j^*\mathrm{V}$. This field passes through a lens and the on-axis intensity is measured on a camera.

2.3.1 Correction factors

When performing a modal decomposition experimentally, it is important to apply 'correction factors'. The amplitude of the projection state Φ_j^* is rescaled to be between 0 and 1 for hologram generation. The result is that instead of evaluating the inner product

$$c_j = \left\langle \Phi_j \middle| \mathrm{V} \right\rangle, \tag{2.46}$$

we actually evaluate

$$\tilde{c}_j = \frac{1}{\mathcal{M}_j}\left\langle \Phi_j \middle| \mathrm{V} \right\rangle = \frac{c_j}{\mathcal{M}_j}, \tag{2.47}$$

where $\mathcal{M}_j = \max\{|\Phi_j|\}$ is the maximum value the amplitude attains. We must multiply our measured coefficients $\tilde{c}_j$ by this $\mathcal{M}_j$ to obtain the true c_j.

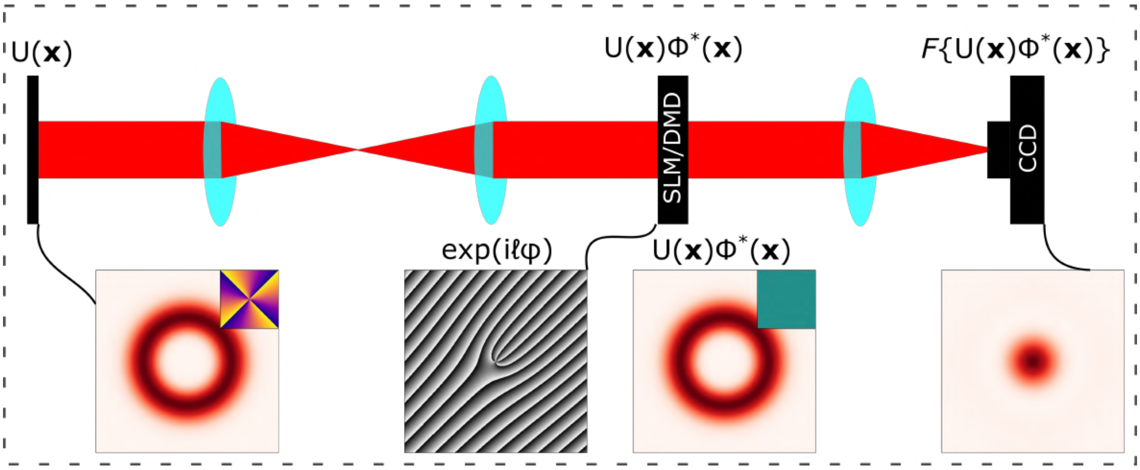

Figure 2.5: The overlap of a field U and basis state Φ is determined by displaying a hologram of Φ^* on an SLM/DMD on which the field U is incident. In this case, the state $\Phi = \exp(i\ell\phi)$ "unwraps" the helical phase of the initial field which results in a strong on-axis intensity in the far field. Insets in the top right corner show the phase of the field and the greyscale image is the hologram.

There is another type correction factor when working with the so-called 'OAM' basis. These are phase-only functions $\exp(i\ell\phi)$ which do not form a complete basis. However, they can still be used to extract the OAM content of a field V. A field V can be expanded in the as

$$\mathrm{V}(\mathbf{r},0) = \sum_{\ell} c_\ell R_\ell(r) \exp(i\ell\phi). \tag{2.48}$$

In the laboratory, we would measure

$$\tilde{c}_\ell \propto \int \mathrm{d}^2\mathbf{r}\ \exp(-i\ell\phi)\mathrm{V}(r,\phi) \propto c_\ell \int \mathrm{d}r\ rR_\ell(r) \tag{2.49}$$

due to the orthogonality of the OAM basis functions. The correction factor which must be applied in this case is

$$\frac{1}{\int \mathrm{d}r\ rR_\ell(r)}. \tag{2.50}$$

We obtain these correction factors by sending pure OAM vortex modes $\exp(i\ell\phi)$ through the channel/system and measuring their overlaps. This produces the upper crosstalk matrix in Fig. 2.6. As evidenced by the figure, the zero OAM mode has the largest on-axis intensity. This occurs because the modes have the same size but larger OAM modes have larger vortices and thus regions of null intensity, and so they carry less power. Taking the inverse of the diagonal of this matrix gives us our correction factors. The corresponding calibration matrix and correction factors are also presented for LG modes with $p = 0$. Here, we witness the opposite behaviour: the Gaussian beam has the lowest on-axis intensity. This is because the beam size increases with mode order and larger modes will have larger powers since the SLM/DMD removes the normalisation of the modes. The data presented in Fig. 2.6 was taken by propagating the pure OAM modes a distance of 2 metres and then taking the modal overlap in the same basis.

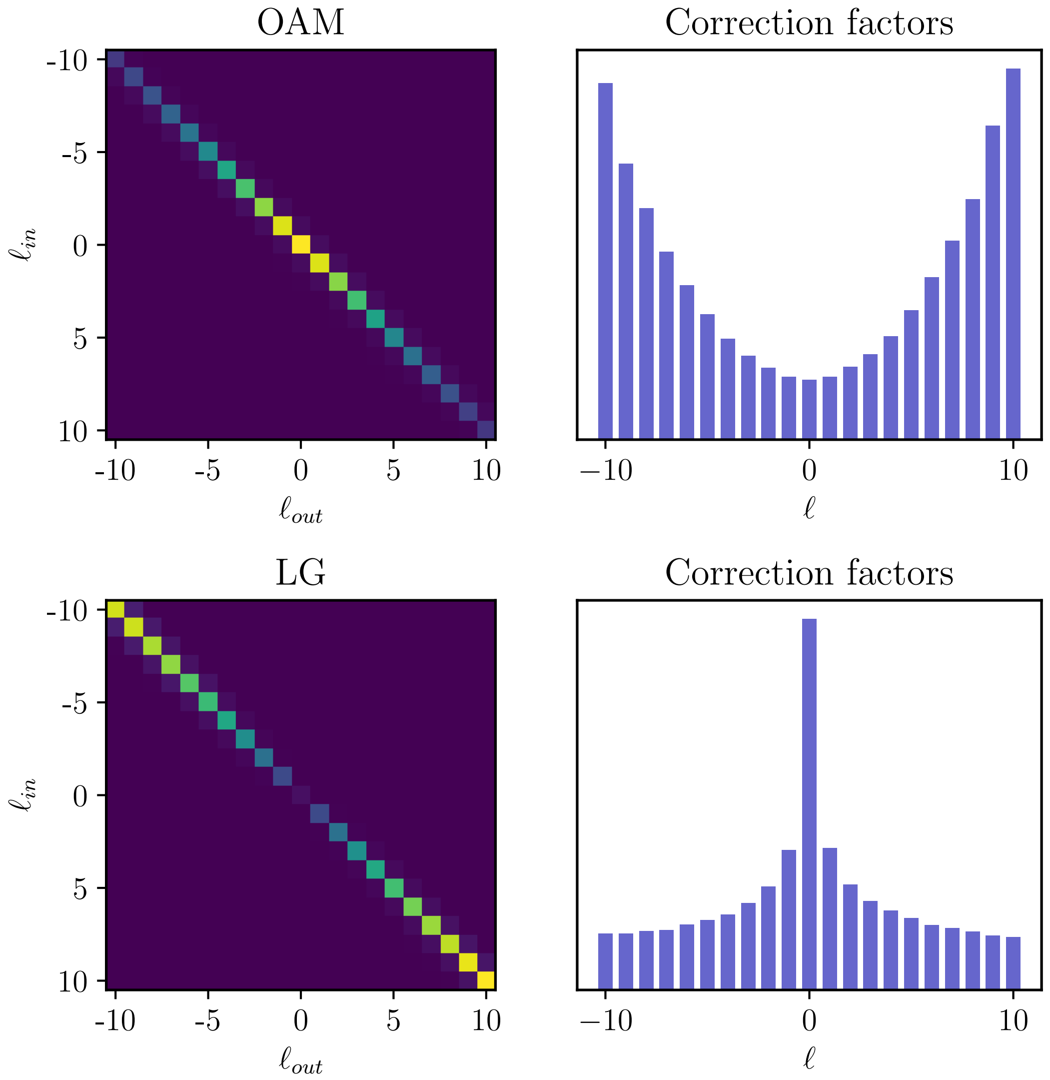

Figure 2.6: The OAM crosstalk matrix and corresponding correction coefficients are presented in the top row and show that lower order modes carry more power. This is not due to the hologram generation procedure but occurs because these modes do not form a complete basis in the transverse plane. The equivalent LG matrix and corrections are presented in the bottom row.

Chapter 3

Turbulence theory

The Earth's atmosphere interacts with propagating structured light fields. Usually, this interaction introduces non-trivial and non-negligible aberrations into the beam. A calm, still sky (as it appears to us) can still cause significant distortions and unwanted effects. This phenomenon is the result of refractive index fluctuations, with scattering and absorption of the light often being negligible for optical wavelengths. In this chapter, the statistics of atmospheric turbulence are presented according to Kolmogorov's theory and used to model the interaction with structured light fields. We explain the thin phase screen approximation which models weak turbulence effects and discuss different methods used for generating these turbulent screens. We then extend this to the strong turbulence regime and show how turbulence of any strength can be simulated using these phase screens. These screens are used to simulate turbulence in the laboratory and so the chapter concludes by explaining the procedure used to calibrate these screens, ensuring that the strength we encode is indeed the same strength that the optical fields experience.

3.1 Atmospheric statistics

The atmosphere, like any fluid, can exhibit turbulent behaviour. Normally, turbulence in a fluid is characterised by the Reynold's number

$$\mathrm{Re} = \frac{vL}{\eta}, \tag{3.1}$$

where v is the speed of the fluid, L is some characteristic length scale and η is the kinematic viscosity. High Reynold's numbers are associated with strong turbulence, whereas low numbers are associated with laminar flow characterised by smooth, constant motion. Describing atmospheric turbulence from first principles would require the use of the Navier-Stokes equations which are notoriously difficult and intricate to solve. For these reasons, Kolmogorov[81] developed a theory of atmospheric turbulence founded on physical insight and dimensional analysis. This theory was then further developed by Obukhov[82] and Corrsin[83] who extended Kolmogorov's theory into various wavenumber ranges where convective effects are not negligible (unlike in Kolmogorov's model). Ref.[83] developed spectral functions for these cases and showed how locally non-isotropic random fields can be treated as isotropic in the intermediate wavenumber range.

Kolmogorov reasoned that there is a flow of energy or energy 'cascade' between different length scales, starting for an outer scale L_0 and ending at an inner scale l_0. This range is called the inertial sub-range. At the large scale, fluctuations in wind flow cause the formation of turbulent eddies which break up into smaller eddies, transferring energy to smaller length scales. From dimensional analysis, Kolmogorov found that the velocity of the eddy was related to its length scale R according to

$$v \propto R^{1/3}. \tag{3.2}$$

The structure function, which depends on the square of the field (see Appendix A.1), picks up a factor of R so that

$$\mathcal{D}_{\text{wind}}(R) = C_V^2 R^{2/3}, \quad l_0 \ll R \ll L_0, \tag{3.3}$$

where the velocity structure constant C_V^2 is related to the energy dissipation rate ϵ according to

$$C_V^2 = 2\epsilon^{2/3}. \tag{3.4}$$

Kolmogorov's fluid theory can then be extended to temperature (T) fluctuations, even though there is no cascade of energy in this model.[69] Extending the theory directly yields a structure function for temperature fluctuations of the form

$$\mathcal{D}_T(R) = \begin{cases} C_T^2 l_0^{-4/3} R^2 & 0 \leq R \ll l_0, \\ C_T^2 R^{2/3} & l_0 \ll R \ll L_0. \end{cases} \tag{3.5}$$

These temperature fluctuations give rise to refractive index n fluctuations in the atmosphere, pictured in Fig. 3.1. These variations in the refractive index are known as optical turbulence and it is precisely this type of turbulence which we refer to as 'atmospheric turbulence'. A laser beam will accumulate a random phase as it propagates through this random refractive index field, which manifests as optical distortions and aberrations. It is thus important to quantify and characterise these refractive index variations. The refractive index n does not form a statistically homogeneous and isotropic field. However, if we split the refractive index between its mean value of 1 and a randomly varying component

$$n(\mathbf{R}) = 1 + \delta n(\mathbf{R}), \tag{3.6}$$

where $\langle \delta n \rangle = 0$, then we can make use of all the statistical functions defined in Appendix A.1. The statistics of δn will form the focus of this discussion.

We note that δn is related to the temperature T and pressure P of the atmosphere according to[69]

$$\delta n(\mathbf{R}) \approx 79 \times 10^{-6} \frac{P(\mathbf{R})}{T(\mathbf{R})}. \tag{3.7}$$

Fluctuations in pressure are negligible compared to those in temperature and so T forms the dominant contribution to δn. Thus, the statistics of δn will closely follow those of T. In light of this strong dependence on temperature fluctuations, we posit that the refractive index structure function has the following form (Eq. A.3)

$$\mathcal{D}_n(R) = \begin{cases} C_n^2 l_0^{-4/3} R^2 & 0 \leq R \ll l_0, \\ C_n^2 R^{2/3} & l_0 \ll R \ll L_0. \end{cases} \tag{3.8}$$

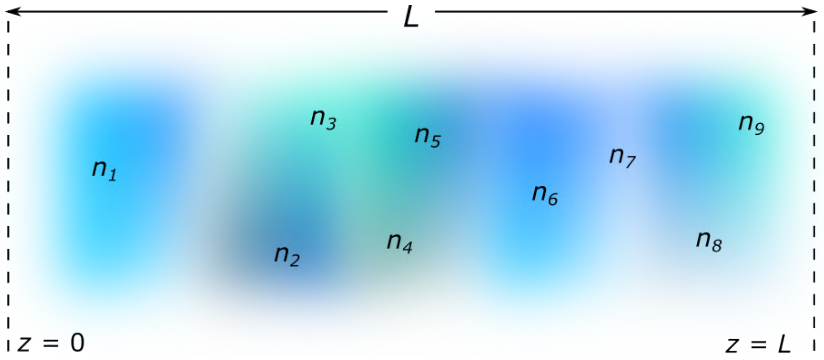

Figure 3.1: The refractive index of the atmospheres varies randomly, both along the propagation path of length L and within the transverse plane. This variance in the refractive index is known as optical turbulence.

The quantity C_n^2 is known as the refractive index structure constant and has units of length$^{-2/3}$. It is an indication of the strength of the fluctuations i.e. the larger the value, the greater the turbulence strength. We determine it from

$$C_n^2 = \left(79 \times 10^{-6}\frac{P}{T}\right)^2 C_T^2 \tag{3.9}$$

where C_T^2 is the temperature structure constant.

Working only within the inertial subrange ($l_0 \ll R \ll L_0$) and using Eq. 3.8, we derive the power spectral density of refractive index fluctuations within the Kolmogorov model (see Appendix A.2)

$$\Phi_n(k) = 0.033C_n^2 k^{-11/3}, \quad \frac{1}{L_0} \ll k \ll \frac{1}{l_0}. \tag{3.10}$$

To ensure the applicability of this model over all wavenumbers, it is common to set $l_0 \rightarrow 0$ and $L_0 \rightarrow \infty$. This expression contains infinities when integrating over its range of allowed frequencies, and this has prompted the development of more "manageable" power spectral density functions. These are presented below for the sake of completeness but are *not* used throughout this dissertation. They are the Tatarskii[84]

$$\Phi_n(k) = 0.033C_n^2 k^{-11/3} \exp\left(-\frac{k^2}{k_m^2}\right), \quad \frac{1}{L_0} \ll k, \; k_m = \frac{5.92}{l_0}, \tag{3.11}$$

and von Kármán

$$\Phi_n(k) = \begin{cases} 0.033C_n^2\left(k^2 + k_0^2\right)^{-11/6}, & 0 \le k \le \frac{1}{l_0}, \\ 0.033C_n^2\left(k^2 + k_0^2\right)^{-11/6} \exp\left(-\frac{k^2}{k_m^2}\right), & 0 \le k, \end{cases} \tag{3.12}$$

models, where $k_0 = 2\pi/L_0$. The second case (with the Gaussian factor) in Eq. 3.12 is known as the modified von Kármán spectrum.

In the limit of small k, the Tatarskii spectrum approximates the Kolmogorov spectrum since $\exp(x) \approx 1 + x$ for $x \ll 1$. Both of these models diverge for $k \rightarrow 0$ and this divergence is rectified in the modified von Kármán spectrum.

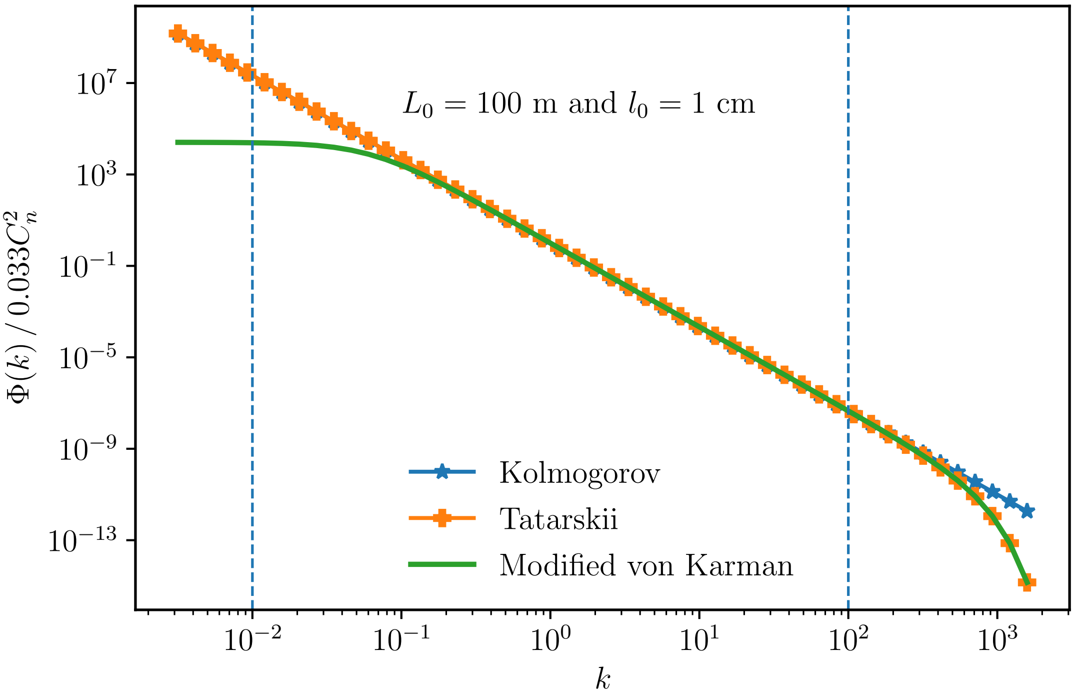

Figure 3.2: Comparison of the Kolmogorov, Tatarskii and modified von Karman power spectral density functions on a log-log plot. Dotted vertical lines indicate the inertial sub-range.

Given a refractive index structure constant alone, it can be difficult (or inconclusive) to ascertain whether the turbulence is strong or weak. This is because the wavelength of the field and the distance over which the field is propagating will naturally influence the effects of turbulence on some optical field. One can imagine that the effects of propagating over a very short distance through an atmosphere with strong fluctuations will be comparable to propagating over a further distance with weaker fluctuations. To take these effects into account, we have the Rytov variance σ_R^2 and Fried parameter r_0,[69] defined respectively as

$$\sigma_R^2 = 2.25C_n^2 k^{7/6} \int_0^z \mathrm{d}z'\ C_n^2(z')(z-z')^{5/6} = 1.23C_n^2 k^{7/6} z^{11/6}, \tag{3.13}$$

and

$$r_0 = \left(0.423k^2 \int_0^z \mathrm{d}z'\ C_n^2(z')\right)^{-3/5} = \left(0.423C_n^2 k^2 z\right)^{-3/5}, \tag{3.14}$$

which form measures of turbulence strength. Specifically, Rytov variances below ($\sigma_R^2 < 1$) and above ($\sigma_R^2 > 1$) one describe weak and strong turbulence regimes respectively. The Fried parameter r_0 is the average distance over which points in the transverse plane are correlated.[85] In both Eq. 3.13 and Eq. 3.14 it was assumed that the refractive index structure constant does not vary along the propagation path since the speed of light is much greater than the rate of change of turbulence conditions.[69]

When modelling the effects of this random refractive index contribution δn on structured light, we assume that the random field δn is delta-correlated in the z-direction (direction of propagation). This means that the refractive index variations are correlated only when looking within a plane at some z value but not between planes. This will simplify the theory by eliminating a spatial coordinate and reducing the analysis to the transverse plane. Mathematically, this is captured in the statement

$$B_n(R) = \langle \delta n(\mathbf{R}_1)\delta n(\mathbf{R}_2)\rangle = \delta(z_1 - z_2)A_n(\mathbf{r}_1 - \mathbf{r}_2) \tag{3.15}$$

where A_n is a two-dimensional covariance function. Physically, this means that the power spectral density $\Phi(k_x, k_y, k_z)$ does not depend on k_z and so we can set $k_z = 0$. To find an expression for A_n we can include this delta-correlated behaviour into Eq. A.11 which yields

$$\begin{aligned} B_n(\mathbf{R}_1, \mathbf{R}_2) &= \int \mathrm{d}k_z \exp(ik_z(z_1 - z_2)) \int \mathrm{d}^2\boldsymbol{\nu}\ \ \Phi(\boldsymbol{\nu}, 0) \exp\left(i\boldsymbol{\nu}\cdot[\mathbf{r}_1 - \mathbf{r}_2]\right) \\ &= 2\pi\delta(z_1 - z_2) \int \mathrm{d}^2\boldsymbol{\nu}\ \ \Phi(\boldsymbol{\nu}, 0) \exp\left(i\boldsymbol{\nu}\cdot[\mathbf{r}_1 - \mathbf{r}_2]\right), \end{aligned} \tag{3.16}$$

from which we read off

$$A_n(\mathbf{r}_1 - \mathbf{r}_2) = 2\pi \int_0^\infty \mathrm{d}\nu \int_0^{2\pi} \mathrm{d}\varphi\ \ \nu\Phi(\nu) \exp\left(i\nu r\cos(\varphi)\right), \tag{3.17}$$

where $\boldsymbol{\nu} = (k_x, k_y) = (\nu_x, \nu_y)$, $\nu = \|\boldsymbol{\nu}\|$ and $r = \|\mathbf{r}_1 - \mathbf{r}_2\|$. Solving the angular integral yields

$$A_n(r) = 4\pi^2 \int_0^\infty \mathrm{d}\nu\ \ \nu\Phi(\nu)J_0(\nu r), \tag{3.18}$$

where $J_0(\cdot)$ is the zeroth Bessel function of the first kind.

3.2 Optical fields in turbulence

Solving the Helmholtz equation (Eq. 1.8) will exactly determine the effects of δn on an optical field. This is usually quite difficult to do since the form of δn is not known. However, we can use perturbative methods to get approximate solutions to Eq. 1.8. We note that the fluctuations δn are small (see Eq. 3.7) and so $n^2(\mathbf{R}) \approx 1 + 2\delta n(\mathbf{R})$ where we ignore higher orders of δn. This means that Eq. 1.8 becomes

$$\left(\nabla^2 + k^2\right) \mathrm{U}(\mathbf{R}) = -2\delta n(\mathbf{R})k^2\mathrm{U}(\mathbf{R}). \tag{3.19}$$

Such an equation is readily solved by (see Eq. 1.12)

$$\mathrm{U}(\mathbf{R}) = \int \mathrm{d}^3\mathbf{R}'\ \ 2\delta n(\mathbf{R}')k^2\mathrm{U}(\mathbf{R}')\frac{\exp\left(ik\|\mathbf{R}' - \mathbf{R}\|\right)}{4\pi\|\mathbf{R}' - \mathbf{R}\|}. \tag{3.20}$$

This integral equation can prove unhelpful since one needs U in order to determine U. The Born approximation[69] gets around this issue by expanding U additively

$$\mathrm{U} = \mathrm{U}_0 + \lambda\mathrm{U}_1 + \lambda^2\mathrm{U}_2 + ..., \tag{3.21}$$

where λ is a small perturbative parameter and *not* the wavelength of the light. Similarly, we write $n = n_0 + \lambda n_1 + \ldots = 1 + \lambda \delta n$ for the refractive index. Substituting these expansions into Eq. 1.8 yields (up to second order in the perturbation)

$$\nabla^2 U_0 + \lambda \nabla^2 U_1 + \lambda^2 U_2 + k^2 U_0 + \lambda k^2 U_1 + \lambda^2 k^2 U_2 = -2\lambda \delta n k^2 U_0 - 2\lambda^2 \delta n k^2 U_1. \tag{3.22}$$

Collecting terms of the same order in the perturbative parameter λ yields three equations

$$\left(\nabla^2 + k^2\right) U_0 = 0, \tag{3.23}$$

$$\left(\nabla^2 + k^2\right) U_1 = -2\delta n k^2 U_0, \tag{3.24}$$

$$\left(\nabla^2 + k^2\right) U_2 = -2\delta n k^2 U_1. \tag{3.25}$$

U_0 is the solution to the unperturbed Helmholtz equation ($\delta n = 0$), which corresponds to vacuum modes, like the Laguerre-Gaussian basis. Using this solution, we can get the first order correction by solving

$$U_1(\mathbf{R}) = \int d^3\mathbf{R}'\ 2\delta n(\mathbf{R}') k^2 U_0(\mathbf{R}') \frac{\exp\left(ik\|\mathbf{R}' - \mathbf{R}\|\right)}{4\pi\|\mathbf{R}' - \mathbf{R}\|} \tag{3.26}$$

and then the second order correction by using our solution of U_1

$$U_2(\mathbf{R}) = \int d^3\mathbf{R}'\ 2\delta n(\mathbf{R}') k^2 U_1(\mathbf{R}') \frac{\exp\left(ik\|\mathbf{R}' - \mathbf{R}\|\right)}{4\pi\|\mathbf{R}' - \mathbf{R}\|}. \tag{3.27}$$

Taking the ensemble average of U_1 over many instances of turbulence reveals

$$\langle U_1(\mathbf{R}) \rangle = \int d^3\mathbf{R}'\ 2\left\langle \delta n(\mathbf{R}') \right\rangle k^2 U_0(\mathbf{R}') \frac{\exp\left(ik\|\mathbf{R}' - \mathbf{R}\|\right)}{4\pi\|\mathbf{R}' - \mathbf{R}\|} = 0, \tag{3.28}$$

since $\langle \delta n \rangle = 0$. On average, there is no first order correction to the unperturbed field U_0 and we must explore the second order correction to U_0. This is difficult since one needs the covariance of the refractive index fluctuations and the first order correction U_1. This leads us to another perturbative solution method, called the Rytov approximation.[69] The final, perturbed field U is instead written as

$$U(\mathbf{R}) = U_0(\mathbf{R}) \exp\left(\psi(\mathbf{R})\right) \tag{3.29}$$

where U_0 is again the unperturbed solution to the Helmholtz equation. ψ is a complex valued quantity which describes the effects of turbulence on the field U_0.

In the weak turbulence regime ($\sigma_R^2 < 1$), turbulence is treated as a phase-only effect.[69] The Rytov perturbation ψ in this case is the imaginary transverse field

$$\psi(\mathbf{R}) = i\Theta(\mathbf{r}). \tag{3.30}$$

The transverse phase Θ captures the cumulative effect of the refractive index variations over a propagation distance z by ignoring propagation effects. Mathematically

$$\Theta(\mathbf{r}) = k \int\limits_{z'=0}^{z'=z} dz'\ \delta n(\mathbf{r}, z'). \tag{3.31}$$

This means that Θ inherits all of δn's statistics. Immediately, we can assume that Θ is statistically homogeneous and isotropic, and so we only have to consider r and not ϕ, since the direction in the transverse plane does not matter – only the path length between points is significant. The covariance function B_Θ is

$$\begin{aligned} B_\Theta(r) = \langle \Theta(\mathbf{r}')\Theta(\mathbf{r}'')\rangle &= k^2 \int \mathrm{d}z' \int \mathrm{d}z'' \ \langle \delta n(\mathbf{r}', z')\delta n(\mathbf{r}'', z'')\rangle \\ &= k^2 \int \mathrm{d}z' \int \mathrm{d}z'' \ \delta(z' - z'') A_n(r) \\ &= 4\pi z k^2 \int_0^\infty \mathrm{d}\nu \ \nu \Phi(\nu) J_0(\nu r). \end{aligned} \tag{3.32}$$

We also recognise that the function A_n is the power spectral density for the refractive index in the Kolmogorov model (since it is delta-correlated in the z direction) so we can write

$$B_\Theta(r) = 2\pi z k^2 \int \mathrm{d}^2\boldsymbol{\nu} \ \Phi_n(\boldsymbol{\nu}) \exp\left(i\boldsymbol{\nu}\cdot\mathbf{r}\right) = \int \mathrm{d}^2\boldsymbol{\nu} \ \Phi_\Theta(\boldsymbol{\nu}) \exp\left(i\boldsymbol{\nu}\cdot\mathbf{r}\right), \tag{3.33}$$

from which we read off

$$\Phi_\Theta(k) = 2\pi z k^2 \Phi_n(k) = \frac{0.49}{r_0^{5/3}} k^{-11/3}. \tag{3.34}$$

Normally, the frequency $\kappa = k/2\pi$ is used instead of the angular frequency in simulations, which means

$$\Phi_\Theta(\kappa) = \frac{0.023}{r_0^{5/3}} \kappa^{-11/3}. \tag{3.35}$$

The phase structure function $\mathcal{D}_\Theta$ can be obtained from its definition:

$$\mathcal{D}_\Theta(r) = 2 \int \mathrm{d}^2\boldsymbol{\nu} \ \Phi_\Theta(\nu) \left[1 - \cos\left(\boldsymbol{\nu}\cdot\mathbf{r}\right)\right] = 6.88 \left(\frac{r}{r_0}\right)^{5/3}. \tag{3.36}$$

Eq. 3.34 and Eq. 3.36 contain equivalent information (one can be obtained from the other) and are the most important equations used to describe the random phase Θ.

3.3 Random phase screens

This section addresses a question which hangs unanswered from the previous section: how is the random phase Θ simulated? There are two approaches; one method employs the Zernike polynomials to write an algebraic sum whereas the other samples the power spectral density of Kolmogorov turbulence.

3.3.1 Zernike polynomials

The Zernike polynomials form a set of functions which are complete over the unit disk. They are numbered by indices $(n, m) \mapsto j$ and are defined as

$$Z_n^m(\boldsymbol{\rho}) = \begin{cases} \sqrt{2(n+1)} R_n^m(\rho) \cos(m\phi), & \text{even } j, \\ \sqrt{2(n+1)} R_n^m(\rho) \sin(m\phi), & \text{odd } j, \\ \sqrt{n+1} R_n^0(\rho), & m = 0, \end{cases} \tag{3.37}$$

where

$$R_n^m(\rho) = \sum_{s=0}^{(n-m)/2} \frac{(-1)^s (n-s)!}{s!\left(\frac{n+m}{2}-s\right)!\left(\frac{n-m}{2}-s\right)!}\rho^{n-2s} \tag{3.38}$$

and $\boldsymbol{\rho}$ is a vector coordinate over the unit disk. The indices n, m are whole numbers such that their difference $n-m$ is even and $m \leq n$. For example, if $n = 5$ then we can have $m = -5, -3, -1, 1, 3, 5$ but not $m = -4, -2, 0, 2, 4$. The polynomials are numbered according to Noll,[86] where $(0,0) \mapsto 1$, $(1,1) \mapsto 2$, $(1,-1) \mapsto 3$, $(2,0) \mapsto 4$ etc. These polynomials are orthogonal with respect to the inner product

$$\frac{1}{\pi}\int \mathrm{d}^2\boldsymbol{\rho}\, Z_j(\boldsymbol{\rho}) Z_{j'}(\boldsymbol{\rho}) = \delta_{jj'}, \tag{3.39}$$

and are shown in Fig. 3.3 for $n \in [0,4]$ and $m \in [-n,n]$ and are also associated with well-known wavefront aberrations, as outlined in Table 3.1.

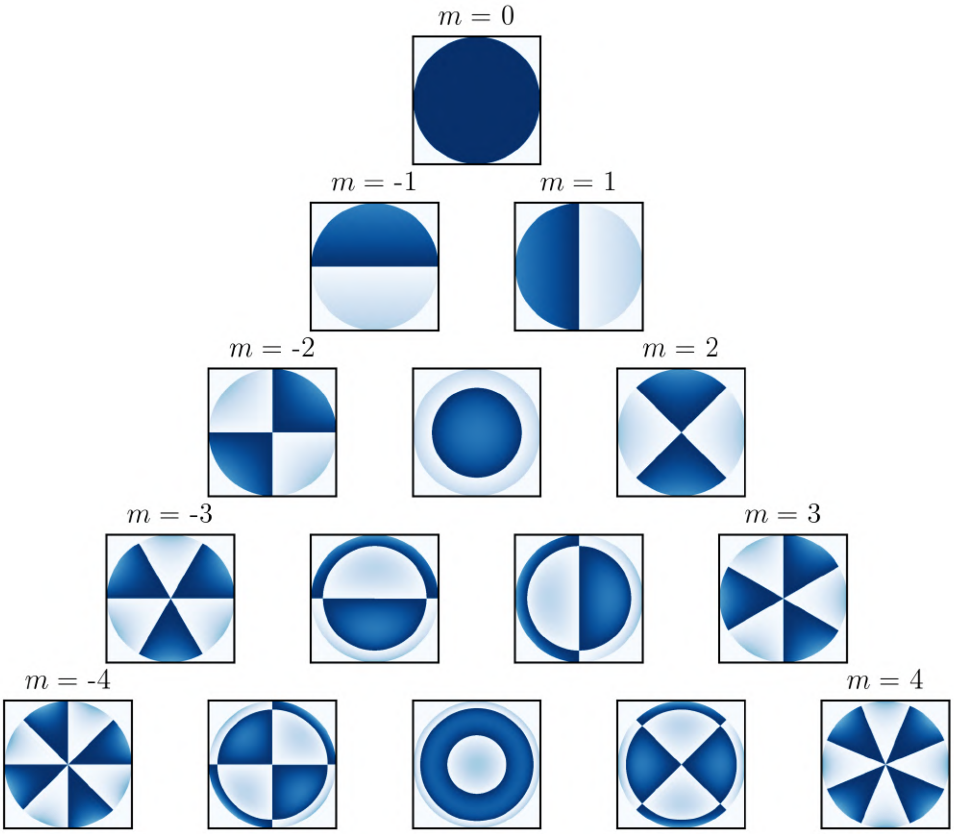

Figure 3.3: Zernike polynomials modulo 2π are plotted according to n (rows, starting from the top) and m (columns, starting from the left).

In the Fourier domain, they have the following representation

$$\begin{aligned} \mathcal{Z}_n^{+|m|}(\mathbf{k}) &= \sqrt{2}(-1)^{(n-m)/2}\cos m\varphi \\ \mathcal{Z}_n^{-|m|}(\mathbf{k}) &= \sqrt{2}(-1)^{(n-m)/2}\sin m\varphi \\ \mathcal{Z}_n^{0}(\mathbf{k}) &= (-1)^{n/2}. \end{aligned} \tag{3.40}$$

These polynomials form an excellent basis into which we can decompose the turbulent phase. The Zernike polynomials are defined only over the unit disk,

(n, m)	Aberration
$(0, 0)$	Piston
$(1, -1)$, $(1, 1)$	Tip and tilt
$(2, -2)$, $(2, 2)$	Astigmatism
$(2, 0)$	Defocus
$(3, -3)$, $(3, 3)$	Trefoil
$(3, -1)$, $(3, 1)$	Coma
$(4, 0)$	Spherical aberration

Table 3.1: The Zernike polynomials can be mapped to well-known wavefront aberrations, shown here for selected terms.

whereas the phase Θ is defined over an aperture of radius $\mathcal{R}$. The expansion then becomes

$$\Theta(\mathcal{R}\rho, \phi) = \sum_j a_j Z_j(\rho, \phi), \tag{3.41}$$

with

$$a_j = \frac{1}{\pi} \int_0^1 \mathrm{d}\rho \int_0^{2\pi} \mathrm{d}\phi \;\; Z_j(\rho, \phi) \Theta(\mathcal{R}\rho, \phi). \tag{3.42}$$

We can treat the a_j as Gaussian random variables with zero mean[86] and find their covariance by using the integral representation in Eq. 3.41

$$\left\langle a_j a_j' \right\rangle = \frac{1}{\pi^2} \int \mathrm{d}^2\boldsymbol{\rho} \int \mathrm{d}^2\boldsymbol{\rho}' \;\; Z_j(\rho', \phi') \left\langle \Theta(\mathcal{R}\rho, \phi) \Theta(\mathcal{R}\rho', \phi') \right\rangle Z_{j'}(R\rho, \phi). \tag{3.43}$$

This integral is daunting in the spatial domain but simpler in the Fourier domain due to the simple forms presented in Eq. 3.40 and using the fact that the Fourier transform of the covariance of the phase is precisely its power spectral density. Putting this all together mathematically achieves

$$\left\langle a_j a_j' \right\rangle = \int \mathrm{d}^2\mathbf{k} \int \mathrm{d}^2\mathbf{k}' \;\; \mathcal{Z}_j(\mathbf{k}') \left(0.023 \left(\frac{\mathcal{R}}{r_0} \right)^{5/3} k^{-11/3} \delta(\mathbf{k} - \mathbf{k}') \right) \mathcal{Z}_{j'}(\mathbf{k}). \tag{3.44}$$

Noll[86] solved this integral and found it to be

$$\left\langle a_j a_{j'} \right\rangle = 0.15337\, \delta_{mm'} \sqrt{(n+1)(n'+1)} (-1)^{n+n'-2n} \left(\frac{D}{r_0} \right)^{5/3} I_{nn'} \tag{3.45}$$

where

$$I_{nn'} = \frac{\Gamma\left(\frac{14}{3}\right) \Gamma\left(\left[n + n' - \frac{5}{3}\right]/2\right)}{\Gamma\left(\frac{\left[-n+n'+\frac{17}{3}\right]}{2}\right) \Gamma\left(\frac{\left[n-n'+\frac{17}{3}\right]}{2}\right) \Gamma\left(\frac{\left[n+n'+\frac{23}{3}\right]}{2}\right)} \tag{3.46}$$

is the Noll covariance matrix.

One may suppose that the phase screens Θ are generated from a sum of the Zernike polynomials whose coefficients are sampled from a Gaussian distribution with zero mean and variance equal to $\left\langle a_j a_j' \right\rangle$. However, $I_{nn'}$ will have off-diagonal terms for polynomials with the same m index but different n indices.

This means we cannot build a screen by randomly sampling the a_j from normal distributions with variance $\left\langle |a_j|^2 \right\rangle$. To sample the a_j correctly, we define $\mathbf{C}$ to be the normalised covariance matrix with elements

$$C_{ij} = \frac{\left\langle a_i a_j^* \right\rangle}{(D/r_0)^{5/3}}. \tag{3.47}$$

Since $\mathbf{C}$ is Hermitian, there exists a diagonal matrix $\mathbf{S}$ and unitary matrix $\mathbf{U}$ such that[87]

$$\mathbf{C} = \mathbf{U}\mathbf{S}\mathbf{U}^\dagger. \tag{3.48}$$

Say we are considering an expansion of Θ with $N-1$ polynomials (we do not use the polynomial Z_0^0 which is a constant). Let A be the vector of the expansion coefficients normalized by $(D/r_0)^{5/6}$

$$A = \begin{pmatrix} a_2 \\ \vdots \\ a_N \end{pmatrix}, \tag{3.49}$$

so that

$$\left\langle AA^\dagger \right\rangle = \begin{pmatrix} \left\langle |a_2|^2 \right\rangle & \cdots & \langle a_2 a_N^* \rangle \\ \vdots & \ddots & \vdots \\ \langle a_N a_2^* \rangle & \cdots & \left\langle |a_N|^2 \right\rangle \end{pmatrix} = \mathbf{C}. \tag{3.50}$$

If we define $B \equiv \mathbf{U}^\dagger A$, then

$$\left\langle BB^\dagger \right\rangle = \left\langle \mathbf{U}^\dagger AA^\dagger \mathbf{U} \right\rangle = \mathbf{U}^\dagger \left\langle AA^\dagger \right\rangle \mathbf{U} = \mathbf{U}^\dagger \mathbf{C} \mathbf{U} = \mathbf{S}. \tag{3.51}$$

This means that the elements of B are statistically independent since $\mathbf{S}$ is diagonal. Thus, the entries in B can be sampled from a normal distribution with zero mean and covariance equal to the corresponding diagonal element of $\mathbf{S}$. Finally, the actual coefficients used in the expansion of Θ are obtained by multiplying $A = \mathbf{U}B$ by $(D/r_0)^{5/6}$.

Worked example

We will generate an exemplar screen using $N = 15$ Zernike polynomials, sampled over a grid of 1024×1024 pixels with pixel spacing $\delta = 8\,\mu$m. Taking the aperture to be $D = 1024 \times 8\,\mu\text{m} = 8.192$ mm and Fried parameter $r_0 = 1.638$ mm means the turbulence strength is $D/r_0 = 5$.

The sub-block (with only 7×7 entries) of the complete normalised covariance matrix $\mathbf{C}$ (containing 15×15 entries) is

$$\begin{pmatrix} 0.4509 & 0 & 0 & 0 & 0 & 0 & -0.0142 \\ 0 & 0.4509 & 0 & 0 & 0 & 0 & 0 \\ 0 & 0 & 0.0233 & 0 & 0 & 0 & 0 \\ 0 & 0 & 0 & 0.0233 & 0 & 0 & 0 \\ 0 & 0 & 0 & 0 & 0.0233 & 0 & 0 \\ 0 & 0 & 0 & 0 & 0 & 0.0062 & 0 \\ -0.0142 & 0 & 0 & 0 & 0 & 0 & 0.0062 \end{pmatrix}, \tag{3.52}$$

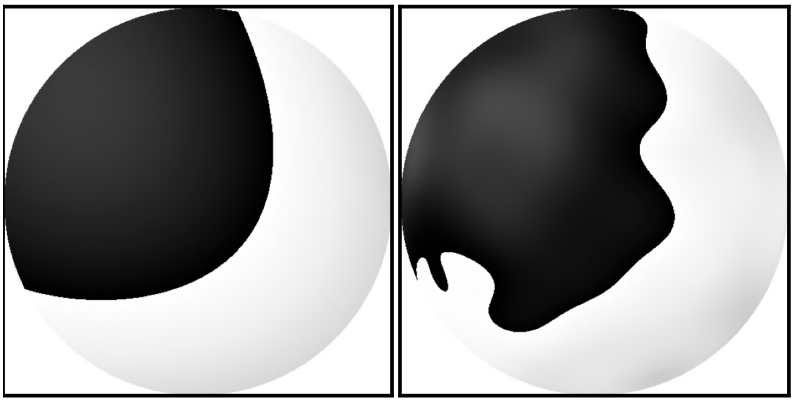

Figure 3.4: Phase screens (modulo 2π) produced using the Zernike method with 6 (left) and 100 (right) terms for a strength of $D/r_0 = 1$.

and the corresponding entries for the diagonalised matrix **S** are

$$\begin{pmatrix} 0.4514 & 0 & 0 & 0 & 0 & 0 & 0 \\ 0 & 0.4514 & 0 & 0 & 0 & 0 & 0 \\ 0 & 0 & 0.0240 & 0 & 0 & 0 & 0 \\ 0 & 0 & 0 & 0.0240 & 0 & 0 & 0 \\ 0 & 0 & 0 & 0 & 0.0240 & 0 & 0 \\ 0 & 0 & 0 & 0 & 0 & 0.0067 & 0 \\ 0 & 0 & 0 & 0 & 0 & 0 & 0.0067 \end{pmatrix}. \tag{3.53}$$

First, we must compute the vector B which is sampled from a Gaussian distribution with zero mean and variance equal to the diagonal elements of **S**. Our values for B are

$$B = \begin{pmatrix} -0.2491 \\ -0.2175 \\ -0.0057 \\ 0.0477 \\ 0.0048 \\ -0.0017 \\ 0.0375 \\ -0.0230 \\ -0.0061 \\ 0.0186 \\ -0.0060 \\ 0.0114 \\ 0.0111 \\ -0.0022 \\ 0.0163 \end{pmatrix}. \tag{3.54}$$

Then, using these values, we obtain the vector A by transforming B according to

$A = \mathbf{U}B$ so

$$A = \begin{pmatrix} 0.9514 \\ 0.8286 \\ -0.1864 \\ 0.0330 \\ -0.0075 \\ 0.0082 \\ -0.0526 \\ -0.1107 \\ -0.1375 \\ 0.0666 \\ -0.0038 \\ 0.0314 \\ 0.0181 \\ 0.0216 \\ 0.0364 \end{pmatrix}. \tag{3.55}$$

To obtain the true expansion coefficients used in Eq. 3.41, we must multiply A by $(D/r_0)^{5/6}$ for $D/r_0 = 5$, which gives

$$\begin{pmatrix} 3.6378 \\ 3.1681 \\ -0.7127 \\ 0.1262 \\ -0.0288 \\ 0.0315 \\ -0.2013 \\ -0.4231 \\ -0.5258 \\ 0.2546 \\ -0.0147 \\ 0.1199 \\ 0.0693 \\ 0.0826 \\ 0.1390 \end{pmatrix}. \tag{3.56}$$

This combination of expansion coefficients produces the phase screen shown in Fig. 3.5. The screen exhibits strongly periodic behaviour (modulo 2π), indicating that the low order terms like tip and tilt are dominating the sum. This is confirmed when looking at the first two entries in Eq. 3.56, which correspond to Z_1^1 and Z_1^{-1}, respectively.

3.3.2 Fourier transform method

The previous method generated an instance of Θ in the spatial domain. In this method, the mirror opposite approach is taken by generating an instance of Θ in the frequency domain and extracting Θ using the inverse transform. Let Θ be a function of the discretely sampled coordinate $\mathbf{r} = (x_p, y_q)$, where (p, q) are sample indices. (p, q) are sampled over N and M points, respectively. The sample

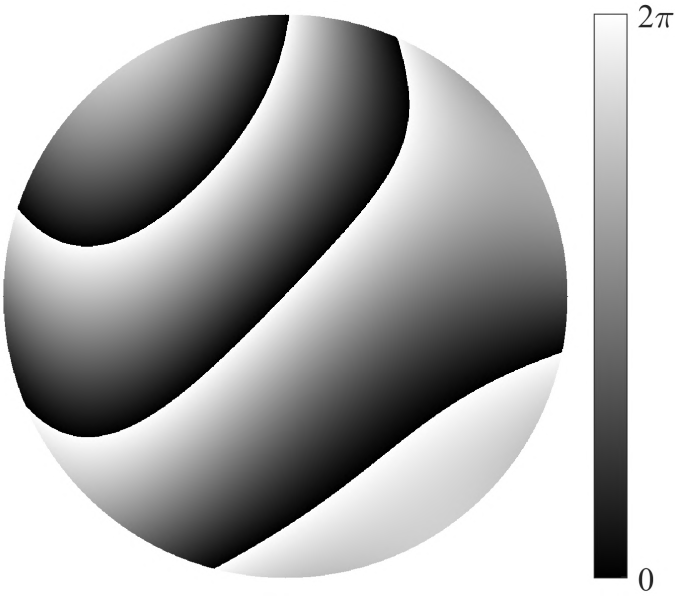

Figure 3.5: A phase screen produced from the first 15 Zernike polynomials (not including the piston term) whose expansion coefficients are given in Eq. 3.56.

spacings are δx and δy, i.e. $x_p = p\delta x$ and $y_q = q\delta y$, resulting in a grid of side lengths $L_x = N\delta x$ and $L_y = M\delta y$. We can write Θ has a Fourier series[88]

$$\Theta(x_p, y_q) = \sum_n \sum_m c_{nm} \exp\left(i2\pi\left[\frac{np}{N} + \frac{mq}{M}\right]\right). \tag{3.57}$$

Such a sum is chosen since the same form is used by programming languages like MATLAB to evaluate the Fourier transform using algorithms like the Fast Fourier Transform [89,90] (FFT).

The expansion coefficients can be obtained by inverting the sum

$$c_{nm} = \frac{1}{NM} \sum_p \sum_q \Theta(x_p, y_q) \exp\left(-i2\pi\left[\frac{np}{N} + \frac{mq}{M}\right]\right). \tag{3.58}$$

These expansion coefficients are normally distributed random variables. Their variance is given by

$$\begin{aligned}\left\langle |c_{nm}|^2 \right\rangle = \left(\frac{1}{NM}\right)^2 \sum_{pp'} \sum_{qq'} \left\langle \Theta(x_p, y_q)\Theta(x_{p'}, y_{q'}) \right\rangle \times \\ \times \exp\left(-i2\pi\left[\frac{n(p'-p)}{N} + \frac{m(q'-q)}{M}\right]\right).\end{aligned} \tag{3.59}$$

Since $B(\mathbf{r}) = \langle \Theta(\mathbf{r}' + \mathbf{r})\Theta(\mathbf{r}') \rangle$, we can simplify the above to

$$\begin{aligned}\left\langle |c_{nm}|^2 \right\rangle &= \frac{1}{NM} \sum_p \sum_q B(x_p, y_q) \exp\left(-i2\pi\left[\frac{np}{N} + \frac{mq}{M}\right]\right) \\ &= \frac{1}{L_x L_y} \Phi(k_n, l_m),\end{aligned} \tag{3.60}$$

where (k_n, l_m) is a sampled frequency vector. This means we can sample the c_{nm} from a normal distribution with mean 0 and variance $\Phi(k_n, l_m)\delta k \delta l$, since the frequency sampling spacing in the x or y direction is equal to the reciprocal of the spatial length $L_{x/y}$, respectively. The final phase screen is then obtained from Eq. 3.57. There is a drawback to this "naive" approach. The smallest sampled frequencies are $k = 1/L_x$ and $l = 1/L_y$. Frequencies with periods greater than L_x and L_y are thus not included. This means that the Kolmogorov frequency spectrum is undersampled, since the contribution from smaller frequencies is much greater as a result of the $\|\mathbf{k}\|^{-11/3}$ behaviour. These frequencies are termed "subharmonics" and must be added in to the spectrum.[91] We divide the area around the origin in frequency space into a 3×3 grid whose corners and midpoints corresponding to indices $(1/3, 0)$, $(1/3, 1/3)$, $(0, 1/3)$, $(-1/3, 1/3)$, $(-1/3, 0)$, $(-1/3, -1/3)$, $(0, -1/3)$ and $(1/3, -1/3)$. However, each of these frequencies must be weighted by a factor of $1/9$ as they occupy a ninth of the area in frequency space compared to integer indexed frequencies. This region can be further subdivided into a 3×3 grid whose indices correspond to $(1/9, 0)$ etc whose contributions must be multiplied by a factor of $1/27$. These terms are added in the following way. Let Θ_{high} be the phase obtained from the "naive" expansion in Eq. 3.57 and $F = \{-1/3^b, 0, 1/3^b\}$. The subharmonic terms are added according to

$$\Theta(x_p, y_q) = \Theta_{\text{high}}(x_p, y_q) + \sum_b \sum_{n \in F} \sum_{m \in F} c_{nm} \exp\left(-i2\pi \left[\frac{np}{3^b N} + \frac{mq}{3^b M}\right]\right), \tag{3.61}$$

where the $n = m = 0$ term is not summed and the c_{nm} are sampled from a distribution with variance

$$\left(\frac{1}{3^b}\right)^2 \frac{\Phi(k_n, l_m)}{L_x L_y} \tag{3.62}$$

The first set of subharmonic terms correspond to $b = 1$, the second set to $b = 2$ and so on. In practice, b is taken up to 5. Phase screens produced with 3 (left) and 5 (right) subharmonic orders are shown in Figure 3.6. The addition of subhamornic frequencies removes the periodicity of the screens.

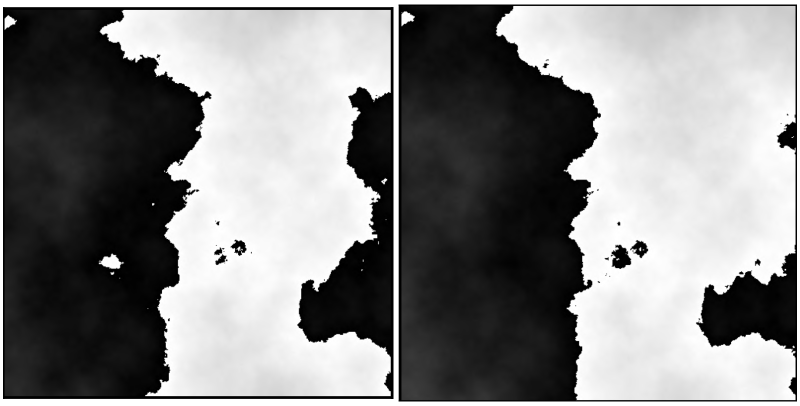

Figure 3.6: Phase screens (modulo 2π) produced using the Fourier approach with 3 (left) and 5 (middle) subharmonic orders for a strength of $D/r_0 = 1$. The periodicity seen in the left frame is removed by the further addition of subharmonic components.

3.3.3 Comparison of simulation approaches

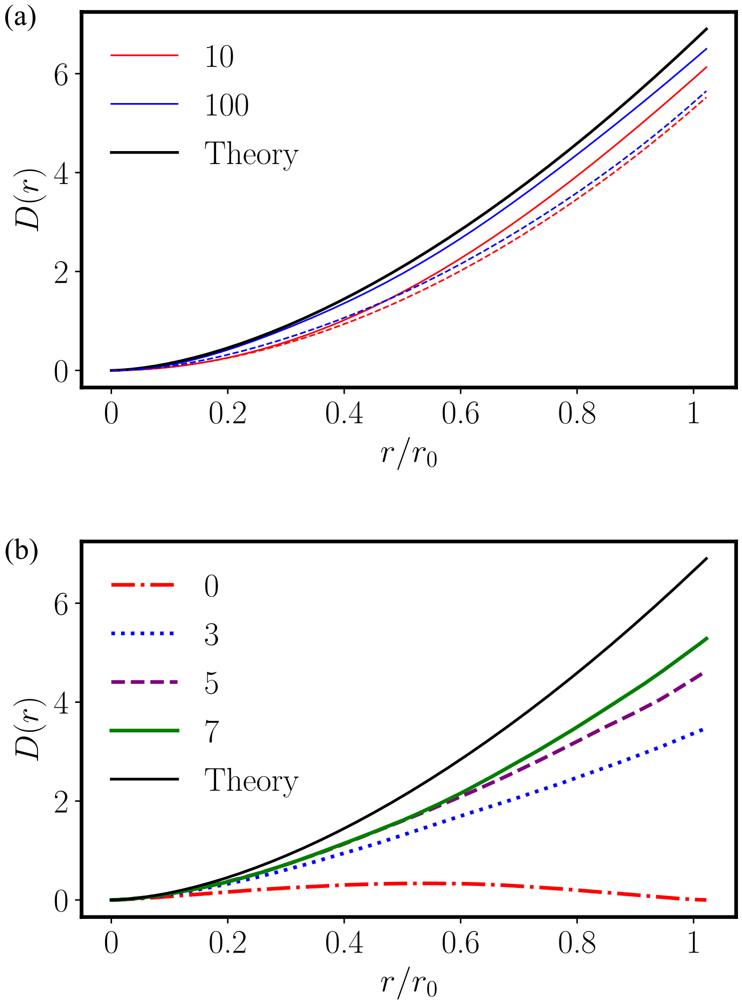

Figure 3.7: The phase structure function is computed for the (a) Zernike and (b) Fourier transform screen generation approaches. In both (a) and (b) the solid black line refers to the theoretical structure function. In (a), phase screens were computed were computed for 10 (red) and 100 (blue) Zernike polynomials. Solid and dashed lines denote the statistically independent and "naive" methods, respectively. (b) Screens with different orders of subharmonic terms (0, 3, 5 and 7) are compared against each other. The addition of subharmonics significantly increases the accuracy of the screens.

We will study four distinct phase screen generation methods: the "incorrect" Zernike method, where the coefficients are sampled directly from a distribution with variance $\langle |a_j|^2 \rangle$; the "corrected" Zernike method, using the procedure outlined above; the "naive" Fourier transform method lacking the subharmonic contribution and the subharmonic method. The phase structure function $\mathcal{D}(r)$ is evaluated for a series of screens generated using both approaches and compared to theory. The results are shown in Fig. 3.7(a) and Fig. 3.7(b) for the Zernike and Fourier approaches, respectively.

The structure function is plotted against the radius, normalized by the Fried parameter r_0. In Fig. 3.7(a), results from screens generated from the "incorrect" and correct methods are represented by dotted and solid lines, respectively. The number of Zernike terms used in the expansion are colour-coded: red for 10 terms and blue for 100 terms. We see excellent agreement with the theory (black solid line) and Zernike approach after only 10 terms. It is also evident that the direct, "incorrect" method under-evaluates the turbulence variations over the aperture, but this is corrected by following the steps outlined above.

In Fig. 3.7(b), results from phase screens generated using different numbers of subharmonic orders are shown. The Fourier approach without the subharmonic inclusions ($b = 0$) is notably inaccurate at replicating truly turbulent behaviour. However, even after 7 subharmonic orders have been included, the phase structure function (green solid line in Fig. 3.7(b)) is still recognisably different from the theoretical prediction.

3.4 Split-step method

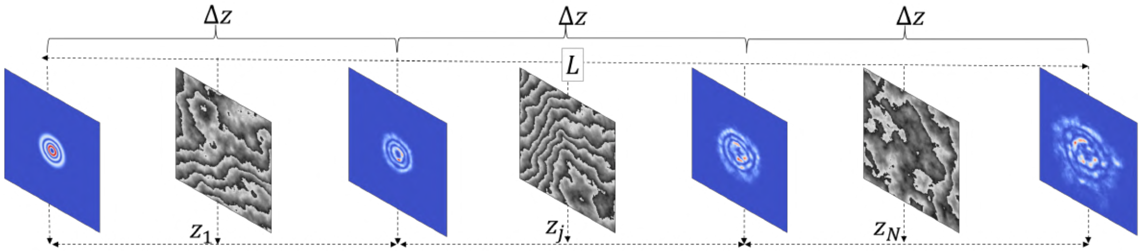

Figure 3.8: The propagation path of length L is divided into N segments, each of length Δz. The screens are placed at z_j, in the middle of each segment. This arrangement allows the thin phase screen approximation to hold in each segment while simultaneously modelling the effects of an extended medium.

Single, random phase screens model turbulence excellently in the weak regime ($\sigma_R^2 < 1$) but fail to do so for the strong scintillation regime ($\sigma_R^2 > 1$) and cannot be used to simulate turbulence. This problem is over come by dividing the path into segments such that the Rytov variance is smaller than 1 for each segment. This means that the effects of turbulence in each segment can be modelled using phase screens. This placement of screens is illustrated in Fig. 3.8, and its derivation is presented below for a channel of length L.

The Fried parameter can be discretized by converting the integral in Eq. 3.14 to the sum

$$r_0 = \left(0.423 C_n^2 k^2 \sum_{j=1}^{N} \Delta z_j\right)^{-3/5}, \tag{3.63}$$

for N segments. If each segment has an equal length $\Delta z = \Delta z_j = L/N$ and the phase screens are positioned at z_j in the middle of each "slab" we get

$$z_j = \frac{L}{2N} + \frac{L(j-1)}{N}, \tag{3.64}$$

and

$$r_0 = \left(\sum_j r_{0,j}^{-5/3} \right)^{-3/5} = N^{-3/5} r_{0,s} \tag{3.65}$$

where $r_{0,s} = N^{3/5} r_0$ is the effective Fried parameter for each segment, implying that the total Fried parameter is larger than that used in each propagation step. A similar discretisation is used to turn Eq. 3.13 into a discrete sum

$$\sigma_R^2 = 2.25 C_n^2 k^{7/6} L^{5/6} \sum_j \left(1 - \frac{z_j}{L} \right)^{5/6} \Delta z \tag{3.66}$$

which becomes

$$\sigma_R^2 = 2.25 C_n^2 k^{7/6} L^{11/6} \sum_j \frac{1}{N} \left(1 - \frac{j - 1/2}{N} \right)^{5/6} . \tag{3.67}$$

We rephrase Eq. 3.67 in terms of the Fried parameter $r_{0,s}$ to obtain

$$\sigma_R^2 = 5.32 k^{-5/6} L^{5/6} r_0^{-5/3} \sum_j \frac{1}{N} \left(1 - \frac{j - 1/2}{N} \right)^{5/6} = \sum_j \sigma_{R,j}^2 . \tag{3.68}$$

The Fried parameter is used in numerical simulations to characterise the turbulence strength (over the structure constant) and so the formulation in Eq. 3.68 proves extremely useful. The greatest contribution to the amplitude fluctuations comes from the first propagation step and decays as we get closer to the observation plane. We can use this fact to ensure that we are in the weak regime in each segment by requiring

$$\sigma_{R,1}^2 = 5.32 k^{-5/6} L^{5/6} r_0^{-5/3} \frac{1}{N} \left(1 - \frac{1/2}{N} \right)^{5/6} < 1. \tag{3.69}$$

3.5 Experimentally calibrating the phase screens

The phase screens must be calibrated to ensure that their turbulence strength is consistent with the programmed value of D/r_0. The Strehl ratio (SR) provides a convenient link between measured intensities and turbulence strength D/r_0. It is defined as the ratio of the average on axis intensity with, $\langle I(\mathbf{0}) \rangle$, and without, $I_0(\mathbf{0})$, turbulence. It has the integral form[69]

$$\mathrm{SR} = \frac{\langle I(\mathbf{0}) \rangle}{I_0(\mathbf{0})} = \frac{16}{\pi} \int_0^1 \mathrm{d}u \;\; u \left(\arccos u - u\sqrt{1 - u^2} \right) \exp \left(-3.44 \frac{uD}{r_0} \right)^{5/3} . \tag{3.70}$$

For a plane wave passing through a Gaussian lens in the Kolmogorov model, the following approximation can be used with excellent accuracy:[69]

$$\mathrm{SR} \approx \frac{1}{\left(1 + (D/r_0)^{5/3} \right)^{6/5}}, \tag{3.71}$$

where $D = \sqrt{8}w_G$ is the hard aperture of the Gaussian lens and w_G is its waist parameter.

The experimental procedure used to calibrate the phase screens is explained as follows. A range of turbulence strengths must be examined – usually $D/r_0 \in [0, 4]$ is sufficient. Then, for each turbulence strength D/r_0, M (=30 or more) turbulent screens are generated and displayed on a spatial light modulator. We illuminate the SLM with a Gaussian beam with radius w_0 and relate this parameter to the aperture D by $D = \chi w_0$. As a starting point, take $\chi = \sqrt{8} \approx 2.83$. It is likely that this parameter will need to change depending on the specific setup and the number of subharmonics used to generate the screens as these factors affect the turbulence strength that the beams in the experiment experience. A factor of $\chi = 2$ produced excellent agreement between measured and theoretical values for numerical simulations and experimental measurements for screens generated with five orders of subharmonic terms. We then pass this field through a lens which takes us to the far field and the intensity is measured on a CCD (camera). The on-axis intensity is measured for M screens, corresponding to one value of D/r_0, and this is repeated for the range of turbulence strengths. The measurements are normalised by switching off the phase screens and measuring the zero-turbulence on-axis intensity of the same Gaussian beam. The error in the measurements is calculated by dividing the standard deviation for M screens per D/r_0 value by $\sqrt{M}$. This procedure gives us a single set of measurements, which we must compare against the theoretical Strehl ratio (Eq. 3.71). Unless one is lucky, these measured values will not coincide with the theoretical ones. The factor χ the aperture D to the Gaussian beam waist and gives a new turbulence strength $\chi w_0/r_0$. This procedure is repeated for a range of χ until a sufficiently good agreement is found between the measured and theoretical values of the Strehl ratio. This can be made more rigorous by calculating the sum of the squares of the differences between the theoretical and measured values and finding the value of χ by trial-and-eror which minimises this sum. The plot in Fig. 3.9 shows results for a calibrated set of phase screens whose measured Strehl ratios (blue markers with error bars) match the programmed (theoretical) values (dotted line).

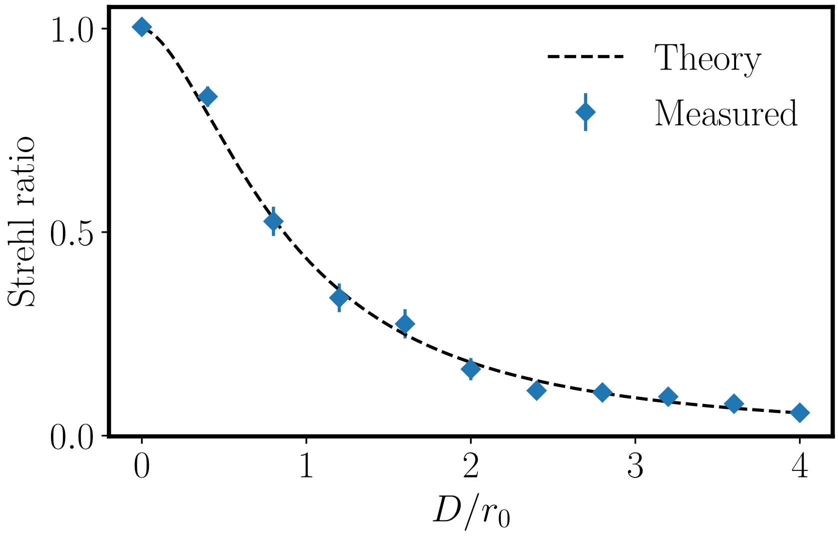

Figure 3.9: The Strehl ratio for a set of calibrated phase screens. Theoretical (programmed) values are plotted as a solid line and experimentally measured points are represented as blue markers. The parameter χ in $D = \chi w_0$ was chosen so as to minimise the difference between the measured and programmed values and one can see the excellent agreement between theory and experiment. This indicates the beams experience the same strength of turbulence as that encoded on the holograms.

Chapter 4

The orbital angular momentum of a turbulent atmosphere

The most popular beams used in communication studies are those carrying OAM, as opposed to using the full radial and azimuthal indices of LG beams. Unfortunately, turbulence causes scattering (crosstalk) between OAM modes which impairs the fidelity of a signal. Understanding this scattering is necessary for improving free space communication links.

Much research has been devoted to characterising the behaviour of OAM beams in turbulence, producing disagreement over the dependence (or lack thereof) on a beam's initial OAM in determining its behaviour as it propagates through the atmosphere. This debate is complicated further by the theoretical and experimental confirmation that both sides have received. A common theme between these studies is their focus on specific beam types, rendering their results specific to their study.

In the traditional approach to modelling structured light in the atmosphere, the optical field experiences phase distortions which then results in modal scattering. In the context of OAM, the beam has some initial OAM (which may be zero or some superposition) with modal scattering amounting to a spread in the OAM values about the initial value(s). Here, we interpret the spread in OAM as the atmosphere having imparted or removed OAM from the beam. This allows us to invert our perspective, and ignore the optical field altogether, instead bringing our attention to bear on the atmosphere itself. The question then reduces to: how much OAM is there in a turbulent atmosphere? Since turbulence is stochastic in nature, we expect the answer to be in probabilities.

4.1 Atmospheric OAM statistics

Since we are interested in the atmosphere's ability to transfer OAM with structured light fields, we will quantify the OAM using the discrete spectrum of OAM eigenmodes. We visualize a cylinder of the turbulent atmosphere, as seen in Fig. 4.1(a). The refractive index variations over the length of the cylinder can be approximated as a thin screen defined over a radius R since we are in the weak scintillation regime. We will show how we can find the probability of measuring charge ℓ in the atmosphere for a fixed turbulence strength, as seen in Fig. 4.1(b), from Θ.

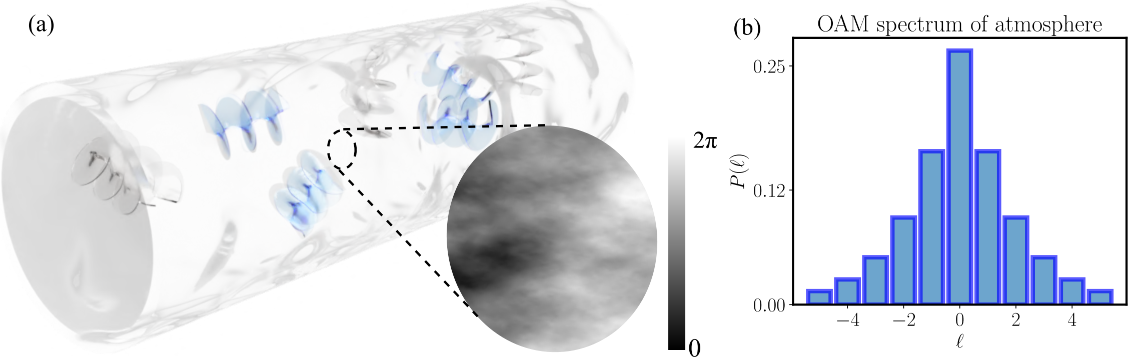

Figure 4.1: (a) A turbulent 'cylinder' of the atmosphere is visualized with spirals, reminiscent of OAM wavefronts, and can modelled as a random phase screen whose frequency spectrum exhibits the -11/3 Kolmogorov power law. (b) The probability of measuring different values of ℓ in the atmosphere is illustrated for medium turbulence.

We expand Θ into the Zernike basis as shown in Eq. 3.41, repeated here for convenience

$$\Theta(R\rho,\phi)=\sum_j a_j Z_j(\rho,\phi).$$

Decomposing the tranmission function $\exp(i\Theta)$ of the atmosphere into the OAM basis results in the following expression for the probability of measuring OAM associated with topological charge ℓ in the atmosphere, on average (see Appendix A.3):

$$P(\ell)=\frac{1}{\pi}\int \mathrm{d}^2\boldsymbol{\rho}\ \cos\left(\ell\phi\right)\exp\left(-\frac{1}{2}\mathcal{D}\left(\boldsymbol{\rho}\right)\right), \tag{4.1}$$

and so the atmosphere possesses a spread of OAM, as seen in Fig. 4.1(b).

The phase structure function function $\mathcal{D}$ is given, in this model, by

$$\mathcal{D}(\boldsymbol{\rho})=\sum_j\sum_{j'}\left\langle a_j^* a_{j'}\right\rangle \Delta Z_j(\boldsymbol{\rho})\Delta Z_{j'}(\boldsymbol{\rho}), \tag{4.2}$$

in terms of Zernike polynomials, where

$$\Delta Z_j(\boldsymbol{\rho})\equiv Z_j(\rho,\phi)-Z_j(\rho,0). \tag{4.3}$$

We can ask: how do the different terms in Eq. 4.2 contribute to the OAM spectrum of the atmosphere? The contribution to the shape of the OAM spectrum, shown in Fig. 4.2(a)–(d), is a function of $\Delta Z_j \Delta Z_j'$ alone. The modal spectrum from the tilt terms is centered around $\ell=0$, whereas that of coma introduces larger ℓ. The $\left\langle a_j a_{j'}\right\rangle$ are much larger for lower order terms, as seen in Fig. 4.2(e). As a result, higher order terms (like coma and trefoil) will contribute to measuring larger $|\ell|$ values and lower order terms will dominate overall as a result of the relative size of the coefficients.

We can use this approach to make general statements about the OAM of the atmosphere without the need to reference specific beam types.

The terms in Eq. 4.2 can be truncated to some finite sum, the limit of which is determined by the required accuracy of the model. The OAM contribution of

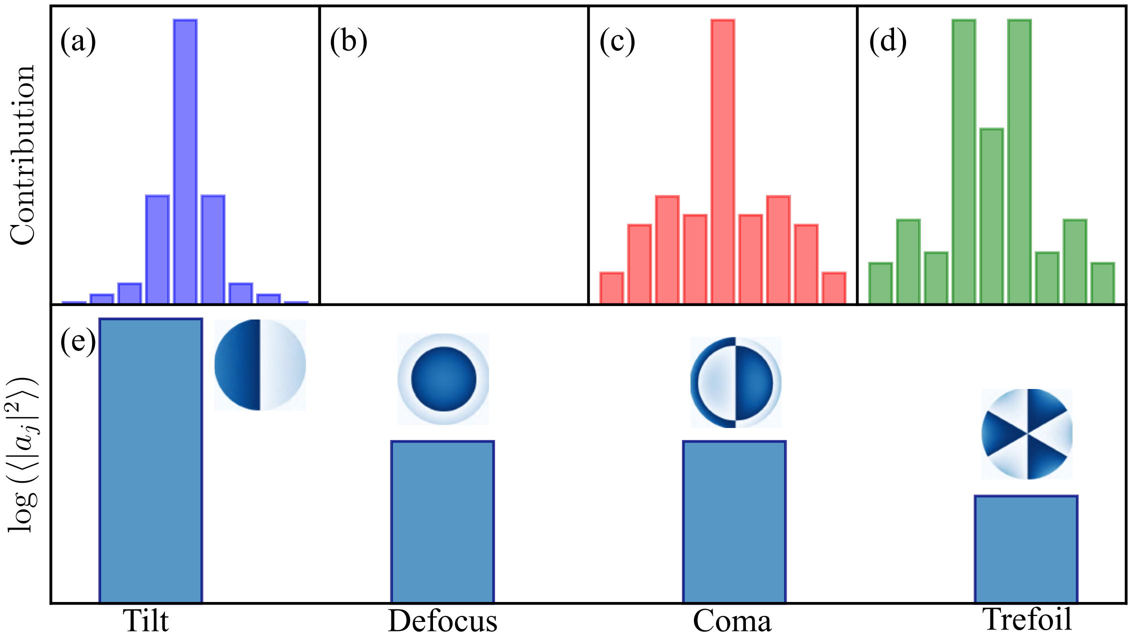

Figure 4.2: **Contribution to OAM**. (a) – (d) Modified OAM spectra of the atmosphere showing the contribution from the various Zernike aberrations normalized to the peak. The aberrations shown, from (a) to (d), are tilt, defocus, coma and trefoil. (e) Logarithmic plot of the variances of the coefficients a_j, with insets of the Zernike functions modulo 2π.

higher order terms diminishes rapidly so that for a fixed turbulence strength, the low order terms such as tip and tilt ($j = 2$ and $j = 3$) are an order of magnitude greater in coefficient value than the others (Fig. 4.2). With this in mind, we use this model to find an approximate expression for the structure function by choosing to truncate the sum to these two terms alone. Noting that $\Delta Z_3(\boldsymbol{\rho}) = Z_3(\boldsymbol{\rho})$ because of the odd sine function and that the covariance between the tip and tilt terms vanishes simplifies the sum to

$$\mathcal{D}(\boldsymbol{\rho}) \approx 4\left\langle |a_2|^2 \right\rangle \rho^2 \left(\cos\phi - 1\right)^2 + 4\left\langle |a_3|^2 \right\rangle \rho^2 \sin^2\phi. \tag{4.4}$$

This is further simplified since $\langle |a_2|^2 \rangle = \langle |a_3|^2 \rangle$ so

$$\mathcal{D}(\boldsymbol{\rho}) \approx 8\left\langle |a_2|^2 \right\rangle \rho^2 \left(1 - \cos\phi\right) = 16\left\langle |a_2|^2 \right\rangle \rho^2 \sin^2\left(\frac{\phi}{2}\right). \tag{4.5}$$

Evaluating $\langle |a_2|^2 \rangle$ yields a compact, analytic expression for the phase structure function, given by

$$\mathcal{D}(\boldsymbol{\rho}) \approx 7.21 \left(\frac{D}{r_0}\right)^{5/3} \left(\rho \sin\left(\frac{\phi}{2}\right)\right)^2, \tag{4.6}$$

where $D = 2\mathcal{R}$. Using this simplified version of our model, we have been able to recover to a high level of accuracy a well-known expression for this function in Kolmogorov turbulence[54]

$$\mathcal{D}(\boldsymbol{\rho}) = 6.88 \left(\frac{D}{r_0}\right)^{5/3} \left(\rho \sin\left(\frac{\phi}{2}\right)\right)^{5/3}. \tag{4.7}$$

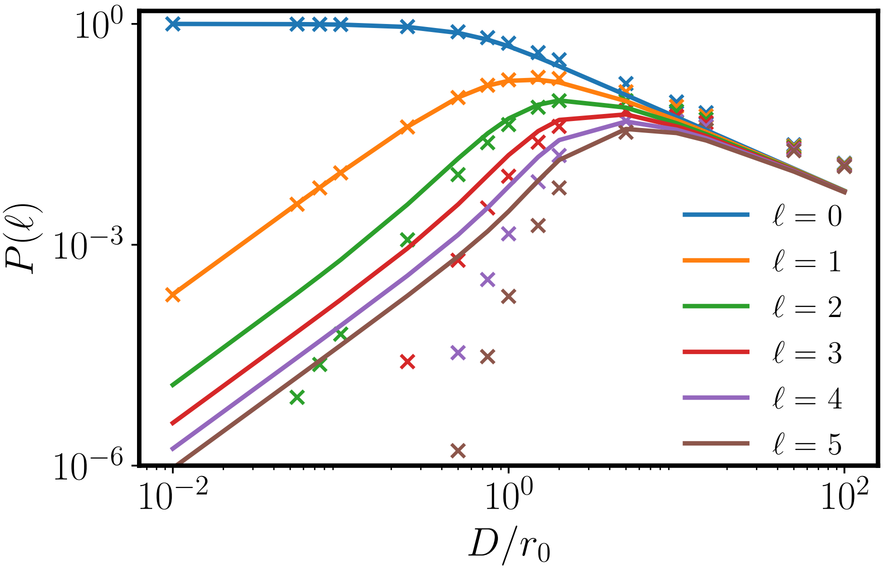

Figure 4.3: **Exact and approximate probabilities**. The probability of measuring $\ell = 0$ to 5 in the atmosphere is calculated from both the exact (Eq. 4.1) and approximate (Eq. 4.8) expressions for weak to strong turbulence. Solid lines and crosses refer to the exact and approximate cases, respectively.

We take this result for the structure function and substitute it into Eq. 4.1, which allows us to obtain a closed-form expression for $P(\ell)$, given by

$$P(\ell) \approx \frac{\beta^\ell \, {}_2F_2\left(\frac{1}{2}+\ell, 1+\ell; 2+\ell, 1+2\ell, -2\beta\right)}{2^\ell \Gamma\left(2+\ell\right)}, \tag{4.8}$$

where $\beta = 1.8025(D/r_0)^{5/3}$, $\Gamma(\cdot)$ is the gamma function and ${}_2F_2$ is the generalized hypergeometric function. Take the case $\ell = 0$ as an example: Eq. 4.8 reduces to

$$P(0) \approx \left(I_0(\beta) + I_1(\beta)\right) \exp\left(-\beta\right), \tag{4.9}$$

where $I_n(\cdot)$ is the modified Bessel function of the first kind. Fig. 4.3 illustrates the comparison between the exact (plotted as solid lines) and approximate (plotted as crosses) probabilities calculated using Eq. 4.1 and Eq. 4.8 respectively from weak to strong turbulence. The approximate probabilities are in excellent agreement for the $\ell = 0$, 1 cases. However, Eq. 4.8 underestimates $P(\ell)$ for weak turbulence in general.

The discrepancy between the refractive index variance and the truncated Zernike sum increases with increasing turbulence strength, so more a_j are needed. As the $\langle |a_j|^2 \rangle$ are an indication of 'how much' OAM is found in Θ, a more turbulent atmosphere is associated with a greater spread in OAM. Stronger turbulence should therefore result in the presence of higher OAM orders as more Z_j are required for an accurate decomposition.

Further, the spread of OAM in the atmosphere is symmetric about $\ell = 0$, since the substitution $\ell \mapsto -\ell$ in Eq. 4.1 leads to

$$P(-\ell) = \frac{1}{\pi} \int \mathrm{d}^2\boldsymbol{\rho} \, \cos\left(-\ell\phi\right) \exp\left(-\frac{1}{2}\mathcal{D}\left(\boldsymbol{\rho}\right)\right) = P(\ell) \tag{4.10}$$

courtesy of the even cosine function. Thus we do not expect a preference for clockwise or anticlockwise helicity in the atmosphere's OAM. We expect a single peak in the OAM spectrum of the atmosphere around $\ell = 0$, as $|\cos(\ell\phi)| \leq 1$, which means that

$$\left|\cos\left(\ell\phi\right)\exp\left(-\frac{1}{2}\mathcal{D}\left(\boldsymbol{\rho}\right)\right)\right| \leq \left|\exp\left(-\frac{1}{2}\mathcal{D}\left(\boldsymbol{\rho}\right)\right)\right| \tag{4.11}$$

over the unit disk, while $P(0)$ will have the greatest value. The existence of a second peak is not supported by this theory. There can be no $P(\ell)$ different from $P(-\ell)$ as they are equal. A second peak would indicate that the spectrum was not symmetric.

4.2 OAM exchange with the atmosphere

Here, we consider the interaction of the atmosphere with structured light.

4.2.1 Initial mode independence

We predict that the OAM of the atmosphere is independent of the structured light beam. To see this, consider an optical vortex (V) mode $W(r/R)\exp\left(im\phi\right)$, where $W(\cdot)$ is an aperture function, equal to 1 when the argument is less than 1 and 0 otherwise. The likelihood of measuring $\ell\hbar$ of momentum in the final field is, on average (see Appendix A.3),

$$P^V(\ell) = \frac{1}{\pi}\int \mathrm{d}^2\boldsymbol{\rho}\ \cos\left(\Delta\phi\right)\exp\left(-\frac{1}{2}\mathcal{D}\left(\boldsymbol{\rho}\right)\right) = P(\Delta), \tag{4.12}$$

where $\Delta = \ell - m$ and $P(\ell)$ is the probability of measuring $\Delta\hbar$ of OAM in the atmosphere (Eq. 4.1). That is, the OAM spectrum of the final field is identical to that of the atmosphere, except that it is symmetric about $\ell = m$ or $\Delta = 0$. This means that higher order OAM modes should not behave any differently than lower modes while propagating through turbulence of fixed strength. The atmosphere will produce the same change in OAM for any beam. It is thus better to think of Δ and not ℓ.

4.2.2 Beam types and size

The previous analysis has not mentioned the size of the field, but turbulence is invariably related to the scale at which we look. This is encoded by the Fried parameter r_0, which is the average distance over which points in the turbulent phase will be correlated.[85] This means that the turbulence strength is characterised by the ratio D/r_0, where $D = 2R$ is the diameter of the section of atmosphere we are studying (see Fig. 4.1). There are thus two ways to adjust the turbulence strength - rescale the 'window' through which you are looking or change r_0. If we consider D to be twice the beam waist, then larger beams propagate over a greater D, which is effectively stronger turbulence. As a result, the definition of beam size is

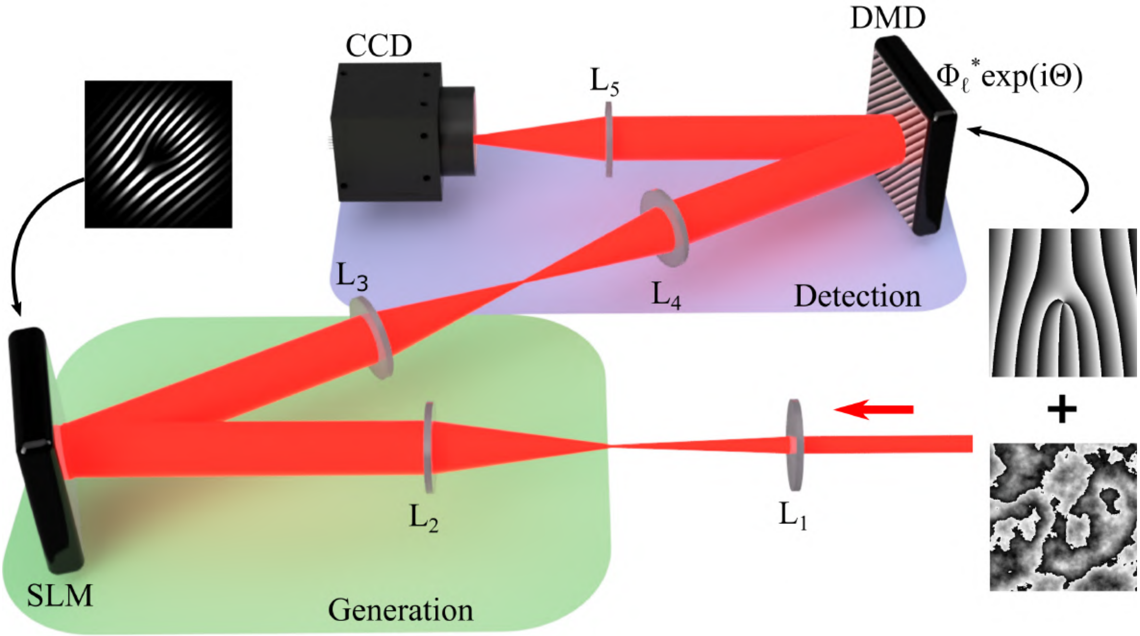

Figure 4.4: **Experimental set-up.** Lenses L_1 and L_2 expand a Gaussian beam onto a spatial light modulator (SLM), on which a hologram of a desired initial field is displayed. The field is subsequently imaged by lenses L_3 and L_4 onto a digital micromirror device (DMD), where binary holograms encoding the detection mode functions, $\Phi_\ell = \exp(i\ell\phi)$, together with the turbulence transmission function, $\exp(i\Theta)$, are displayed (see insets). The final beam is then mapped to the far field by lens L_5 where a charge-coupled device (CCD) records an axis intensity corresponding to the modal overlap.

very important. Take Laguerre-Gaussian modes as an illustrative example. These modes, ignoring constants, have the form (repeated here for convenience)

$$LG_0^m(\mathbf{r}) = \left(\frac{\sqrt{2}r}{w_0}\right)^{|m|} \exp\left(-\frac{r^2}{w_0^2}\right) \exp\left(im\phi\right),$$

where the radial index is set to 0 and w_0 is the waist of the embedded Gaussian. The second moment radius is $\overline{r^2} = w_0\sqrt{1+|m|}$, which gets larger for higher order modes. One may, mistakenly, say that higher order modes (with fixed w_0) are less robust. But, from the perspective of the atmosphere, higher order modes are larger and 'see more' of the atmosphere, which is equivalent to passing through stronger turbulence. However, if the waist of the Gaussian factor is set to $w_0 \to w_0/\sqrt{1+|\ell|}$, then all modes have the same second moment radius and should behave similarly. The only important factor is the turbulence strength, which is the size of the beam, all else kept equal.

4.3 Experimental confirmation

In this section, we provide experimental confirmation of our theoretical predictions. Our experiment is shown in Fig. 4.4 and comprises two parts: a section in

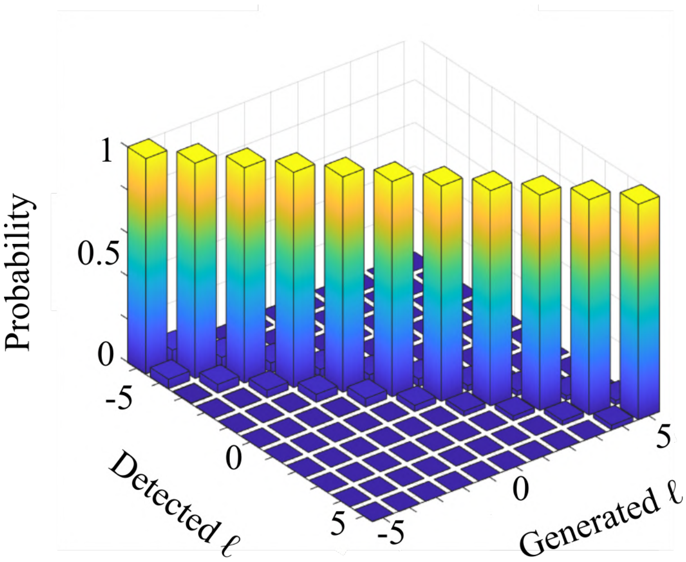

Figure 4.5: The accuracy of the experimental setup is verified using a crosstalk matrix for 11 modes where $\ell \in [-5, 5]$. We see that the matrix is almost perfectly diagonal, indicating that any spread in a beam's OAM spectrum is attributable to turbulence alone.

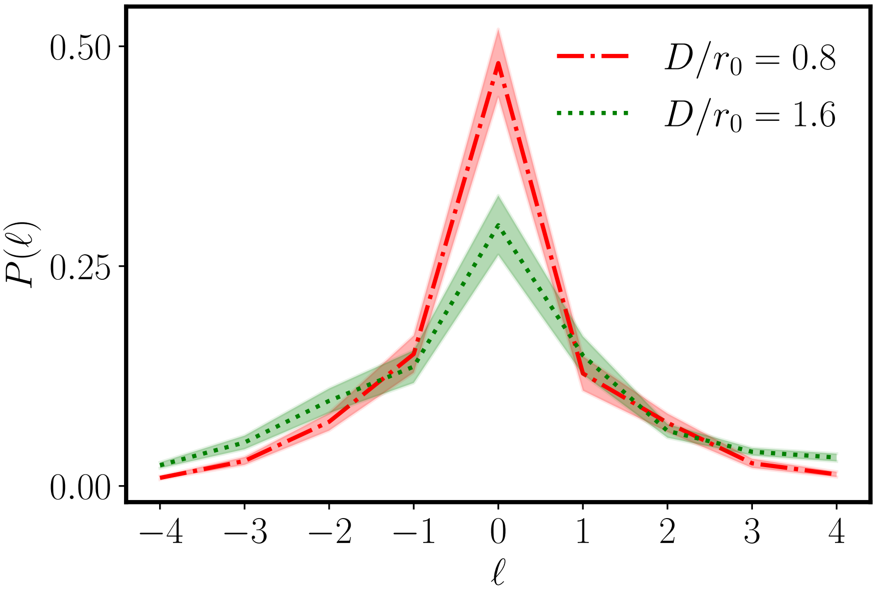

Figure 4.6: **Measured OAM of the atmosphere.** Experimental OAM spectrum of the atmosphere for turbulence strengths $D/r_0 = 0.8$ and 1.6. The shaded regions show the variance of $P(\ell)$ around the respective mean values (dashdot and dotted lines). The shaded bands correspond to the measurement uncertainties.

which the modes were generated using a Holoeye Pluto phase-only spatial light modulator (SLM), and a second section, where turbulence was added to the mode and the OAM content of the final field was detected using a digital micromirror device (DMD), lens and CCD camera. Lenses L_1 and L_2 expanded the laser beam onto the SLM, on which a hologram was displayed. This generated the initial field. Lenses L_3 and L_4 imaged the field onto the DMD, on which a hologram of the appropriate match filter and turbulent phase screen was displayed. L_5 acted as a Fourier lens, ensuring that the far field intensity was observed on the CCD camera where the $P(\ell)$ is proportional to the on axis intensity.[80] The holograms that were encoded on the SLM and DMD were computed following methods from Refs.[75] and,[78] respectively. Although the turbulence could be created directly from the Zernike aberrations,[87,92,93] we elected to simulate turbulence by generating phase screens using the sub-harmonic random matrix transform method,[91] which has no direct link to OAM nor the Zernike aberrations. This method guarantees that the screens exhibit the correct $-11/3$ power law characteristic of Kolmogorov power spectrum,[69] while ensuring that our predictions are not self-satisfying.

In order to validate the random phase screens we used the Strehl ratio (SR) (explained in Chapter 2),[34] as it provides a direct relationship between measured intensities and turbulence strength. It is the ratio of the average on axis intensity of the beam with, $\langle I(\mathbf{0})\rangle$, and without, $I_0(\mathbf{0})$, turbulence. A crosstalk matrix, seen in Fig. 4.5, for 11 modes ($\ell = -5$ to 5) was obtained for zero turbulence. Such a matrix ensures that any instance of $P(\Delta \neq 0) \neq 0$ is attributable to turbulence alone and not experimental error.

A Gaussian beam whose width was large compared to the DMD screen was used to experimentally measure the OAM of the atmosphere, as this beam approximates the constant intensity used in the derivation of Eq. 4.1. Fig. 4.6 shows the experimentally measured OAM spectrum of the atmosphere for $D/r_0 = 0.8$ and $D/r_0 = 1.6$. The spectra are peaked at $\ell = 0$ as expected (see Eq. 4.11) and are symmetric, implying a lack of preference for left or right helicitiy ($\pm\ell$) in the atmosphere. The statistical variance in the $P(\ell)$ is visualized as shaded bands around the data.

To quantify the interaction between the atmosphere and structured light fields, two families of beams were investigated: vortex LG beams defined in Eq. 4.2.2 and pure vortex (PV) modes defined, ignoring constants, as

$$\mathrm{PV}_m(\mathbf{r}) = \exp\left(-\frac{(r - r_V)^2}{w_0^2}\right)\exp\left(im\phi\right),$$

where r_V is the radial position of the ring. The experiment confirmed the symmetry of the OAM spectra of the beams, the presence of a single peak in those spectra and the independence of initial TC. Fig. 4.7 shows the the dependence of an LG vortex mode's behaviour in turbulence on its size. The crosstalk matrices in Fig. 4.7(a) and Fig. 4.7(b) for $D/r_0 = 1.6$ and different beam sizes show how the seemingly unresilient behaviour of higher order modes in turbulence is in fact a result of their increased size. This effect is magnified in Fig. 4.7(c), where the probability $P(\ell)$ of measuring the same charge as the generated beam (normalized by the Gaussian case $P(0)$) is measured for weak and strong turbulence cases. Beams whose second moment radii are equal perform similarly, independent of the initial OAM charge. In contrast, beams whose size increase with ℓ exhibit the well-known mode-dependent degradation as a result of turbulence. The aperture D was taken as twice the second moment radius. PV beams, shown in Fig. 4.8, were investigated as all modes are the same size. Measurements for modes with initial charges ($m = 1, 8, 15$) in weak turbulence are in excellent agreement with the theory: confirming the independence on initial charge and showing the symmetry of the spectrum and the peak at $\ell = 0$, as predicted.

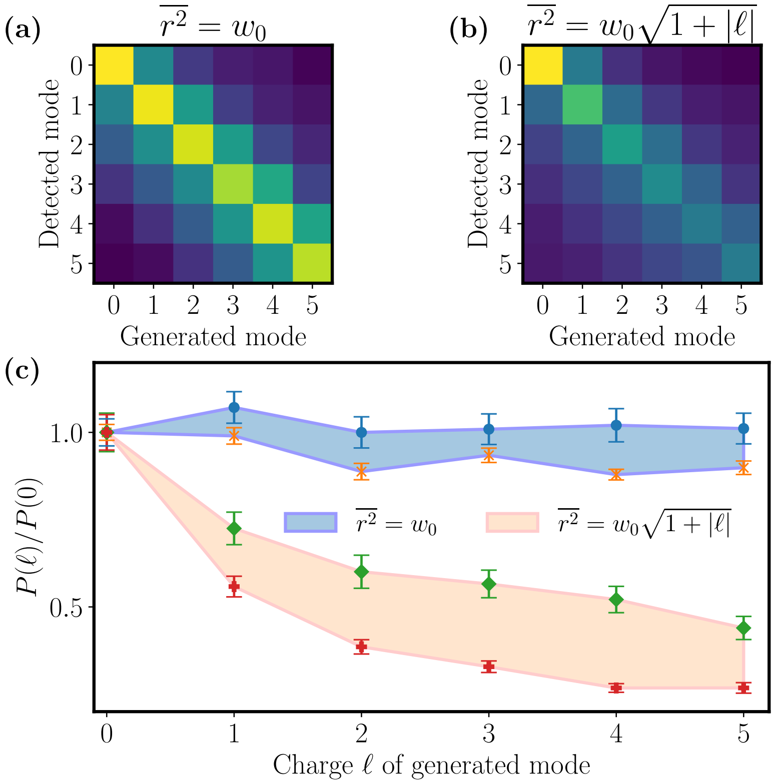

Figure 4.7: **Effects of beam resizing on LG modes.** (a) and (b) are crosstalk matrices for LG modes in medium turbulence whose second moment radii are equal to w_0 and $w_0\sqrt{1+|\ell|}$ respectively, where w_0 is the waist of the Gaussian ($\ell = 0$) case. (c) The quantity $P(\ell)$ is the likelihood of measuring the same charge as the initial beam. The probabilities are normalised to the Gaussian case $P(0)$ for comparison. The upper and lower limits for $\overline{r^2} = w_0$ and $\overline{r^2} = w_0\sqrt{1+|\ell|}$ correspond to $D/r_0 = 0.8$ and $D/r_0 = 2.4$, respectively.

4.4 One or two peaks?

Sorelli *et al.*[94] investigated the extended medium (multiple phase screens) and observed the mysterious appearance of a 'double peak' in the OAM spectrum of an LG mode after turbulence. Initial thoughts suggested that this was a feature which appears only in the strong regime and will not be observed when turbulence is weak and modelled with a single phase screen, like the results presented above. This would suggest that modes with equal but opposite OAM

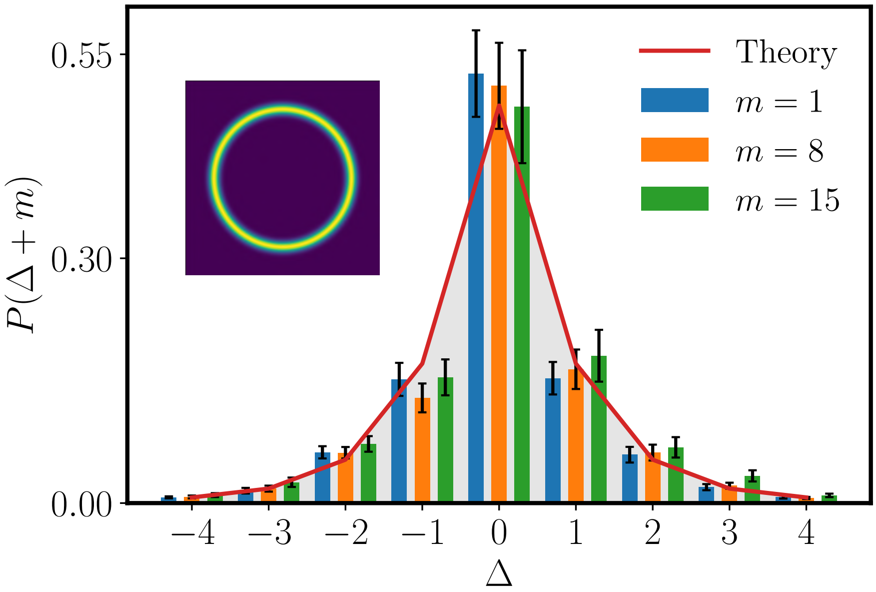

Figure 4.8: **Modal independence and symmetry.** The probability of measuring $\ell = \Delta + m$ for PV modes with initial charges $m = 1$, 8 and 15 in weak turbulence ($D/r_0 = 0.8$). The solid line corresponds to theoretical values and the inset shows a simulated PV intensity profile

.

values couple more strongly into each other than neighbouring modes. From the perspective of the atmosphere, this does not make sense. If the affect of the atmosphere on a beam's OAM spectrum is symmetric on average, why should the inclusion of more phase screens introduce an asymmetry in the momentum exchange? These seemingly contradictory results were resolved and synthesised by noting the basis in which the measurements were made: this research used the $\exp(i\ell\phi)$ OAM basis states to measure the total OAM spectrum of the field, whereas Ref.[94] used the LG basis but did not examine the p indices. When using the OAM basis, the double peak 'disappears' and one is left with a symmetric OAM spectrum, as expected. However, the LG $p = 0$ basis leaves out information contained in the p-modes. The peak at the opposite OAM charge $-m$ is explained by examining the amplitude structure of the LG modes – modes with the $\pm\ell$ have identical radial functions. Strong turbulence significantly disturbs the phase of a mode which allows the radial contribution to the inner product to become more pronounced. This effect is illustrated in Fig. 4.9 by decomposing a set of LG modes into three different basis: the pure OAM $\exp(i\ell\phi)$ basis, the LG basis and a pseudo-basis consisting of the amplitudes of the LG modes with all phase information discarded. The bar plots correspond to a mode with $m = 5$ initially and this is indicated on the crosstalk matrices by a red line. The two lines in the bar plots correspond to $\pm m$.

4.5 Discussion and Conclusion

We can clarify the current disagreement in the community regarding the robustness or lack thereof of higher order modes. Studies that supported modal inde-

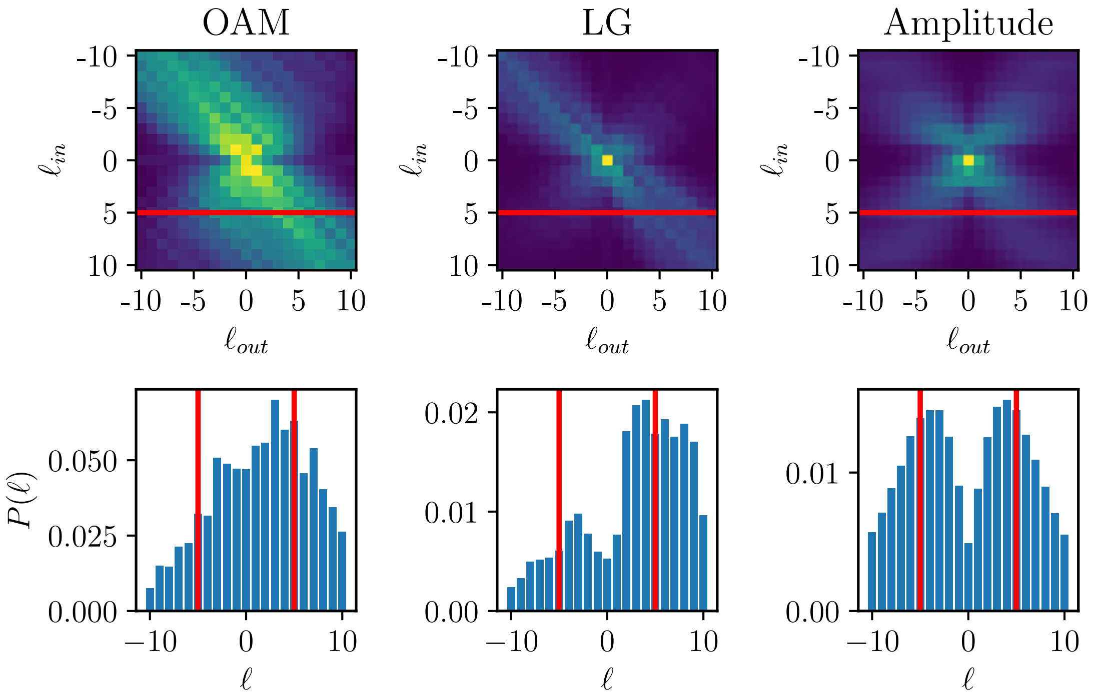

Figure 4.9: The basis used for measuring the spectrum of LG modes after turbulence determines the appearance of the 'double peak'. The OAM basis modes are $\exp(i\ell\phi)$ and measure the entire OAM spectrum of the mode. In such a picture, the spectrum is symmetric and it is equally likely that the atmosphere will give or take momentum from the beam. However, the LG $p = 0$ basis does not contain the OAM found in the other p indices. The second peak is explained by the radial overlap between the $\pm\ell$ modes. This effect is amplified when we decompose the final field into a basis consisting of $\left|\mathrm{LG}^{\ell}_{p=0}\right|$, where we only take the amplitude of the LG functions. Experimental crosstalk matrices show $\ell \in [-10, 10]$ for 60 iterations of turbulence where $\sigma_R^2 = 1.383$. The slice corresponds to $m = 5$.

pendence[54–56] investigated optical vortex beams and imaged them between the transmitting and receiving planes. These beams lack a mode-dependent size parameter and posses the same second moment radius. In contrast, those studies that reported modal dependence did not resize higher order modes, resulting in larger second moment radii. Propagated vortex Gaussian modes[58] will have intensity profiles which depend on the initial charge in a similar way to the more obvious cases of LG[59] and IG[33] modes. According to our model, this is all resolved by understanding that turbulence is dependent on a beam's size and not its OAM. When there is a link between the two, e.g. $\overline{r^2} = w_0\sqrt{1+|\ell|}$, one can mistakenly conclude that higher order modes are less robust. However, the asymmetry of the OAM spectra[58] seems to be an anomalous result.

The OAM content of the atmosphere is non-zero, even though it possesses a symmetric spectrum which results in a 0 mean charge (refer to Fig. 4.6). A question may be posed: if the aberrations possess symmetric OAM profiles, which imply a total OAM of 0, how can there be non-zero OAM spreading (modal crosstalk)? This is reconciled by realising that the symmetry of TCs in the aberrations result in a symmetric OAM spectrum. On average, the OAM of the beam is zero. However, there is an equal, non-trivial likelihood that a photon carrying $(\pm m + \Delta)\hbar = \ell\hbar$ is present in the final field. Since the beam has gained these photons, the likelihood of measuring photons carrying the initial TC must have decreased. Note that in deriving Eq. 4.12, a rotationally symmetric beam profile is assumed. Although this seems to exclude other families such as the Hermite-Gaussian modes, the same analysis can be applied to these modes by expanding them into a rotationally symmetric basis.

Interestingly, there is a distinction between a Zernike term's contribution to turbulence and its contribution to OAM. This behaviour is reflected in $\mathcal{D}(\boldsymbol{\rho})$ (see Eq. 4.2). The $\langle |a_j|^2 \rangle$ are considerably smaller for higher order terms. Thus, turbulence and the OAM spectrum are mostly described by lower order terms. However, Fig. 4.2 shows the conspicuous zero contribution of the defocus term to OAM, in spite of the relative size of its coefficient. To understand this, consider a beam in a superposition of $\ell = \pm 1$. The phase of such a beam is precisely the inset of the tilt term. Defocus, however, contributes an azimuthally symmetric phase which affects the curvature of the wavefront, but not its vorticity. This is mathematically captured in the result $\Delta Z_4 = 0$, and so defocus results in a null contribution to the phase structure function.

One may wonder where the OAM of the atmosphere might come from? The notion of the atmosphere possessing angular momentum can be linked to fluid dynamics. Turbulence is characterised by kinetic energy transfer along different length scales. This cascade of energy is facilitated by eddies - regions of non-zero vorticity.[95] These regions of circular vortex rings are ultimately responsible for the Kolmogorov -11/3 power law.[96] These fluid vortices could manifest themselves as phase vortices through the fluctuations in the refractive index of the atmosphere and will be detected as OAM in structured light fields. We hope that this inspires future research linking these seemingly disparate fields.

Chapter 5

Eigenmodes of turbulence

Here, we present a class of modes whose amplitude and phase remain invariant as they propagate through a turbulent channel. These are the so-called eigenmodes of the channel. Unlike other spatial modes, no corrective procedures are necessary and unwanted effects like modal crosstalk are removed. We demonstrate this invariance through a thick medium modelled using multiple turbulent phase screens along the propagation path. A full theoretical model is presented with extensive simuations, and confirmation is provided by a laboratory based experiment. This technique can be easily extended to arbitrary noisy channels whose characteristics are known.

5.1 Solving the eigenvalue problem

5.1.1 Representing the channel in the pixel basis

The goal of this section is to find some linear operator $\mathcal{T}$ which describes a turbulent channel. Once this operator is found, the process of diagonalising it reduces to any other eigenvalue problem. These basis states which diagonalise the turbulent channel are precisely the eigenmodes of the channel. We could take the stochastic Helmholtz equation (see Eq. 3.19) and write

$$\mathrm{U}_f = \mathcal{T}\mathrm{U}_i \tag{5.1}$$

where

$$\mathcal{T} = \int \mathrm{d}^3\mathbf{R}'\ 2\delta n(\mathbf{R}')k^2 \frac{\exp\left(ik\|\mathbf{R}' - \mathbf{R}\|\right)}{4\pi\|\mathbf{R}' - \mathbf{R}\|}. \tag{5.2}$$

The eigenmodes must then satisfy the condition $\mathrm{U}_f = \gamma\mathrm{U}_i$ where γ is the eigenvalue. Without the explicit form of δn we cannot find solutions to this eigenvalue equation. This problem lends itself to a numerical treatment and so we work in the strong scintillation regime ($\sigma_R^2 > 1$). The channel of length L is modelled using the split-step method described in Section 3.4 with random phase screens placed at equal distances along the propagation path. If we concentrate on a single segment of this path, we see that the beam picks up a turbulent phase Θ and then propagates a distance z. Mathematically this transformation is described by the equation

$$\mathcal{T}\mathrm{U}_i \equiv \int \mathrm{d}^2\mathbf{r}\ g(\mathbf{r}, \mathbf{r}'; z) \exp(i\Theta(\mathbf{r}))\mathrm{U}_i(\mathbf{r}, 0), \tag{5.3}$$

where

$$g(\mathbf{r},\mathbf{r}';z) = \frac{1}{i\lambda z}\exp\left(\frac{i\pi}{\lambda z}\|\mathbf{r}-\mathbf{r}'\|^2\right) \tag{5.4}$$

is the paraxial free space Green's function and $\mathbf{r}$, $\mathbf{r}'$ are the two-dimensional coordinates of the initial and final planes, respectively. The position (pixel) basis is used for a matrix representation of the channel operator by discretising the initial and final planes into grids of $N \times N$ points. The coordinates are labelled $\mathbf{r} = (x_\alpha, y_\beta)$ and $\mathbf{r}' = (x_\mu, y_\nu)$ so that the integral is approximated by the sum

$$\mathrm{U}^f_{\mu\nu} = \sum_{\alpha,\beta} \mathcal{T}_{\mu\nu\alpha\beta}\mathrm{U}_{\alpha\beta} = \mathcal{T}_{\mu\nu\alpha\beta}\mathrm{U}^i_{\alpha\beta} \tag{5.5}$$

where

$$\mathcal{T}_{\mu\nu\alpha\beta} = \frac{\Delta x \Delta y}{i\lambda z}\exp\left(\frac{i\pi}{\lambda z}\left(x_\mu - x_\alpha\right)^2 + \frac{i\pi}{\lambda z}\left(y_\nu - y_\beta\right)^2 + i\Theta(x_\alpha, y_\beta)\right) \tag{5.6}$$

and repeated lower indices are implicitly summed over. An eigenmode U solves the tensor equation

$$\gamma \mathrm{U}_{\mu\nu} = \mathcal{T}_{\mu\nu\alpha\beta}\mathrm{U}_{\alpha\beta}. \tag{5.7}$$

This four dimensional tensor equation can be systematically reduced to a regular matrix-vector equation by introducing a bijective mapping ξ that acts on the indices (α, β) and (μ, ν) and "counts" them, first along the columns and then along the rows according to

$$\begin{aligned} \xi(1,1) &= 1, \\ &\vdots \\ \xi(1,N) &= N, \\ \xi(2,1) &= N+1, \\ &\vdots \\ \xi(N,N) &= N^2. \end{aligned} \tag{5.8}$$

This can be visualised as "unfolding" the two dimensional matrix $\mathrm{U}_{\alpha\beta}$ into a long column vector where each row is stacked on top of the next until all N^2 elements are mapped and leads to the usual eigenvalue problem

$$\gamma \mathrm{U}_i = \mathcal{T}_{ij}\mathrm{U}_j \tag{5.9}$$

where $\xi(\alpha,\beta) = j$ and $\xi(\mu,\nu) = i$.

5.1.2 Fresnel scaling

The channel parameters, like path length, are highly restricted in the laboratory setting. This presents an apparent difficulty to experimentally verifying the eigenmodes. However, a scaling procedure exists called Fresnel scaling[97] which allows us to verify real-world channels in the laboratory setting. This procedure is presented below.

The Fresnel integral for the full (real-world) channel of length L is

$$\mathrm{U}_f(\mathbf{r}, L) = \frac{\exp(ikL)}{i\lambda L} \int \mathrm{d}^2\mathbf{r}' \, \mathrm{U}_i(\mathbf{r}') \exp\left(\frac{i\pi}{\lambda L} \|\mathbf{r} - \mathbf{r}'\|^2\right). \tag{5.10}$$

We then apply the following scaling parameters: $\mathbf{r}_{\text{lab}} = \alpha_x \mathbf{r}$, $\mathbf{r}'_{\text{lab}} = \alpha_{r'} \mathbf{r}'$ and $L' = \alpha_z L$, where $\mathbf{r}_{\text{lab}}$ and $\mathbf{r}'_{\text{lab}}$ are the coordinates used in the experiment. The diffraction integral becomes

$$\begin{aligned} \mathrm{U}_f\left(\frac{\mathbf{r}_{\text{lab}}}{\alpha_r}\right) = \frac{\exp\left(ikL'/\alpha_z\right)}{i\alpha_{r'}\lambda L'} \int \mathrm{d}^2\mathbf{r}'_{\text{lab}} \, \mathrm{U}_i\left(\frac{\mathbf{r}'_{\text{lab}}}{\alpha_{r'}}\right) \times \\ \times \exp\left(\frac{i\pi\alpha_z}{\lambda L'} \left\| \frac{\mathbf{r}_{\text{lab}}}{\alpha_r} - \frac{\mathbf{r}'_{\text{lab}}}{\alpha_{r'}} \right\|^2\right). \end{aligned} \tag{5.11}$$

To keep the diffraction equivalent with these scaled coordinates we require the Fresnel number

$$F = \frac{\pi D_i D_f}{4\lambda L} \tag{5.12}$$

to be the same in both the full and scaled-down cases, where D_i and D_f are the aperture diameters in the initial and final planes, respectively. This sets $\alpha_r \alpha_{r'} = \alpha_z$ and the diffraction integral becomes

$$\begin{aligned} \frac{\exp\left(ikL'\left(1 - \frac{1}{\alpha_z}\right)\right)}{\alpha_r} \mathrm{U}_f\left(\frac{\mathbf{r}_{\text{lab}}}{\alpha_r}\right) = \exp\left(-\frac{i\pi r_{\text{lab}}^2}{\lambda f_r}\right) \frac{\exp\left(ikL'\right)}{i\lambda L'} \times \\ \times \int \mathrm{d}^2\mathbf{r}'_{\text{lab}} \, \mathrm{U}_i\left(\frac{\mathbf{r}'_{\text{lab}}}{\alpha_{r'}}\right) \exp\left(-\frac{\pi (r'_{\text{lab}})^2}{\lambda f_{r'}}\right) \exp\left(\frac{i\pi}{\lambda L'} \|\mathbf{r}_{\text{lab}} - \mathbf{r}'_{\text{lab}}\|\right), \end{aligned} \tag{5.13}$$

where

$$f_r = \frac{L'}{1 - \alpha_{r'}/\alpha_r}, \tag{5.14}$$

$$f_{r'} = \frac{L'}{1 - \alpha_r/\alpha_{r'}}. \tag{5.15}$$

Setting $\alpha_r = \alpha_{r'}$ means that the final and initial planes have the same size in the laboratory setting and $f_{r,r'} \to \infty$ and the final Fresnel integral, ignoring constant phase factors which arise due to scaling, becomes

$$\mathrm{U}_f\left(\frac{\mathbf{r}_{\text{lab}}}{\alpha_r}\right) = \frac{\alpha_r \exp(ikL')}{i\lambda L'} \int \mathrm{d}^2\mathbf{r}'_{\text{lab}} \, \mathrm{U}_i\left(\frac{\mathbf{r}'_{\text{lab}}}{\alpha_{r'}}\right) \exp\left(\frac{i\pi}{\lambda L'} \|\mathbf{r}_{\text{lab}} - \mathbf{r}'_{\text{lab}}\|\right). \tag{5.16}$$

5.2 Numerical solutions

5.2.1 Vacuum propagation

To illustrate the action of the operator $\mathcal{T}$, we consider the case of vacuum propagation (zero turbulence), shown in Fig. 5.1. Propagation was simulated over 2 metres for an LG beam with radial index set to zero and an azimuthal index of

$\ell = 1$ (Fig. 5.1(a)) . The beam was simulated on a grid of 60×60 pixels where each pixel had a physical side length of 50 μm in Fig. 5.1(b) and Fig. 5.1(c), whereas the pixel size is increased in the propagated plane in Fig. 5.1(e) and Fig. 5.1(f) to twice that of the initial plane. This sizing causes the beam in the Rayleigh plane to appear unchanged. Propagation is achieved purely by matrix multiplication.

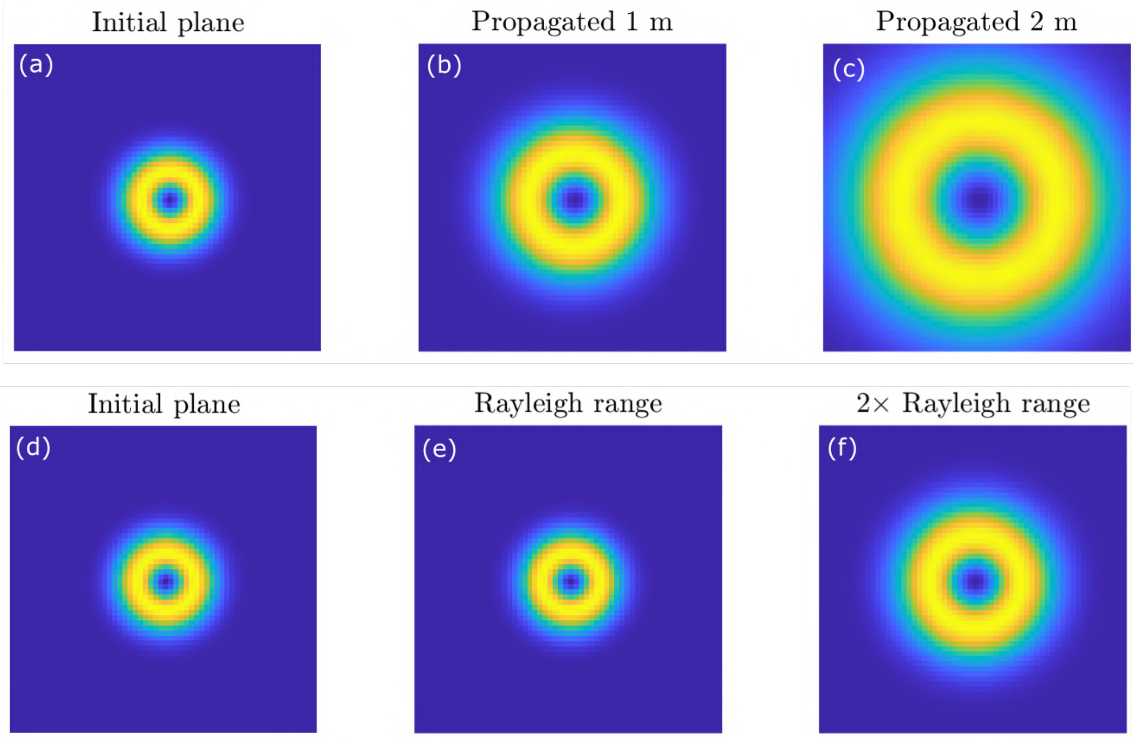

Figure 5.1: An $\mathrm{LG}_{p=0}^{\ell=1}$ beam ((a) and (d)) is propagated over 2 metres using the propagation operator $\mathcal{T}$. (b) and (c) show the beam at 1 and 2 metres, respectively, where the pixels in the initial and propagated planes have equal sizes. The pixels in (e) and (f) are sized such that the beam appears to have the same size in the initial and Rayleigh planes.

5.2.2 Sampling constraints and unitarity

The use of the Fresnel diffraction integral is valid so long as the condition[88]

$$\delta_2 = \frac{\lambda L}{N\delta_1} \tag{5.17}$$

is satisfied. δ_1 and δ_2 are the pixel side lengths in the initial and final planes, respectively, and N is the number of sampling points along one dimension. To avoid numerical artefacts like aliasing, we must also satisfy the condition

$$\frac{N\delta_1^2}{\lambda} \leq L. \tag{5.18}$$

Interestingly, there is only a *minimum* propagation distance L over which the discrete (sampled) Fresnel integral is valid. However, if we combine the two conditions in Eq. 5.17 and Eq. 5.18, then the operator $\mathcal{T}$ can be used to simulate the propagation of a beam over an arbitrarily long distance. This is in contrast to the angular spectrum method which sets a maximum distance for propagation.[88] We illustrate this in Fig. 5.2 by propagating a Bessel-Gaussian beam carrying OAM with a waist parameter of $w_0 = 1$ mm and $k_r = 9 \times 10^3$ m^{-1} over a distance of 4.963 metres using only 60×60 pixels. The distance was chosen as it corresponds to the Rayleigh length of a Gaussian beam with the same waist parameter w_0. The same beam was propagated using the angular spectrum method, but the grid had to be resized to 256×256 pixels to avoid numerical artefacts. The beams were then resized to 60×60 grids for comparison. Fig. 5.2 confirms that the discrete Fresnel operator acts on beams correctly as the two rows are indiscernible from each other.

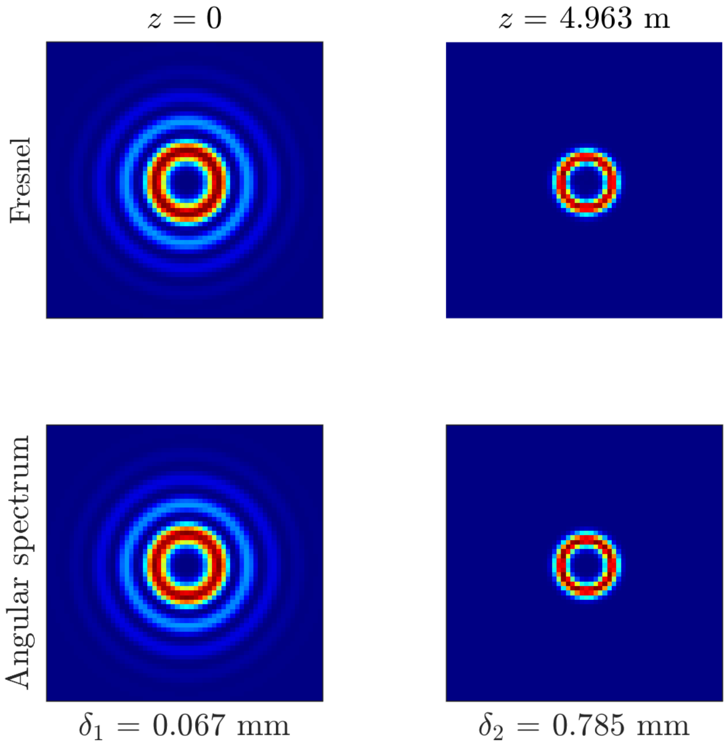

Figure 5.2: A Bessel-Gaussian beam with $w_0 = 1$ mm is propagated over 4.963 m using the vacuum Fresnel propagation operator (top row) sampled over 60×60 pixels and obeying all sampling conditions. For comparison, the same beam is propagated using the angular spectrum method (bottom row) on a grid of 256×256 pixels. The grid was then resized to 60×60 pixels for comparison. The two methods are certainly in agreement with each other, given the strong similarity between the top and bottom rows.

Further, using the correct scaling of pixels in the propagated plane preserves the unitary of the Fresnel diffraction integral as it ensures that all the light emitted in the initial plane is captured over the propagation. However, Fig. 5.3(a) clearly shows that using the convention $\delta_1 = \delta_2$ breaks the unitarity of $\mathcal{T}$ as the propagated grid is not large enough to capture all the emitted light. This is evident if we consider the matrix product $\mathcal{T}\mathcal{T}^\dagger$, which should be the identity matrix if $\mathcal{T}$ is unitary. This is in contrast to the preservation of unitarity in Fig. 5.3(b) when

$\delta_2 = \lambda L/N\delta_1$. Fig. 5.3(c) and Fig. 5.3(d) show eigenmodes obtained for different scaling regimes. When the pixels are scaled such that $\delta_1 = \delta_2$, we obtain the well-known LG beams (or superpositions of them) which are indeed solutions for vacuum propagation, as seen in Fig. 5.3(c). However, Fig. 5.3(d) shows that setting $\delta_2 = \lambda L/N\delta_1$ may preserve the unitarity of the operator but results in sparse, speckle-like and unphysical eigenmodes.

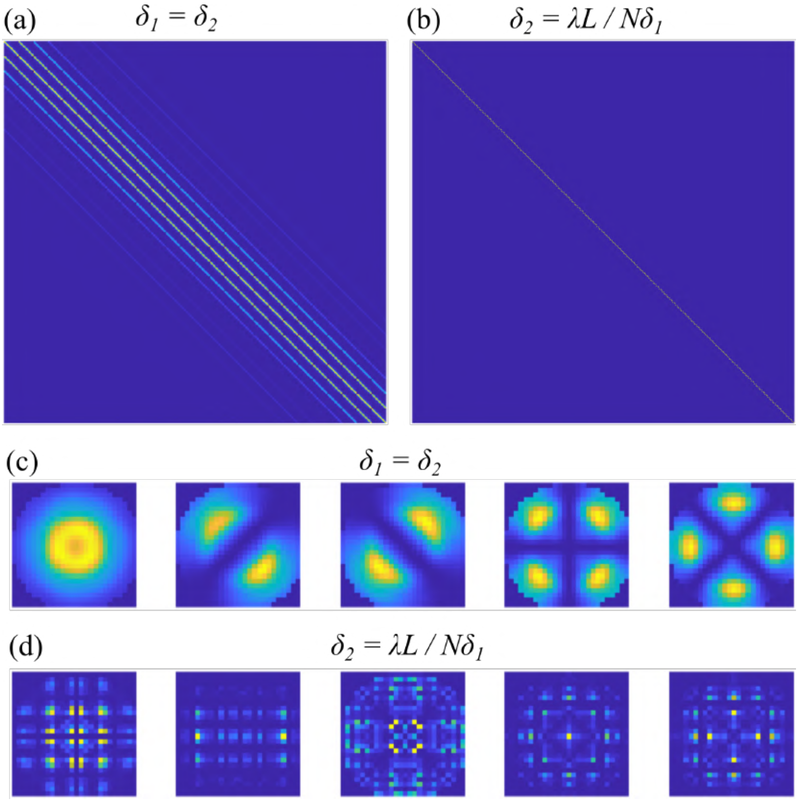

Figure 5.3: The unitarity of the operator $\mathcal{T}$ is destroyed when violating Eq. 5.17, see (a), but is preserved otherwise – see (b). The matrices show the product $\mathcal{T}\mathcal{T}^\dagger$ which should be the identity matrix if $\mathcal{T}$ is unitary. The matrix product in (b) is clearly diagonal which reflects the correct scaling, in contrast to the product in (a). Eigenmodes for free space vacuum propagation are shown in (c) and (d). In (c), the pixels are kept the same size and permit solutions resembling well-known superpositions of LG beams. However, when the correct scaling of Eq. 5.17 is employed, the eigenmodes become sparse speckle-like patterns.

5.2.3 Reintroducing turbulence

To demonstrate the process of diagonalising a turbulent operator, we consider the following case. The initial and final planes were divided into 60 × 60 pixels, each $0.0667 \times 0.0667\ \text{mm}^2$ in size. The length (propagation distance) of a segment was two metres and the turbulence strength was $D/r_0 = 1.5$. For such parameters, the minimum propagation distance over which the discrete Fresnel operator is valid is

$$z_{\text{min}} = 0.42\ \text{m} < 2\ \text{m}, \tag{5.19}$$

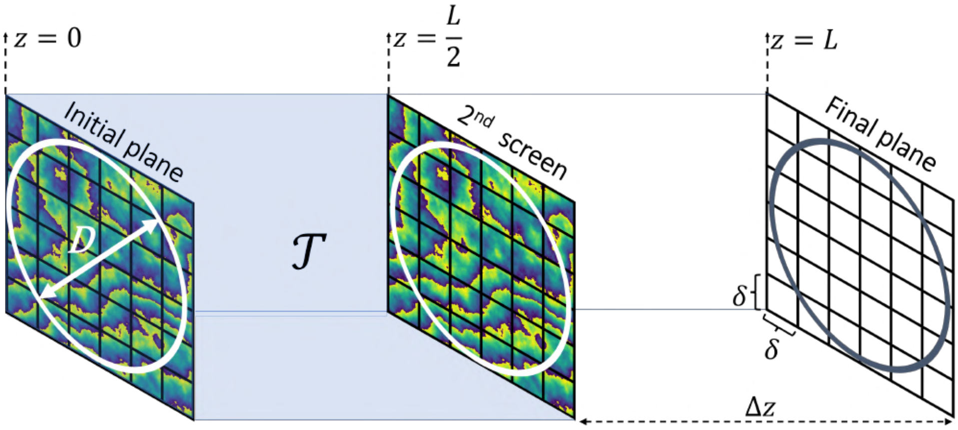

Figure 5.4: We consider a channel of length $L = 4$ m consisting of two screens, placed at $z = 0$ and $z = 2$. The planes are discretised into grids of 60×60 pixels (the figure shows 6×6 pixels for illustration purposes) of area $\delta \times \delta$, and the segments can be conceptually divided into repeated sections of a turbulent phase followed by vacuum propagation of $\Delta z = 2$ m. The operator $\mathcal{T}$ represents the first slab only – highlighted in blue. The overlaid circles illustrate the aperture D used to characterise the strength D/r_0.

using Eq. 5.18. The required pixel size in the final plane, according to Eq. 5.17, should be

$$\delta_2 = 0.317 \text{ mm} \approx 4.75\,\delta_1. \tag{5.20}$$

We set $\delta_2 = \delta_1$ to avoid the speckle-effect in the turbulent eigenmodes. Using these parameters, we compute the crosstalk matrices of Fig. 5.5, both before (left column) and after (right column) the channel. The matrices presented in (a) and (b) correspond to the channel's eigenmodes and LG beams with $\ell \in [0, 4]$, respectively. The crosstalk for the LG beams is significant but effectively non-existent between the eigenmodes.

5.3 Experimental verification

The experiment, shown in Fig.5.6, is conceptually divided into three parts. In the generation stage, a laser beam was expanded and collimated by lenses L_1 and L_2 onto an SLM which generated the desired initial field. This field then entered the turbulent section of the setup where it passed through a random phase screen and propagated one metre before being incident on another phase screen and propagating a metre further. The phase screens were generated using the sub-harmonic random matrix transform method (see Section 3.3.2) with Fried parameters determined by the split-step method (Section 3.4). This perturbed and aberrated field was decomposed into a desired basis in the detection section. The beam was then multiplied by the complex conjugate of a basis function which was displayed on another SLM before passing through a Fourier lens L_3. The on-axis intensity was measured on a camera (CCD).

We studied a channel of $L = 200$ m, $\lambda = 633$ nm and a Rytov variance of $\sigma_R^2 = 1.383 > 1$. The Fried parameter r_0 of the entire channel was 7 mm. According to the split-step method, we required two screens each with Fried parameter $r_{0,s} =$

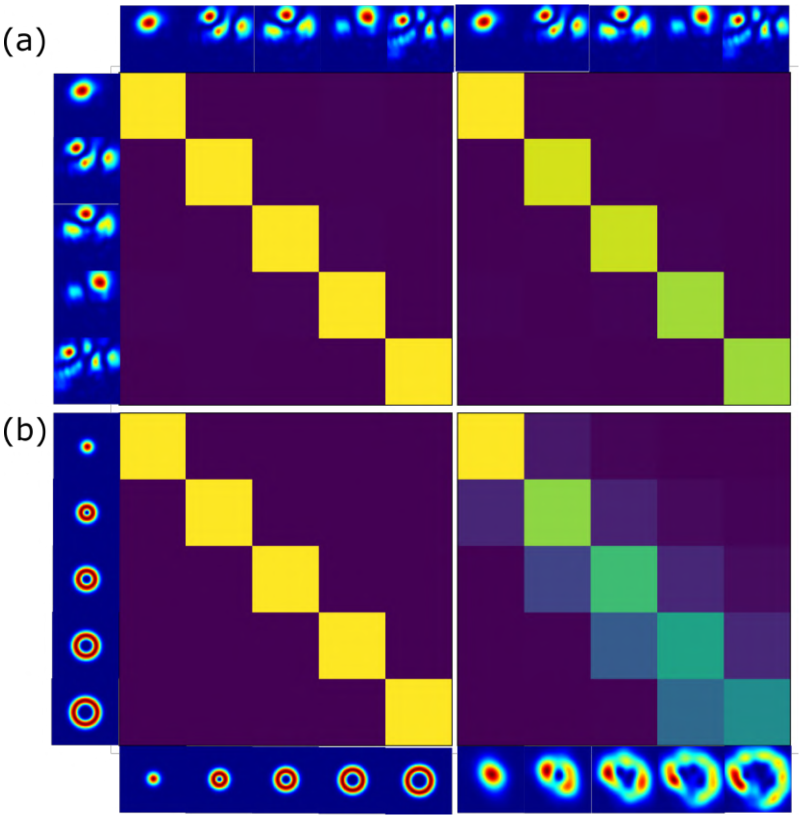

Figure 5.5: (a) and (b) are crosstalk matrices for five modes before (left column) and after (right column) a turbulent channel. (a) corresponds to the eigenmodes of the channel whereas (b) shows the crosstalk for LG beams with $\ell \in [0, 4]$.

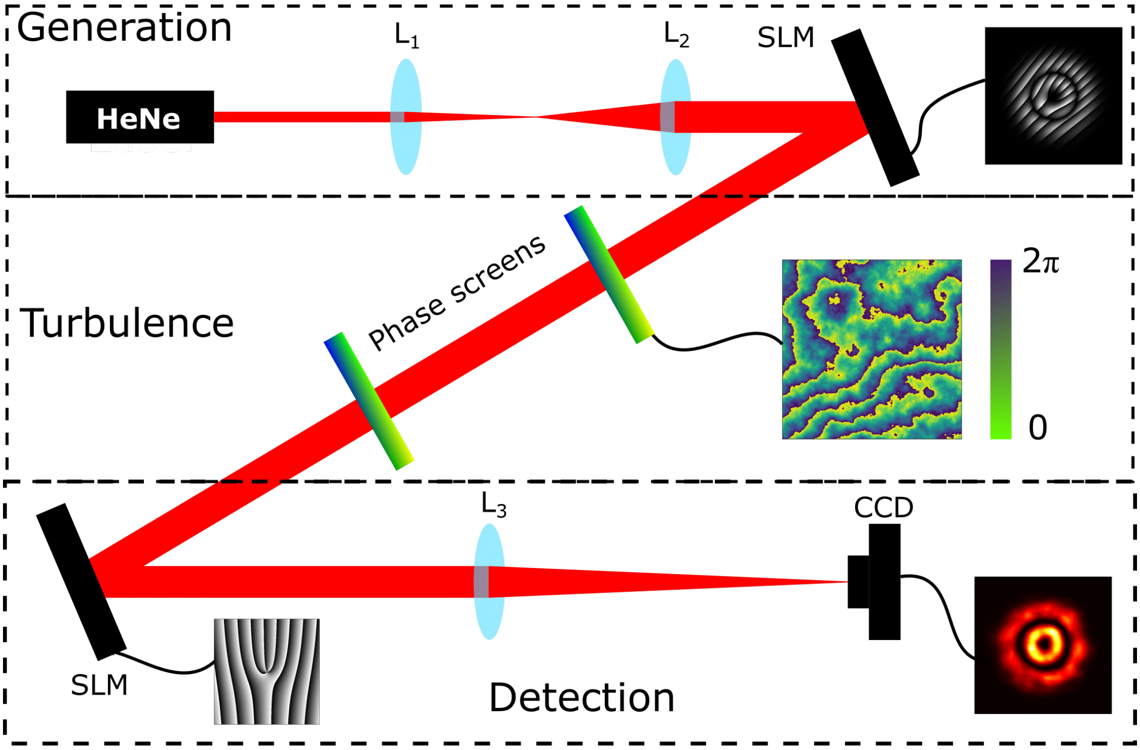

Figure 5.6: A Gaussian beam is expanded and collimated by lenses L_1 and L_2 onto an SLM where it is shaped into a desired field. This field passes through two turbulent phase screens before bouncing off another SLM on which a hologram of a basis state is displayed. The field then passes through lens L_3 so that the intensity of its Fourier transform is captured by a CCD.

10.6 mm with a distance of 100 m between them. This channel was simulated on the setup shown in Fig. 5.6 using the above-mentioned Fresnel scaling procedure. The scaling factors were chosen to be: $\alpha_x = \alpha_{x'} = 0.1$ and $\alpha_z = 0.01$. This corresponded to a total path length of $L' = 2$ m and segment Fried parameter $r_{0,s} = 1.06$ mm.

Using these parameters, a turbulence operator $\mathcal{T}$ was constructed for a unit consisting of a phase screen followed by one metre of propagation. The eigenmodes were found using numerical techniques (in MATLAB). The modes were generated and turbulence was simultaneously introduced on one half of an SLM. After propagating a metre, the beam was incident on the other half of the same SLM on which the same phase screen was displayed. The beam propagated one metre again before its intensity pattern was captured on a CCD. To confirm that the effects of turbulence were indeed significant, LG beams with $p = 0$ and $\ell \in [0, 3]$ were sent through the same channel. The effects of turbulence on the intensity pattern of these modes are displayed in Fig. 5.6(a), and the resilience of the intensity of the eigenmodes is shown in Fig. 5.6(b). In both (a) and (b), the top row illustrates the beam before the channel, and the bottom row shows the same beams after propagating through the channel.

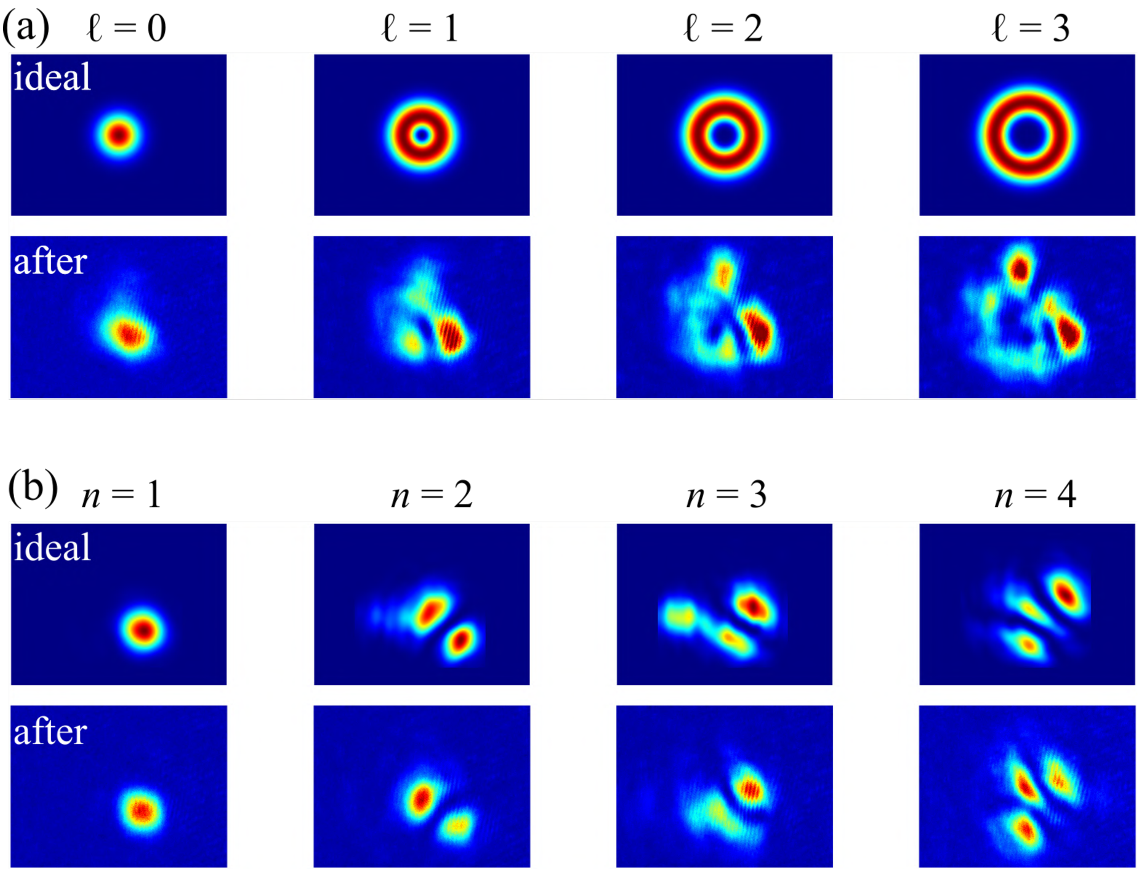

Figure 5.7: (a) LG beams with topological charge $\ell \in [0, 3]$ are highly perturbed by the turbulent channel. This can be seen by comparing the beams before propagating through the channel (top row, labelled 'ideal') to the same beams after propagating through the channel. (b) The eigenmodes are robust through the channel and maintain their intensity patterns. The index n labels the mode order.

5.4 Averaging effects

Solving the eigenvalue problem in Eq. 5.9 must be done for a single instance of Θ, the turbulent phase. For each realisation of turbulence, these modes will remain unchanged. However, different realisations of turbulence will, of course, produce different eigenmodes. These different instances of eigenmodes are not necessarily correlated with each other and averaging over many realisations of turbulence is not trivial.

We explore the effects of averaging over many different sets of eigenmodes where each set corresponds to a different realisation of turbulence. This can be done analytically by examining Eq. 5.1 over many different realisations of turbulence to get the ensemble average equation

$$\langle \mathrm{U}(\mathbf{r}) \rangle = 2k^2 \int \mathrm{d}^3\mathbf{R}' \, \frac{\exp\left(ik\|\mathbf{R}' - \mathbf{R}\|\right)}{4\pi\|\mathbf{R}' - \mathbf{R}\|} \left\langle \delta n(\mathbf{R}')\mathrm{U}(\mathbf{R}') \right\rangle . \tag{5.21}$$

Finding an expression for the term $\langle \delta n(\mathbf{R}')\mathrm{U}(\mathbf{R}) \rangle$ is not trivial. Such an expression does exist but its derivation involves functional derivatives and the Furutsu-

Novikov formula.[69] It is

$$\left\langle \delta n(\mathbf{R}')\mathrm{U}(\mathbf{R}') \right\rangle = \frac{ik}{2} A_n(0) \left\langle \mathrm{U}(\mathbf{R}') \right\rangle , \tag{5.22}$$

where A_n is the two dimensional refractive index correlation function presented in Eq. 3.18. Substituting Eq. 5.22 into Eq. 5.21 gives

$$\left\langle \mathrm{U}(\mathbf{R}) \right\rangle = ik^3 A_n(0) \int \mathrm{d}^3\mathbf{R}' \, \frac{\exp\left(ik\|\mathbf{R}' - \mathbf{R}\|\right)}{4\pi\|\mathbf{R}' - \mathbf{R}\|} \left\langle \mathrm{U}(\mathbf{R}') \right\rangle . \tag{5.23}$$

The are two ways to interpret Eq. 5.23. First, we recognize that Eq. 5.23 is identical to the usual, zero-turbulence Fresnel integral, up to a constant. Therefore, the averaged eigenmodes should be solutions to the free space (zero turbulence) case. Secondly, if we substitute a free space mode in the initial plane ($z = 0$) instead of $\langle \mathrm{U}(\mathbf{r}) \rangle$ as the driving term, we can conclude that there is no average local effect/distortion of turbulence on free space modes.

Substituting a solution U_0 to the vacuum Helmholtz equation as the driving term means that the final, average beam, after experiencing the turbulent channel, is

$$\left\langle \mathrm{U}(\mathbf{R}) \right\rangle = \mathrm{U}_0(\mathbf{R}) \exp\left(-2\pi^2 k^2 z \int_0^\infty \mathrm{d}k \;\, k\Phi(k) \right) . \tag{5.24}$$

The mean effect of turbulence on structured light beams is the acquisition of a global exponential dampening in the beam's amplitude.

We can view turbulence as a tunable perturbation which distorts the vacuum modes into the now-called eigenmodes. To measure this perturbative effect for a given mode order n, the inner product (overlap integral) of the ideal vacuum states and eigenmodes was calculated for strengths in the range $D/r_0 \in [0, 1.5]$. To obtain the average overlap for a given strength and mode number, 60 random phase screens were generated for each strength and the resulting operator was diagonalised. Even though the first six ($n \in [1, 6]$) eigenmodes were found for each operator, Fig. 5.8 shows only four modes. This is because modes corresponding to $n = 2$, 3 can be mapped to superpositions of $LG_{p=0}^{\ell=1}$ and $LG_{p=0}^{\ell=-1}$ beams. However, the orientation of these modes is highly unstable and will change with even the slightest perturbation. One may, mistakenly, calculate a low correlation (overlap), simply because the modes have rotated. Insets in Fig. 5.8 show (from left to right in each row): the vacuum eigenmodes (left), the average field of the vacuum modes after the channel (see Eq. 5.24) and the average field of the eigenmodes. The turbulent insets correspond to $D/r_0 = 1.5$.

Is it evident from the insets in Fig. 5.8 that the average field of the vacuum modes after the channel closely resembles the initial vacuum modes, and presents a numerical confirmation to Eq. 5.24. Fig. 5.8 also shows that eigenmodes with mode orders corresponding to rotationally symmetric vacuum states resemble the unperturbed states more closely than other, less symmetric modes.

In optical communication studies, some set of orthogonal modes form a basis which conveys information across the channel. For a given instance of turbulence, the eigenmodes of that specific realisition will, of course, form a better basis (in terms of mode fidelity), defined as

$$\text{Fidelity} = \text{trace}\{\mathcal{I}\}/N \tag{5.25}$$

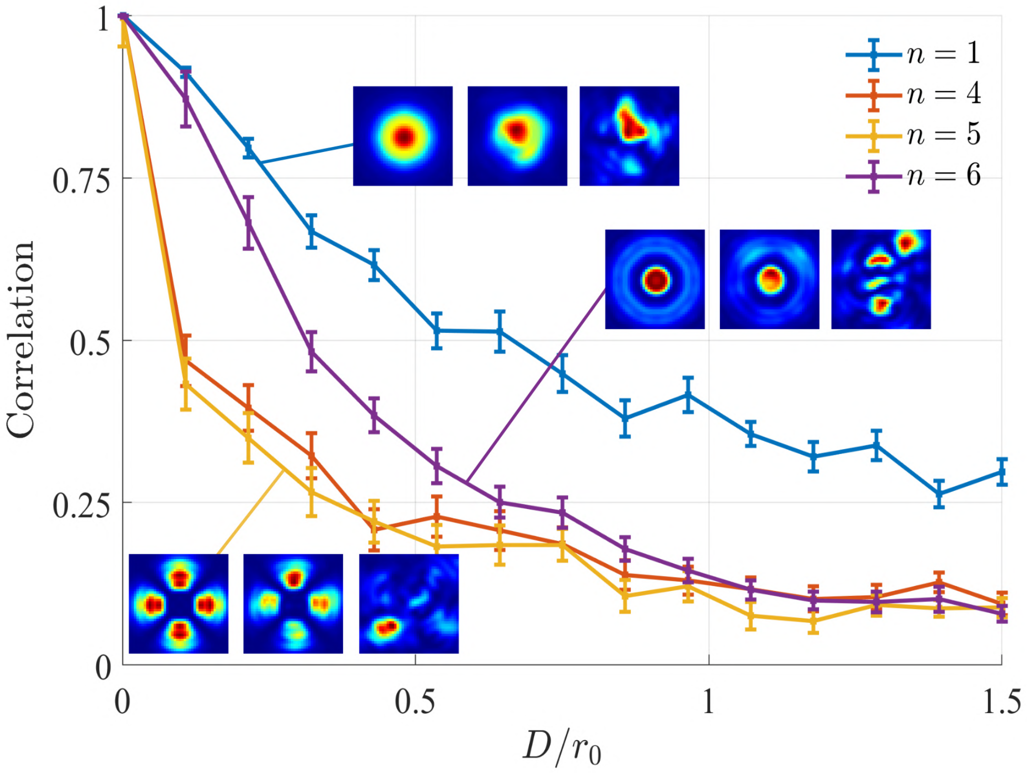

Figure 5.8: The correlation or modal overlap between the vacuum modes and the eigenmodes for a range of turbulence strengths. The first six eigenmodes were obtained for sixty phase screens for each turbulence strength and the modal overlap (inner product) between these eigenmodes and the corresponding (same order) vacuum modes was computed before taking the average. Insets (from left to right) show: the initial vacuum mode; the average vacuum mode after it has been through the turbulent channel; the average eigenmode of order n. Modes with orders 2 and 3 were suppressed since their field patterns are highly sensitive to rotations.

than some set of vacuum modes. N is the number of basis modes and I is their crosstalk matrix. However, one may wonder, how do the eigenmodes of one turbulence instance fair compared to the vacuum modes in a different realisation of turbulence? This question is numerically investigated in Fig. 5.9 by selecting two different sets of eigenmodes at random, alongside the vacuum modes, and observing their fidelity through different turbulent channels. Fig. 5.9(a) shows the intensity patterns of three of the six basis states for each mode set. Set 2 of the turbulent eigenmodes corresponds to a stronger turbulence strength than set 1. In Fig. 5.9(b), we see the expected decay in fidelity for increasing turbulence strength, calculated for 800 iterations per ratio D/r_0. We see that the turbulent eigenmodes are less robust than their vacuum counterparts and one is better off using the usual vacuum states (like LG beams) if one is not going to change the mode set for each instance of turbulence.

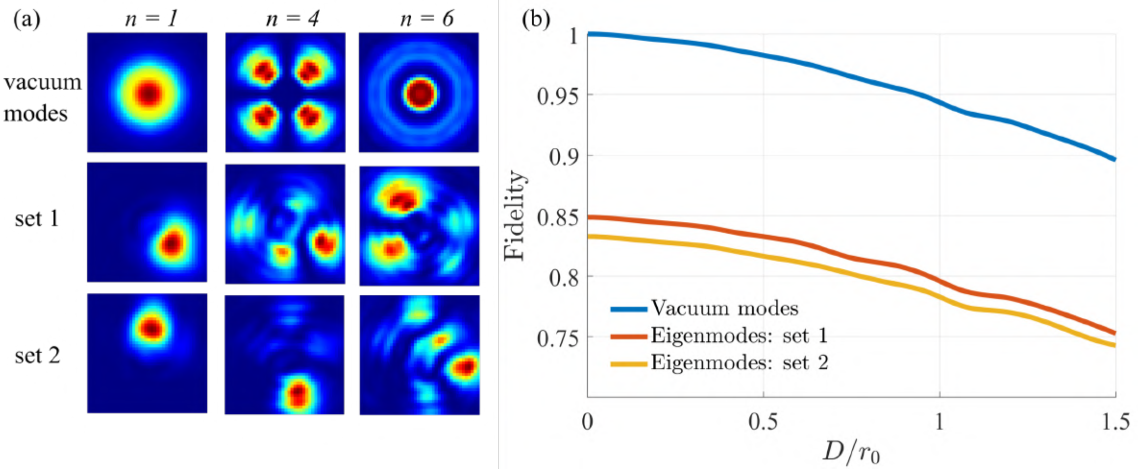

Figure 5.9: The fidelity of three sets of modes is simulated for weak to moderate turbulence, where 800 instances of turbulence were examined for each Fried parameter r_0. The modes were: the 'vacuum' modes found by diagonalising the zero-turbulence propagation operator and two randomly selected sets of eigenmodes for random phase screens. Insets show the intensity patterns of the modes where modes in the same column have the same mode number.

5.5 Discussion and conclusion

We have developed and implemented a procedure for finding modes which are unchanged after propagating through a turbulent channel by discretising the Fresnel integral into an operator which can be represented in a discrete matrix. The eigenmodes are then found using numerical tools, like those found in MATLAB. These modes are eigenmodes in their truest sense i.e. they are fixed under the action of the channel.

Others have recommended using a singular value decomposition procedure to obtain so-called singular modes. These modes have singular values of one, which means that all the light present in the transmitting plane is collected and detected in the detecting plane. Such an approach was used by Miller[98] with a discretised Green's function, similar to the operator we presented in Eq. 5.6. However, this treatment of the subject is very terse and does not easily open the topic up to the reader without some effort.

Others[99] have used the singular value decomposition technique with two different basis sets: the input plane is described by LG modes and the output plane is represented in the pixel basis. Such a treatment allows the description of a larger grid size but does not return eigenmodes: even though these modes have unit singular values and thus preserve the light, their field patterns change between the transmitting and receiving planes.

Pai *et al*. developed 'scattering invariant modes' by studying a layer of zinc oxide nanopowder which was deposited on a glass slide.[100] These modes are solutions to the generalised linear eigenvalue problem $\mathcal{T}\mathrm{E} = \gamma_{\mathrm{air}}\mathcal{T}_{\mathrm{air}}\mathrm{E}$ where $\mathcal{T}$ and $\mathcal{T}_{\mathrm{air}}$ are the scattering and free-space channels, respectively. The scattering invariant modes E are not eigenmodes, however, they simultaneously diagonalise the scattering and vacuum operators, and so these modes appear the same after propagating through the scattering medium or free space. This is a weaker condition since the modes are allowed to evolve over propagation, unlike the modes presented here.

In all of these approaches, eigenmodes are channel specific and this may prove to be impractical in real-time due to the fast changing nature of turbulence. In order to physically implement these modes, it would be necessary to first characterise the turbulent channel and then diagonalise it before it changes.

Even though turbulence played the role of our noisy channel, this method is not restricted to turbulence and can be used on any channel whose properties are known.

Chapter 6

Conclusion

This dissertation examined and characterised the highly topical interaction of structured light fields and atmospheric turbulence using the Kolmogorov model.

Chapter 1 began with a brief overview of structured light and the different beam types used in this dissertation before explaining scalar diffraction theory and the angular spectrum method of propagation. The chapter concluded with the mathematical derivation of the orbital angular momentum carried by structured light fields.

Chapter 2 presented all the experimental techniques which were utilised during the course of this project. The operation of liquid crystal spatial light modulators and digital micromirror devices was explained along with their calibration and set-up procedures. These devices were used to shape light, simulate turbulence and take measurements through the implementation of holograms. The chapter also showed how these holograms are generated for the two devices. We showed how one can perform an inner product (modal overlap) optically in order to obtain a modal decomposition of a desired field, and how to obtain and calculate the required correction factors to ensure that the measured data is correct.

We turned to the theory of atmospheric turbulence in chapter 3 by first discussing its characteristics and statistics. We then showed how turbulence is modelled and how it impacts on optical fields. This led to the thin phase screen approximation and to the different methods used to generate these screens. A full treatment of these generation procedures was presented and the two approaches were compared against each other. The modelling of a thick atmosphere (strong turbulence) was explained via the split-step (many screen) method. Finally, the experimental calibration of these turbulent screens was explained.

Chapter 4 and Chapter 5 introduced novel research. In Chapter 4, we viewed the atmosphere as a store of orbital angular momentum which it can exchange with propagating structured light fields. We showed that the spread in the OAM spectrum of optical fields perturbed by turbulence was symmetric and peaked at the initial topological charge. This model allowed us to decouple the atmosphere from specific beam types and allowed us to reach general conclusions, such as the fact that the behaviour of an OAM-carrying mode is independent of its initial charge. The debate on the lack of robustness of higher order modes was resolved by realising that the size of a mode determines its behaviour in turbulence and not its OAM, all else held equal. This was demonstrated experimentally for both Laguerre-Gaussian and perfect vortex modes. The disagreement over the symmetry and single-peaked nature of a beam's OAM spectrum in the strong regime was resolved by comparing measurements in the OAM and LG bases.

Chapter 5 wrote the turbulent channel as a linear operator and successfully diagonalised it, yielding families of modes which are impervious to the deleterious effects of turbulence. Numerical pitfalls were highlighted and the eigenmodes were experimentally verified in a laboratory setting. It was also theoretically and numerically shown that turbulence has a zero average influence on vacuum modes and that these modes prove to be a better basis for optical communication when many instances of turbulence are considered.

Future work

It was shown in Chapter 4 that turbulence results in a spread in the OAM carried by optical fields, and that this spread is independent of a field's initial topological charge ℓ. This leads us to the following hypothesis: a mode built from the sum of the Φ_ℓ should be more resilient as adjacent modes will scatter into each other equally, preserving the initial power in each mode. Such a basis does exist, and are the so-called angular modes, defined as

$$|\Psi_n(\mathbf{r})\rangle = \frac{1}{\sqrt{d}} \sum_{\ell=-p}^{p} \exp\left(\frac{i2\pi\ell n}{d}\right) |\Phi_\ell(\mathbf{r})\rangle\,, \tag{6.1}$$

where $p = (d-1)/2$, d is the total number of Φ_ℓ and

$$|\Phi_\ell(\mathbf{r})\rangle = \exp(i\ell\phi). \tag{6.2}$$

These modes have intensity profiles that look like angular 'wedges'. Fig. 6.1 shows intensity profiles for angular ((a) – (c)) and OAM ((d) – (f)) modes for $d = 11$. One can see that changing the index n rotates the wedge profile azimuthally.

We can express the transformation from the $\{\Phi_\ell\}$ to the $\{\Psi_n\}$ as a matrix $\mathbf{U}$ with elements

$$U_{jk} = \frac{1}{\sqrt{d}} \exp\left(\frac{i2\pi(j-p-1)(k-p-1)}{d}\right) \tag{6.3}$$

so that

$$|\Psi_n\rangle = \mathbf{U}\,|\Phi_n\rangle = \sum_j U_{jn}\,|\Phi_j\rangle\,. \tag{6.4}$$

Further, we express the turbulent phase (working in the weak scintillation regime) $\exp(i\Theta)$ as a matrix $\mathbf{T}$ with elements $T_{ij} = \langle\Phi_i|\, e^{i\Theta}\,|\Phi_j\rangle$, which operates on the states $\{\Phi_\ell\}$ like

$$\mathbf{T}\,|\Phi_m\rangle = \sum_j T_{jm}\,|\Phi_j\rangle\,. \tag{6.5}$$

These matrix elements are related to the probability $P(\Delta) = P(\ell|m)$ by

$$P(\Delta) = \left\langle |T_{\ell m}|^2 \right\rangle. \tag{6.6}$$

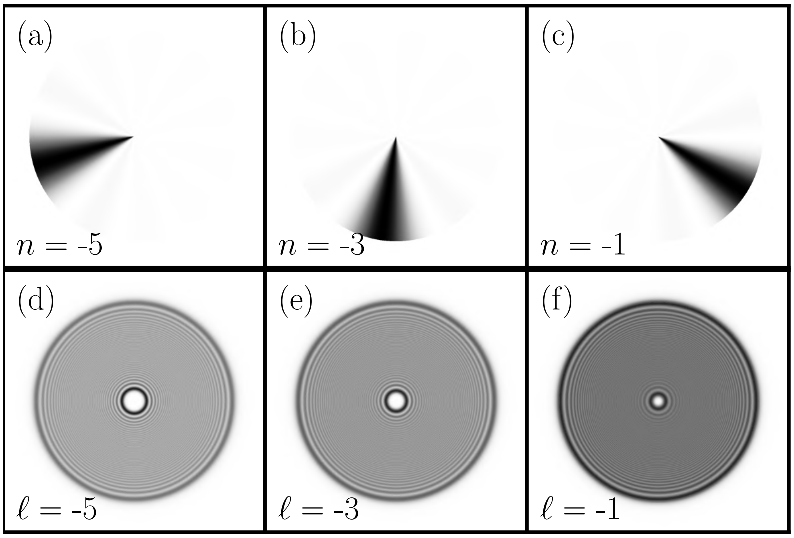

Figure 6.1: (a) – (b) show intensity profiles for angular modes with indices equal to -5, -3 and -1 respectively. (d) – (f) show intensity plots for OAM vortex modes with charges -5, -3 and -1.

Let the scattering amplitude from the state $|\Psi_j\rangle$ to $|\Psi_k\rangle$ be S_{kj}. Using the definition of the angular modes in the OAM basis, we get

$$S_{kj} = \langle \Psi_k | e^{i\Theta} |\Psi_j\rangle = \frac{1}{d}\sum_{\ell}\sum_{\ell'} e^{i2\pi(\ell' j - \ell k)/d} T_{\ell\ell'}, \tag{6.7}$$

which is more easily visualised as a matrix equation:

$$S_{kj} = \frac{1}{d}\begin{pmatrix}1 & \cdots & e^{i2\pi k/d}\end{pmatrix} \mathbf{T} \begin{pmatrix}1 \\ \vdots \\ e^{-i2\pi j/d}\end{pmatrix}. \tag{6.8}$$

Letting the indices k and j range from 0 to $d-1$ gives us the equation

$$\mathbf{S} = \mathbf{U}^{\dagger}\mathbf{T}\mathbf{U}. \tag{6.9}$$

The improved fidelity of these angular modes through turbulence is numerically demonstrated in Fig. 6.2. **T** refers to the turbulence operator in the OAM basis, whereas **S** is the equivalent operator in the transformed, angular basis. Clearly, the angular modes are more resilient. However, we see that the matrix $\mathbf{U}^{\dagger}\mathbf{T}\mathbf{U}$ does not match with the directly measured matrix **S**. This improved resilience is also shown in Fig. 6.3 for two turbulence strengths, $D/r_0 = 1.8$ and $D/r_0 = 4.0$. Future work will attempt to obtain experimental results, confirming the improved robustness of angular modes through turbulence and explain the discrepancy between the nearly-diagonal matrix **S** and its calculated counterpart $\mathbf{U}^{\dagger}\mathbf{T}\mathbf{U}$. Further, future work will focus on understanding the source of these modes' resilience and investigating whether other mode families exist which are equally robust.

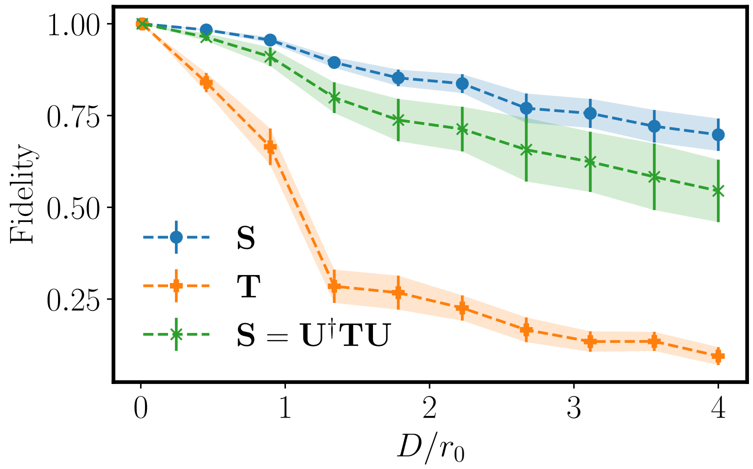

Figure 6.2: Fidelity of modes after propagating through increasing turbulence strengths in the weak scintillation regime. The fidelity is the average value of the diagonal elements of the crosstalk matrix.

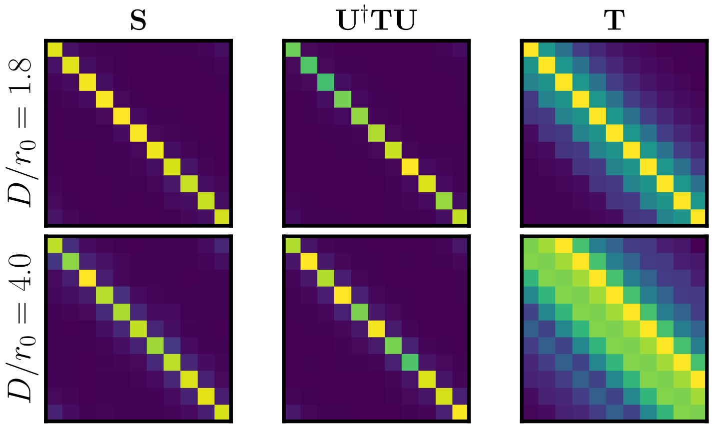

Figure 6.3: Crosstalk matrices for angular ($\mathbf{S}$) and OAM ($\mathbf{T}$) modes through moderate and strong turbulence in the weak scintillation regime. The matrix $\mathbf{U}^\dagger\mathbf{T}\mathbf{U}$ is the calculated angular mode crosstalk matrix which is the quantum Fourier transform of $\mathbf{T}$.

Appendix A

A.1 Statistical preliminaries

Let $x(t)$ be a real, random, stationary variable which depends on t. "Stationary" means that only differences between t values are significant, but not absolute values. The correlation function R_x is defined as

$$R_x(t_1, t_2) = \langle x(t_1)x(t_2) \rangle = R_x(\tau), \quad \tau = t_2 - t_1. \tag{A.1}$$

Let the mean value of x be $m = \langle x(t) \rangle$. Then, the covariance function B_x is defined as

$$\begin{aligned} B_x(\tau) = B_x(t_1, t_2) &= \langle [x(t_1) - m][x(t_2) - m] \rangle \\ &= \langle x(t_1)x(t_2) \rangle - m^2 = R_x(\tau) - m^2 \end{aligned} \tag{A.2}$$

since x is stationary. We use B_x to define the structure function $\mathcal{D}_x$ as

$$\mathcal{D}_x(\tau) = \left\langle |x(t_1) - x(t_2)|^2 \right\rangle = 2\left(B_x(0) - B_x(\tau)\right). \tag{A.3}$$

The power spectral density $\Phi_x(\omega)$ is calculated from B_x as the Fourier transform

$$\begin{aligned} \Phi_x(\omega) &= \int \mathrm{d}t\ B_x(t) \exp\left(-i2\pi t\omega\right) \\ &= \int \mathrm{d}t\ B_x(t) \cos\left(2\pi t\omega\right), \end{aligned} \tag{A.4}$$

if we require both B and Φ to be real. The structure function can be obtained from inversely transforming the power spectral density by

$$\mathcal{D}_x(\tau) = 2 \int \mathrm{d}\omega\ \Phi(\omega)\left(1 - \cos(2\pi t\omega)\right), \tag{A.5}$$

using Eq. A.3. These definitions are then easily generalised to three spatial dimensions i.e. $t \mapsto \mathbf{r} = (x, y, z)$. The spatial analogue of "stationary" random variables are statistically homogeneous and isotropic random fields. "Statistically homogeneous" means that only the difference between points in the random field is significant, whereas "isotropic" means that we only need to look at the magnitude of the vector difference between two points as the direction does not matter.

A.2 Phase structure function

Consider a one dimensional structure function $\mathcal{D}(x)$ and power spectral density $\mathcal{P}(\nu)$ which are related according to

$$\mathcal{D}(x) = 2 \int\limits_{-\infty}^{\infty} \mathrm{d}\nu \;\; \mathcal{P}(\nu)\,(1 - \cos(x\nu))\,. \tag{A.6}$$

We must remove term of $1 \times \mathcal{P}(\nu)$ in the integrand. This is achieved by differentiating with respect to x so that

$$\frac{\mathrm{d}}{\mathrm{d}x}\mathcal{D}(x) = -2 \int\limits_{-\infty}^{\infty} \mathrm{d}\nu \;\; \nu\mathcal{P}(\nu)\sin(x\nu). \tag{A.7}$$

For a real valued (random) process the structure function is even[69] (see Eq. A.6). We can use the the Fourier sine transformations[101]

$$\begin{aligned} F(\nu) &= \int\limits_{0}^{\infty} \mathrm{d}x \;\; \sin(x\nu) f(x) \\ f(x) &= \frac{1}{2\pi}\int\limits_{0}^{\infty} \mathrm{d}\nu \;\; \sin(x\nu) F(\nu), \end{aligned} \tag{A.8}$$

to write

$$\mathcal{P}(\nu) = \frac{1}{8\pi\nu}\int\limits_{0}^{\infty} \mathrm{d}x \;\; \sin(x\nu)\frac{\mathrm{d}}{\mathrm{d}x}\mathcal{D}(x). \tag{A.9}$$

Now, consider the three dimensional case described by a power spectral density function $\Phi(\mathbf{k})$. Again, the field is assumed to be statistically homogeneous and isotropic. The power spectral density is again the transform of the covariance $B(R)$

$$\Phi(k) = \frac{1}{(2\pi)^3}\int \mathrm{d}^3\mathbf{R} \;\; B(R)\exp(-i\mathbf{k}\cdot\mathbf{R}), \tag{A.10}$$

and the covariance is the inverse transform of Φ

$$B(R) = \int \mathrm{d}^3\mathbf{k} \;\; \Phi(k)\exp\left(i\mathbf{k}\cdot\mathbf{R}\right). \tag{A.11}$$

We can partially solve Eq. A.11 by aligning the coordinate systems such that $\mathbf{k}\cdot\mathbf{R} = kR\cos(\vartheta)$ and solving the resulting angular integral

$$\int\limits_{0}^{\pi} \mathrm{d}\vartheta \int\limits_{0}^{2\pi} \mathrm{d}\varphi \;\; \sin\vartheta\exp\left(ikR\cos\vartheta\right) = 4\pi\frac{\sin\left(kR\right)}{kR}. \tag{A.12}$$

This means that Eq. A.11 reduces to the radial integral

$$B(R) = \frac{4\pi}{R}\int\limits_{0}^{\infty} \mathrm{d}k \;\; k\Phi(k)\sin(kR), \tag{A.13}$$

and that the structure function is given by

$$\mathcal{D}(R) = 8\pi \int_0^\infty \mathrm{d}k\ k^2\Phi(k)\left(1 - \frac{\sin(kR)}{kR}\right). \tag{A.14}$$

Integrating Eq. A.6 by parts, while assuming that the power spectral density goes to zero at infinity, yields an expression comparable to Eq. A.14:

$$\begin{aligned}\mathcal{D}(x) &= 4\left[\mathcal{P}(\nu)\left(\nu - \frac{\sin(x\nu)}{x}\right)\right]_0^\infty - 4\int_0^\infty \mathrm{d}\nu\ \left(\nu - \frac{\sin(x\nu)}{x}\right)\frac{\mathrm{d}}{\mathrm{d}\nu}\mathcal{P} \\ &= -4\int_0^\infty \mathrm{d}\nu\ \nu^2\left(1 - \frac{\sin(x\nu)}{\nu x}\right)\frac{1}{\nu}\frac{\mathrm{d}}{\mathrm{d}\nu}\mathcal{P},\end{aligned} \tag{A.15}$$

where we changed the integration bounds in Eq. A.6 to zero and ∞ and compensated with a factor of 2. Equating the two expressions (Eq. A.14 and Eq. A.15) for the structure functions gives us the relation

$$\Phi(k) = -\frac{1}{2\pi k}\frac{\mathrm{d}}{\mathrm{d}k}\mathcal{P}(k). \tag{A.16}$$

Consider a structure function $\mathcal{D}(x) = Cx^p$. The one dimensional power spectral density is

$$\mathcal{P}(\nu) = \frac{1}{8\pi\nu}\int_0^\infty \mathrm{d}x\ \sin(x\nu)\frac{\mathrm{d}}{\mathrm{d}x}\mathcal{D}(x) = C\left[\frac{\Gamma(p+1)}{2\pi}\sin\left(\frac{\pi p}{2}\right)\right]\nu^{-p-1}, \tag{A.17}$$

and the three dimensional power spectral density $\Phi(k)$ is given by

$$\Phi(k) = \frac{1}{2\pi k}C\left[\frac{\Gamma(p+1)}{2\pi}\sin\left(\frac{\pi p}{2}\right)\right](p+1)\,k^{-p-2} \tag{A.18}$$

$$= C\left[\frac{\Gamma(p+2)}{4\pi^2}\sin\left(\frac{\pi p}{2}\right)\right]k^{-p-3}. \tag{A.19}$$

For Kolmogorov theory, $C = C_n^2$ and $p = 2/3$ and so

$$\Phi(k) = 0.033C_n^2k^{-11/3}. \tag{A.20}$$

A.3 Field OAM statistics

This section presents the theory from Ref.[55,56] which derives an expression for the probability of measuring $\ell\hbar$ of OAM in an optical vortex beam $\exp(im\phi)$ initially carrying $m\hbar$ of OAM per photon. This analysis treats turbulence as a phase only effect.

Consider an initial beam of the form $\mathrm{V}_i = \mathcal{A}\exp(im\phi)$ defined over a radius R. After propagating through weak turbulence, the field will have picked up a phase Θ so that the final field is $\mathrm{V}_f = \mathcal{A}\exp(im\phi)\exp(i\Theta)$. We perform the following two expansions in the OAM basis:

$$\exp(i\Theta(\mathbf{r})) = \sum_n g_n(r)\exp(in\phi), \tag{A.21}$$

where

$$g_n(r) = \frac{1}{2\pi}\int_0^{2\pi} \mathrm{d}\phi \; \exp(i\Theta - in\phi), \tag{A.22}$$

and

$$\mathrm{V}_f(\mathbf{r}) = \sum_\ell c_\ell(r)\exp(i\ell\phi), \tag{A.23}$$

where

$$c_\ell(r) = \frac{1}{2\pi}\int_0^{2\pi} \mathrm{d}\phi \; \mathrm{V}_f(r)\exp(-i\ell\phi) = \frac{\mathcal{A}}{2\pi}\int_0^{2\pi} \mathrm{d}\phi \; \exp(i\Theta)\exp(-i(\ell-m)\phi). \tag{A.24}$$

Substituting Eq. A.21 into Eq. A.24 and evaluating the integral gives

$$c_\ell(r) = \mathcal{A}g_{\ell-m}(r) \implies |c_\ell|^2 = |\mathcal{A}|^2|g_{\ell-m}|^2, \tag{A.25}$$

where we have suppressed the explicit spatial dependence. Eq. A.25 shows that the power remaining in the original mode with topological charge $\ell = m$ is proportional to the zeroth order expansion coefficient of the phase, $|g_0|^2$. To derive an expression for the average probability of measuring $\ell\hbar$ in the final field we begin by finding an average form of $|c_\ell|^2$. This is achieved using Eq. A.22 and Eq. A.25 which leaves the double integral over two angular coordinates

$$\left\langle |c_\ell(r)|^2 \right\rangle = \left|\frac{\mathcal{A}}{2\pi}\right|^2 \int \mathrm{d}\phi \int \mathrm{d}\phi' \; \left\langle \exp\left(i\left[\Theta(\mathbf{r}') - \Theta(\mathbf{r})\right]\right)\right\rangle \exp\left(i\Delta(\phi'-\phi)\right), \tag{A.26}$$

where $\Delta \equiv \ell - m$ is the difference between the final and inital topological charges. The fact that the phase is statistically homogeneous and isotropic means we only have to look at the relative difference between ϕ' and ϕ and can set ϕ or ϕ' to zero to convert the exponential containing the turbulent phase into

$$\left\langle \exp\left(i\left[\Theta(\mathbf{r}') - \Theta(\mathbf{r})\right]\right)\right\rangle = \exp\left[-\frac{1}{2}\mathcal{D}_\Theta\left(2r\left|\sin\left(\frac{\phi}{2}\right)\right|\right)\right], \tag{A.27}$$

where $\mathcal{D}_\Theta(\cdot)$ is the structure function of the turbulent phase and we used the result $\langle\exp(ix)\rangle = \exp\left(-\left\langle |x|^2\right\rangle/2\right)$ for a Gaussian random variable x. Inserting Eq. A.27 back in to Eq. A.26 with the explicit form of the structure function, integrating over the radial coordinate and dividing by the total power[54] of the initial field gives an expression for the average probability of measuring $\ell\hbar$ of OAM in the final field

$$P(\ell) = \frac{1}{\pi}\int_0^1 \mathrm{d}\rho \int_0^{2\pi} \cos(\Delta\phi)\exp\left(-\frac{1}{2}\mathcal{D}_\Theta\left(2\rho\sin\left(\frac{\phi}{2}\right)\right)\right). \tag{A.28}$$

Bibliography

[1] D. J. Richardson, “Filling the light pipe,” *Science*, vol. 30, pp. 327–328, 2010.

[2] D. J. Richardson, J. M. Fini, and L. E. Nelson, “Space-division multiplexing in optical fibres,” *Nat. Photonics*, vol. 7, no. 5, pp. 354–362, 2013.

[3] S. Berdagué and P. Facq, “Mode division multiplexing in optical fibers,” *Appl. Opt.*, vol. 21, no. 11, pp. 1950–1955, 1982.

[4] A. Trichili, K.-H. Park, M. Zghal, B. S. Ooi, and M.-S. Alouini, “Communicating using spatial mode multiplexing: Potentials, challenges, and perspectives,” *IEEE Commun. Surv. Tutor.*, vol. 21, no. 4, pp. 3175–3203, 2019.

[5] A. Forbes, M. de Oliveira, and M. R. Dennis, “Structured light,” *Nat. Photonics*, vol. 15, no. 4, pp. 253–262, 2021.

[6] L. Allen, M. W. Beijersbergen, R. Spreeuw, and J. Woerdman, “Orbital angular momentum of light and the transformation of laguerre-gaussian laser modes,” *Phys. Rev. A*, vol. 45, no. 11, p. 8185, 1992.

[7] M. J. Padgett, “Orbital angular momentum 25 years on,” *Opt. Express*, vol. 25, no. 10, pp. 11265–11274, 2017.

[8] Y. Shen, X. Wang, Z. Xie, C. Min, X. Fu, Q. Liu, M. Gong, and X. Yuan, “Optical vortices 30 years on: Oam manipulation from topological charge to multiple singularities,” *Light Sci. Appl.*, vol. 8, no. 1, pp. 1–29, 2019.

[9] A. Trichili, C. Rosales-Guzmán, A. Dudley, B. Ndagano, A. Ben Salem, M. Zghal, and A. Forbes, “Optical communication beyond orbital angular momentum,” *Sci. Rep.*, vol. 6, no. 1, p. 27674, 2016.

[10] N. Zhao, X. Li, G. Li, and J. M. Kahn, “Capacity limits of spatially multiplexed free-space communication,” *Nat. Photonics*, vol. 9, no. 12, p. 822, 2015.

[11] Y. Zhou, M. Mirhosseini, S. Oliver, J. Zhao, S. M. H. Rafsanjani, M. P. Lavery, A. E. Willner, and R. W. Boyd, “Using all transverse degrees of freedom in quantum communications based on a generic mode sorter,” *Opt. Express*, vol. 27, no. 7, pp. 10383–10394, 2019.

[12] N. Mphuthi, R. Botha, and A. Forbes, “Are bessel beams resilient to aberrations and turbulence?,” *JOSA A*, vol. 35, no. 6, pp. 1021–1027, 2018.

[13] N. Mphuthi, L. Gailele, I. Litvin, A. Dudley, R. Botha, and A. Forbes, "Free-space optical communication link with shape-invariant orbital angular momentum bessel beams," *Appl. Opt.*, vol. 58, no. 16, pp. 4258–4264, 2019.

[14] I. P. Lukin, "Mean intensity of vortex bessel beams propagating in turbulent atmosphere," *Appl. Opt.*, vol. 53, no. 15, pp. 3287–3293, 2014.

[15] C. Bao-Suan and P. Ji-Xiong, "Propagation of gauss–bessel beams in turbulent atmosphere," *Chinese Phys. B*, vol. 18, no. 3, p. 1033, 2009.

[16] K. Zhu, G. Zhou, X. Li, X. Zheng, and H. Tang, "Propagation of bessel-gaussian beams with optical vortices in turbulent atmosphere," *Opt. Express*, vol. 16, no. 26, pp. 21315–21320, 2008.

[17] W. Nelson, J. Palastro, C. Davis, and P. Sprangle, "Propagation of bessel and airy beams through atmospheric turbulence," *JOSA A*, vol. 31, no. 3, pp. 603–609, 2014.

[18] N. Ahmed, Z. Zhao, L. Li, H. Huang, M. P. Lavery, P. Liao, Y. Yan, Z. Wang, G. Xie, Y. Ren, *et al.*, "Mode-division-multiplexing of multiple bessel-gaussian beams carrying orbital-angular-momentum for obstruction-tolerant free-space optical and millimetre-wave communication links," *Sci. Rep.*, vol. 6, p. 22082, 2016.

[19] M. Cheng, L. Guo, J. Li, and Y. Zhang, "Channel capacity of the oam-based free-space optical communication links with bessel–gauss beams in turbulent ocean," *IEEE Photonics J.*, vol. 8, no. 1, pp. 1–11, 2016.

[20] T. Doster and A. T. Watnik, "Laguerre–gauss and bessel–gauss beams propagation through turbulence: analysis of channel efficiency," *Appl. Opt.*, vol. 55, no. 36, pp. 10239–10246, 2016.

[21] R. J. Watkins, K. Dai, G. White, W. Li, J. K. Miller, K. S. Morgan, and E. G. Johnson, "Experimental probing of turbulence using a continuous spectrum of asymmetric oam beams," *Opt. Express*, vol. 28, no. 2, pp. 924–935, 2020.

[22] M. A. Cox, L. Maqondo, R. Kara, G. Milione, L. Cheng, and A. Forbes, "The Resilience of Hermite- and Laguerre-Gaussian Modes in Turbulence," *J. Light. Technol.*, vol. 37, no. 16, pp. 3911–3917, 2019.

[23] B. Ndagano, N. Mphuthi, G. Milione, and A. Forbes, "Comparing mode-crosstalk and mode-dependent loss of laterally displaced orbital angular momentum and Hermite–Gaussian modes for free-space optical communication," *Opt. Lett.*, vol. 42, no. 20, p. 4175, 2017.

[24] S. Restuccia, D. Giovannini, G. Gibson, and M. Padgett, "Comparing the information capacity of Laguerre–Gaussian and Hermite–Gaussian modal sets in a finite-aperture system," *Opt. Express*, vol. 24, no. 24, p. 27127, 2016.

[25] B. Ndagano, I. Nape, M. A. Cox, C. Rosales-Guzman, and A. Forbes, "Creation and detection of vector vortex modes for classical and quantum communication," *J. Light. Technol.*, vol. 36, pp. 292–301, 2017.

[26] A. Sit, F. Bouchard, R. Fickler, J. Gagnon-Bischoff, H. Larocque, K. Heshami, D. Elser, C. Peuntinger, K. Günthner, B. Heim, C. Marquardt, G. Leuchs, R. W. Boyd, and E. Karimi, "High-dimensional intracity quantum cryptography with structured photons," *Optica*, vol. 4, no. 9, p. 1006, 2017.

[27] Z. Zhu, M. Janasik, A. Fyffe, D. Hay, Y. Zhou, B. Kantor, T. Winder, R. W. Boyd, G. Leuchs, and Z. Shi, "Compensation-free high-capacity free-space optical communication using turbulence-resilient vector beams," *arXiv preprint arXiv:1910.05406*, 2019.

[28] M. A. Cox, C. Rosales-Guzmán, M. P. J. Lavery, D. J. Versfeld, and A. Forbes, "On the resilience of scalar and vector vortex modes in turbulence," *Opt. Express*, vol. 24, pp. 18105–18113, 2016.

[29] A. Willner, H. Huang, Y. Yan, Y. Ren, N. Ahmed, G. Xie, C. Bao, L. Li, Y. Cao, Z. Zhao, *et al.*, "Optical communications using orbital angular momentum beams," *Adv. Opt. Photonics*, vol. 7, no. 1, pp. 66–106, 2015.

[30] J. Wang, J.-Y. Yang, I. M. Fazal, N. Ahmed, Y. Yan, H. Huang, Y. Ren, Y. Yue, S. Dolinar, M. Tur, and A. E. Willner, "Terabit free-space data transmission employing orbital angular momentum multiplexing," *Nat. Photonics*, vol. 6, no. 7, pp. 488–496, 2012.

[31] A. Trichili, M. A. Cox, B. S. Ooi, and M.-S. Alouini, "Roadmap to free space optics," *JOSA B*, vol. 37, no. 11, pp. A184–A201, 2020.

[32] M. P. Lavery, C. Peuntinger, K. Günthner, P. Banzer, D. Elser, R. W. Boyd, M. J. Padgett, C. Marquardt, and G. Leuchs, "Free-space propagation of high-dimensional structured optical fields in an urban environment," *Sci. Adv.*, vol. 3, no. 10, p. e1700552, 2017.

[33] X. Gu, L. Chen, and M. Krenn, "Phenomenology of complex structured light in turbulent air," *ArXiv*, p. 1906.03581v1, 2019.

[34] M. A. Cox, N. Mphuthi, I. Nape, N. Mashaba, L. Cheng, and A. Forbes, "Structured light in turbulence," *IEEE J. Sel. Top. Quantum Electron*, vol. 27, no. 2, pp. 1–21, 2020.

[35] C. Paterson, "Atmospheric turbulence and orbital angular momentum of single photons for optical communication," *Phys. Rev. Let.*, vol. 94, no. 15, p. 153901, 2005.

[36] B. Ndagano, B. Perez-Garcia, F. S. Roux, M. McLaren, C. Rosales-Guzman, Y. Zhang, O. Mouane, R. I. Hernandez-Aranda, T. Konrad, and A. Forbes, "Characterizing quantum channels with non-separable states of classical light," *Nat. Phys.*, vol. 13, no. 4, pp. 397–402, 2017.

[37] Y. Zhang, S. Prabhakar, F. S. Roux, A. Forbes, T. Konrad, *et al.*, "Experimentally observed decay of high-dimensional entanglement through turbulence," *Phys. Rev. A*, vol. 94, no. 3, p. 032310, 2016.

[38] T. Brünner and F. S. Roux, "Robust entangled qutrit states in atmospheric turbulence," *New J. Phys.*, vol. 15, p. 063005, 2013.

[39] A. H. Ibrahim, F. S. Roux, M. McLaren, T. Konrad, and A. Forbes, "Orbital-angular-momentum entanglement in turbulence," *Phys. Rev. A*, vol. 88, no. 1, p. 12312, 2013.

[40] D. Bachmann, V. N. Shatokhin, and A. Buchleitner, "Universal entanglement decay of photonic orbital angular momentum qubit states in atmospheric turbulence: an analytical treatment," *J. Phys. A*, vol. 52, no. 40, p. 405303, 2019.

[41] A. K. Jha, G. A. Tyler, and R. W. Boyd, "Effects of atmospheric turbulence on the entanglement of spatial two-qubit states," *Phys. Rev. A*, vol. 81, p. 053832, 2010.

[42] N. D. Leonhard, V. N. Shatokhin, and A. Buchleitner, "Universal entanglement decay of photonic-orbital-angular-momentum qubit states in atmospheric turbulence," *Phys. Rev. A*, vol. 91, no. 1, p. 12345, 2015.

[43] J. A. Anguita, M. A. Neifeld, and B. V. Vasic, "Turbulence-induced channel crosstalk in an orbital angular momentum-multiplexed free-space optical link," *Appl. Opt.*, vol. 47, no. 13, p. 2414, 2008.

[44] J. A. Anguita, M. A. Neifeld, and B. V. Vasic, "Modeling channel interference in an orbital angular momentum-multiplexed laser link," p. 74640U, SPIE, 2009.

[45] Z. Qu and I. B. Djordjevic, "500 Gb/s free-space optical transmission over strong atmospheric turbulence channels," *Opt. Lett.*, vol. 41, no. 14, p. 3285, 2016.

[46] G. Milione, M. P. J. Lavery, H. Huang, Y. Ren, G. Xie, T. A. Nguyen, E. Karimi, L. Marrucci, D. A. Nolan, R. R. Alfano, and A. E. Willner, "Gbit/s mode division multiplexing over free space using vector modes and a q-plate mode (de)multiplexer," *Opt. Lett.*, vol. 40, no. 9, pp. 1980–1983, 2015.

[47] S. Li, S. Chen, C. Gao, and A. E. Willner, "Atmospheric turbulence compensation in orbital angular momentum communications: Advances and perspectives," *Opt. Commun.*, vol. 408, pp. 68–81, 2018.

[48] L. Li, H. Song, R. Zhang, Z. Zhao, C. Liu, K. Pang, H. Song, J. Du, A. N. Willner, A. Almaiman, B. Lynn, R. Bock, M. Tur, and A. E. Willner, "Demonstration of Both Mode and Space Diversity in a 100-Gbit/s QPSK Free-Space Optical Link to Increase System Tolerance to Turbulence," in *Optical Fiber Communication Conference (OFC) 2019*, (Washington, D.C.), p. W4A.5, OSA, 2019.

[49] Z. Li, J. Su, and X. Zhao, "Atmospheric turbulence compensation with sensorless ao in oam-fso combining the deep learning-based demodulator," *Opt. Commun.*, vol. 460, p. 125111, 2020.

[50] G. Gbur and R. K. Tyson, "Vortex beam propagation through atmospheric turbulence and topological charge conservation," *J. Opt. Soc. Am. A*, vol. 25, pp. 225–230, 2008.

[51] M. Krenn, R. Fickler, M. Fink, J. Handsteiner, M. Malik, T. Scheidl, R. Ursin, and A. Zeilinger, "Communication with spatially modulated light through turbulent air across vienna," *New J. Phys.*, vol. 16, no. 11, p. 113028, 2014.

[52] M. Krenn, J. Handsteiner, M. Fink, R. Fickler, R. Ursin, M. Malik, and A. Zeilinger, "Twisted light transmission over 143 km," *Proc. Natl. Acad. Sci. U.S.A.*, vol. 113, no. 48, pp. 13648–13653, 2016.

[53] F. Steinlechner, S. Ecker, M. Fink, B. Liu, J. Bavaresco, M. Huber, T. Scheidl, and R. Ursin, "Distribution of high-dimensional entanglement via an intra-city free-space link," *Nat. Commun.*, vol. 8, no. 1, pp. 1–7, 2017.

[54] G. A. Tyler and R. W. Boyd, "Influence of atmospheric turbulence on the propagation of quantum states of light carrying orbital angular momentum," *Opt. Lett.*, vol. 34, no. 2, pp. 142–144, 2009.

[55] B. Rodenburg, M. P. Lavery, M. Malik, M. N. O'Sullivan, M. Mirhosseini, D. J. Robertson, M. Padgett, and R. W. Boyd, "Influence of atmospheric turbulence on states of light carrying orbital angular momentum," *Opt. Lett.*, vol. 37, no. 17, pp. 3735–3737, 2012.

[56] M. Malik, M. O'Sullivan, B. Rodenburg, M. Mirhosseini, J. Leach, M. P. Lavery, M. J. Padgett, and R. W. Boyd, "Influence of atmospheric turbulence on optical communications using orbital angular momentum for encoding," *Opt. Express*, vol. 20, no. 12, pp. 13195–13200, 2012.

[57] C. Gopaul and R. Andrews, "The effect of atmospheric turbulence on entangled orbital angular momentum states," *New J. Phys.*, vol. 9, no. 4, p. 94, 2007.

[58] C. Chen, H. Yang, S. Tong, and Y. Lou, "Changes in orbital-angular-momentum modes of a propagated vortex gaussian beam through weak-to-strong atmospheric turbulence," *Opt. Express*, vol. 24, no. 7, pp. 6959–6975, 2016.

[59] L. Zhang, F. Shen, B. Lan, and A. Tang, "Mode-dependent crosstalk and detection probability of orbital angular momentum of optical vortex beam through atmospheric turbulence," *J. Opt.*, vol. 22, no. 7, p. 075607, 2020.

[60] I. Nape, K. Singh, A. Klug, W. Buono, C. Rosales-Guzmán, S. Franke-Arnold, A. Dudley, and A. Forbes, "Revealing the invariance of vectorial structured light in perturbing media," *arXiv preprint arXiv:2108.13890*, 2021.

[61] B. Ndagano, N. Mphuthi, G. Milione, and A. Forbes, "Comparing mode-crosstalk and mode-dependent loss of laterally displaced orbital angular momentum and hermite–gaussian modes for free-space optical communication," *Opt. Lett.*, vol. 42, no. 20, pp. 4175–4178, 2017.

[62] M. A. Cox, L. Cheng, C. Rosales-Guzmán, and A. Forbes, "Modal diversity for robust free-space optical communications," *Phys. Rev. Appl.*, vol. 10, no. 2, p. 024020, 2018.

[63] S. O. Arik and J. M. Kahn, "Diversity-multiplexing tradeoff in mode-division multiplexing," *Opt. Lett.*, vol. 39, no. 11, pp. 3258–3261, 2014.

[64] R. K. Tyson, "Bit-error rate for free-space adaptive optics laser communications," *JOSA A*, vol. 19, no. 4, pp. 753–758, 2002.

[65] S. Zhao, J. Leach, L. Gong, J. Ding, and B. Zheng, "Aberration corrections for free-space optical communications in atmosphere turbulence using orbital angular momentum states," *Opt. Express*, vol. 20, no. 1, pp. 452–461, 2012.

[66] Y. Ren, G. Xie, H. Huang, N. Ahmed, Y. Yan, L. Li, C. Bao, M. P. Lavery, M. Tur, M. A. Neifeld, *et al.*, "Adaptive-optics-based simultaneous pre-and post-turbulence compensation of multiple orbital-angular-momentum beams in a bidirectional free-space optical link," *Optica*, vol. 1, no. 6, pp. 376–382, 2014.

[67] M. Li, Y. Li, and J. Han, "Gerchberg–saxton algorithm based phase correction in optical wireless communication," *Phys. Commun.*, vol. 25, pp. 323–327, 2017.

[68] J. Liu, P. Wang, X. Zhang, Y. He, X. Zhou, H. Ye, Y. Li, S. Xu, S. Chen, and D. Fan, "Deep learning based atmospheric turbulence compensation for orbital angular momentum beam distortion and communication," *Opt. Express*, vol. 27, no. 12, pp. 16671–16688, 2019.

[69] L. C. Andrews, "Laser beam propagation through random media," in *SPIE-International Society for Optical Engineering*, 2005.

[70] A. Forbes, *Laser beam propagation: generation and propagation of customized light*. CRC Press, 2014.

[71] J. Pinnell, V. Rodríguez-Fajardo, and A. Forbes, "How perfect are perfect vortex beams?," *Opt. Lett.*, vol. 44, no. 22, pp. 5614–5617, 2019.

[72] C. Rosales-Guzmán and A. Forbes, *How to shape light with spatial light modulators*. SPIE Press, 2017.

[73] J. W. Goodman, *Introduction to Fourier Optics*. McGraw-Hill, 1988.

[74] R. A. Beth, "Mechanical detection and measurement of the angular momentum of light," *Phys. Rev.*, vol. 50, no. 2, p. 115, 1936.

[75] V. Arrizón, U. Ruiz, R. Carrada, and L. A. González, "Pixelated phase computer holograms for the accurate encoding of scalar complex fields," *JOSA A*, vol. 24, no. 11, pp. 3500–3507, 2007.

[76] G. N. Watson, *A treatise on the theory of Bessel functions*. Cambridge University Press, 1995.

[77] S. Scholes, R. Kara, J. Pinnell, V. Rodríguez-Fajardo, and A. Forbes, "Structured light with digital micromirror devices: a guide to best practice," *Opt. Eng.*, vol. 59, no. 4, p. 041202, 2019.

[78] M. Mirhosseini, O. S. Magana-Loaiza, C. Chen, B. Rodenburg, M. Malik, and R. W. Boyd, "Rapid generation of light beams carrying orbital angular momentum," *Opt. Express*, vol. 21, no. 25, pp. 30196–30203, 2013.

[79] W.-H. Lee, "Binary computer-generated holograms," *Appl. Opt.*, vol. 18, no. 21, pp. 3661–3669, 1979.

[80] J. Pinnell, I. Nape, B. Sephton, M. A. Cox, V. Rodríguez-Fajardo, and A. Forbes, "Modal analysis of structured light with spatial light modulators: a practical tutorial," *JOSA A*, vol. 37, no. 11, pp. C146–C160, 2020.

[81] A. N. Kolmogorov, "The local structure of turbulence in incompressible viscous fluid for very large reynolds numbers," *Cr Acad. Sci. URSS*, vol. 30, pp. 301–305, 1941.

[82] A. Oboukhov, "Structure of the temperature field in turbulent flows," *Isv. Geogr. Geophys. Ser.*, vol. 13, pp. 58–69, 1949.

[83] S. Corrsin, "On the spectrum of isotropic temperature fluctuations in an isotropic turbulence," *J. Appl. Phys.*, vol. 22, no. 4, pp. 469–473, 1951.

[84] V. I. Tatarskii, "The effects of the turbulent atmosphere on wave propagation," *Jerusalem: Israel Program for Scientific Translations, 1971*, 1971.

[85] D. L. Fried, "Optical resolution through a randomly inhomogeneous medium for very long and very short exposures," *JOSA*, vol. 56, no. 10, pp. 1372–1379, 1966.

[86] R. J. Noll, "Zernike polynomials and atmospheric turbulence," *JOSA*, vol. 66, no. 3, pp. 207–211, 1976.

[87] N. Roddier, "Atmospheric wavefront simulation using zernike polynomials," *Opt. Eng.*, vol. 29, pp. 1174–1180, 1990.

[88] J. D. Schmidt, "Numerical simulation of optical wave propagation: With examples in matlab," SPIE, 2010.

[89] J. W. Cooley and J. W. Tukey, "An algorithm for the machine calculation of complex fourier series," *Math. Comput.*, vol. 19, no. 90, pp. 297–301, 1965.

[90] C. Rader and N. Brenner, "A new principle for fast fourier transformation," *IEEE Trans. Signal Process.*, vol. 24, no. 3, pp. 264–266, 1976.

[91] R. Lane, A. Glindemann, and J. Dainty, "Simulation of a kolmogorov phase screen," *Waves in random media*, vol. 2, pp. 209–224, 1992.

[92] P. H. Hu, J. Stone, and T. Stanley, "Application of zernike polynomials to atmospheric propagation problems," *J. Opt. Soc. Am. A*, vol. 6, pp. 1595–1608, 1989.

[93] L. Burger, I. A. Litvin, and A. Forbes, "Simulating atmospheric turbulence using a phase-only spatial light modulator," *S. Afr. J. Sci.*, vol. 104, no. 3-4, pp. 129–134, 2008.

[94] G. Sorelli, N. Leonhard, V. N. Shatokhin, C. Reinlein, and A. Buchleitner, "Entanglement protection of high-dimensional states by adaptive optics," *New J. Phys.*, vol. 21, no. 2, p. 023003, 2019.

[95] R. Antonia, H. Shafi, and Y. Zhu, "A note on the vorticity spectrum," *Phys. Fluids*, vol. 8, no. 8, pp. 2196–2202, 1996.

[96] M. Kiya and H. Ishii, "Vortex interaction and kolmogorov spectrum," *Fluid Dyn. Res.*, vol. 8, no. 1-4, p. 73, 1991.

[97] "Simulating thick atmospheric turbulence in the lab with application to orbital angular momentum communication," *New J. Phys.*, vol. 16, no. 3, p. 033020, 2014.

[98] D. A. Miller, "Better choices than optical angular momentum multiplexing for communications," *Proc. Natl. Acad. Sci. U.S.A.*, vol. 114, no. 46, pp. E9755–E9756, 2017.

[99] V. Shatokhin, D. Bachmann, G. Sorelli, N. Treps, and A. Buchleitner, "Spatial eigenmodes of light in atmospheric turbulence," in *Environmental Effects on Light Propagation and Adaptive Systems III*, vol. 11532, p. 115320G, SPIE, 2020.

[100] P. Pai, J. Bosch, M. Kühmayer, S. Rotter, and A. P. Mosk, "Scattering invariant modes of light in complex media," *Nat. Photonics*, vol. 15, no. 6, pp. 431–434, 2021.

[101] G. Sorelli, *Quantum state transfer in diffractive and refractive media*. PhD thesis, Universität Freiburg, 2019.